6-12-2014

Doped-Tin Oxide Aerogels in Dye-Sensitized Solar Cells

Juan Pablo Correa Baena
jpcorreabaena@gmail.com

Doped-Tin Oxide Aerogels in Dye-Sensitized Solar Cells

Juan Pablo Correa Baena, PhD

University of Connecticut, 2014

Aerogels are attractive structures due to their high surface area, high porosity and particle interconnectivity, which are desirable properties for many device applications. They can be made by a facile sol-gel synthesis from low-cost metal salts to produce monolithic gels. These are dried supercritically to avoid the collapse of the structure that occurs with surface tension at the liquid-gas interface. SnO_2 is a n-type, wide bandgap semiconductor. Doped SnO_2 materials can exhibit transparency throughout the visible range of the solar spectrum and low electrical resistivity. They are commonly used as transparent conducting electrodes (TCEs) for a wide array of applications including solar cell fabrication. Here, doped-SnO_2 aerogels are synthesized as bulk and thin film monoliths, the latter serving as porous electron collectors in dye-sensitized solar cells (DSCs). This thesis is an in-depth study of the effects of dopants, namely fluorine and antimony, in the properties of SnO_2 aerogels. First, the use of fluorine and antimony is investigated to understand the effect of these dopants on the physical and optoelectronic properties of the SnO_2 materials. Doped aerogels are then used as thin films and coated with conformal layers of TiO_2 to fabricate DSCs. Solar cell characterization, including performance analysis and electron kinetics in the device, is conducted to understand the advantages of this system compared to the traditional TiO_2 DSCs.

Doped-Tin Oxide Aerogels in Dye-Sensitized Solar Cells

Juan Pablo Correa Baena

B.S., University of Connecticut, **[2008]**

M.S., University of Connecticut, **[2011]**

A Dissertation

Submitted in Partial Fulfillment of the

Requirements for the Degree of Doctor of Philosophy

at the

University of Connecticut

[2014]

APPROVAL PAGE

Doctor of Philosophy Dissertation

Doped-Tin Oxide Aerogels in Dye-Sensitized Solar Cells

Presented by

Juan Pablo Correa Baena, B.S., M.S.

Major Advisor

Dr. Alexander G. Agrios

Associate Advisor

Dr. Ali Gokirmak

Associate Advisor

Dr. Steven L. Suib

Associate Advisor

Dr. Timothy Vadas

Associate Advisor

Dr. Brian Willis

University of Connecticut

[2014]

Acknowledgements

It has been a long journey. I still remember that day when I decided I would move to the great US of A, that place where, as we were told, people fulfilled their goals, succeeded to reach climax and lived happily ever after. Of course, I was 17 and naïve and full of energy and expectation and did not realize the other reality. This was, that I would have to fight harder than the average to achieve what I wanted simply because of my foreignness to the language and to the system. On the other hand, I have been pleasantly surprised to see how this country has mechanisms in place that allow people like me to fulfill their goals.

This of course would not have been possible without the support of a network of people who betted everything and gave everything to help me succeed. I am absolutely convinced that an individual is a compilation of the absorbed surroundings; we are sponges that take in what we need in order to arrive where we want. This is a human condition that has marked my 11 years in this country and that has shaped who I am. My family, my friends and my girlfriend are equality guilty of this fantastic trip through the depths of the mind, which I have explored meticulously in the loneliness of our lab and the furor of exciting conferences. It is because of their support that I am here and I thank them deeply.

As 5-year-old, my grandfather, an engineer by birth, taught me about chemistry and electronics. We built an electric motor with bootleg magnets and copper wire from a local hardware store. We built simple circuits with resistors, transistors and switches. And all the while he inspired me to think critically about the natural phenomena that surround us. It was my mother and aunts and uncles who taught me to work hard and to never be disappointed by negative outcomes related to work, a critical trait in doing finicky research. My cousins, as if they were my brothers, were always an inspiration, pushing each other to get where we wanted. A very important part of my life has been shaped by my amazing girlfriend, who was concurrently doing her MD at

Yale. A combination of brain and rhythms, she has been my true inspiration to live a life of happiness, to enjoy travelling while helping me to be a better scientist. We have travelled more than 15 countries together, backpacking the dirt roads of the Philippines, climbing a mountain in the Himalayas in India or the Andes in South America.

Another well-deserved acknowledgement to Aida Ghiaei and the program she runs; the National Science Foundation's GK-12 program. Without this amazing support and experience (and Aida's motherly protection), I would not have been able to do and learn as much as I did. Working with high school students was pivotal in giving perspective to the research I do and to see the world outside of the lab. Thanks to my advisor Dr. Alexander G. Agrios for all the patience he has (a lot !) and for introducing me to the wonderful world of photovoltaics. Together we learned many things, such as how to make aerogels (neither of us had a clue on how to make these materials at the beginning), about characterization of materials and many more. Alex allowed me to get lost and find myself and get lost again (he gave me a lot of freedom in the project) in the research and I think that was extremely important to become independent and critical. I developed my own ideas and then discussed them with him. I am very grateful for that.

I dedicate this thesis to my mother; strong woman she is. She taught me to be an incessant worker without limiting the mind to challenges of the workplace. She also came through a renaissance of her own where she reinvented herself after years of struggle; set a goal in her mind and I can proudly say that she is still fulfilling those dreams. That is inspirational and it is what has made me fight everyday to make aerogels even if they did not want to cooperate.

"Los seres humanos no nacen para siempre el día en que sus madres los alumbran, sino que la vida los obliga a parirse a sí mismos una y otra vez."

Gabriel Garcia Marquez

El Coronel no Tiene Quien le Escriba

TABLE OF CONTENTS

1 Introduction

Most of the effort in this thesis has been devoted to the preparation of transparent conducting oxide (TCO) aerogel thin films as conducting scaffold used in dye sensitized solar cells (DSC). These structures can find use in many other fields where porosity, transparency in the visible range of the solar spectrum, and conductivity are key. In this work a facile synthetic route to cast the conducting aerogels on glass has been developed. First, a brief introduction to the motivation to research solar cells will be presented alongside some of the general trends in the field. Figure 1.1 summarizes the scope of this thesis including the four main chapters. A thorough background will be discussed where aerogels, TCOs and DSCs will be the main topic (Chapter 2). The effects of fluorine in tin dioxide (SnO_2) aerogel shrinkage will be evaluated in chapter 3, a crucial step towards achieving crack-free monolithic aerogel thin films. Characterization of SnO_2 aerogels doped with varying amounts of antimony (Sib) will be presented in chapter 4. Chapter 5 will explore the incorporation of Sb-doped SnO_2 (ATO) as thin film aerogels in DSC and the performance of the devices.

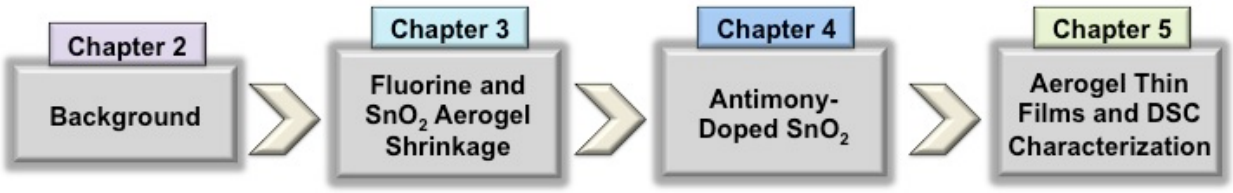

Figure 1.1. Schematic summarizing the focus of this thesis.

1.1 Solar Energy

The sun is largest star in our solar system and is responsible for providing energy that supports life on our planet. Its importance has been recognized for millennia and it has been worshiped by a myriad of cultures. This is not surprising since its effects directly impact crop yields which

are dependent on photosynthesis and the major climatic phenomena on the surface of the earth.[1]

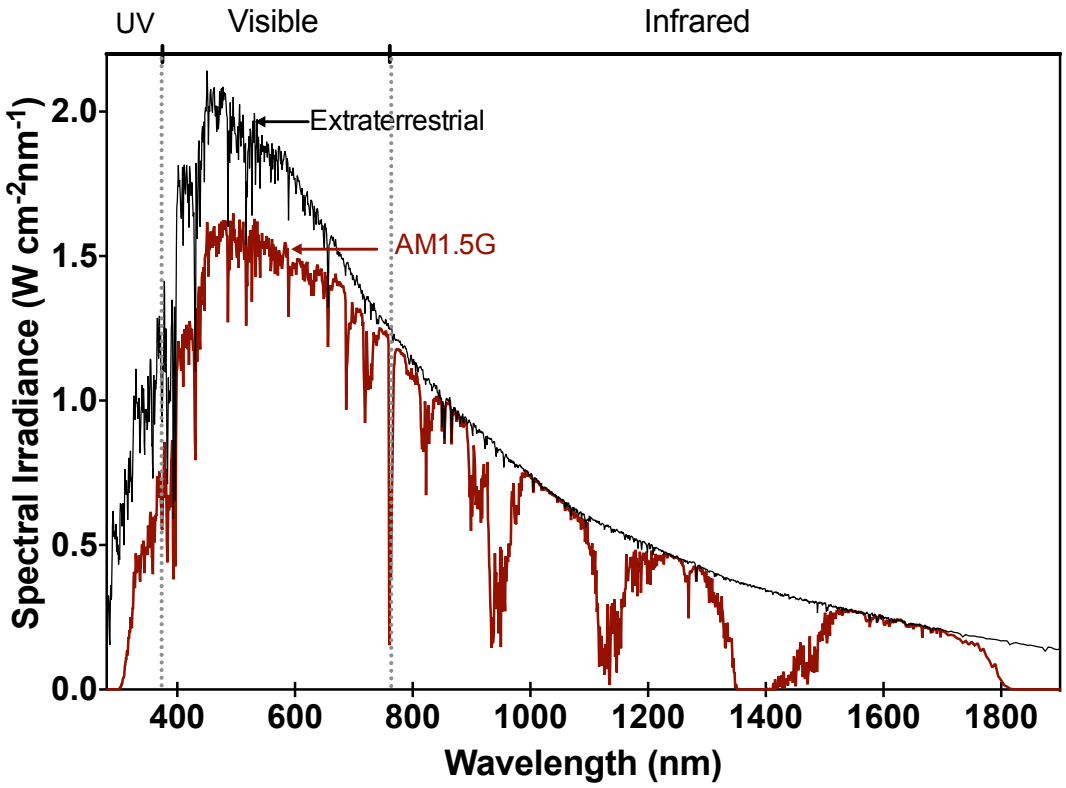

Figure 1.2. Solar irradiation spectrum outside the earth's atmosphere (black) and at AM1.5 (red).[2]

Solar irradiation is composed of light that exhibits wave-like properties which can be described by its wavelength and frequency. Light can also be characterized as photons with energy that can be quantified by the expression

$$E = h \cdot v = h \cdot \frac{c}{\lambda} \qquad (2.1)$$

where *h* is Planck's constant, *v* is the frequency, c is the speed of light and λ is the wavelength. Since both *h* and c are constants, the energy of photons varies with its wavelength and it is therefore a vital variable for materials development in harvesting light from the sun. Outside the

earth's atmosphere (extraterrestrial in Figure 1.2) the power density of light is estimated to be 1353 W m^{-2}. Atmospheric absorption and light scattering reduce this number to 1000 W m^{-2} at sea level measured at an angle θ of 48˚ (otherwise known as air mass, AM1.5) between the light irradiation and the zenith (Figure 1.2). AM1.5 is a commonly used standard for testing and characterization of solar cell devices. The air mass numbers can also be explained in terms of the solar spectrum, where higher AM is more red-shifted, whereas lower is more blue-shifted.

1.2 Photovoltaic Devices

Increased evidence of global warming, which is blamed for the deicing of Arctic and Antarctic poles, and the imminence of hydrocarbon fuel depletion, have raised public demand for renewable sources of energy. As a result, governments and private corporations have increased investment in solar and wind generation methods.[3] Solar cells are a promising source of clean and renewable energy and great efforts are being made to improve the efficiency and durability and decrease the cost of the cells. In particular, photovoltaic (PV) cells are devices that produce direct current electrical power when illuminated by photons. The PV effect was first discovered by Edmond Becquerel in 1839, in France, paving the way to today's research on solar cells.[4] In the 1954, researchers at Bell Labs in the USA discovered that pn junctions produced a current when exposed to light. This was the beginning of photovoltaic device research, which reached 6% efficiency for silicon within a year.[5] Shortly after, gallium arsenide and cadmium selenide solar cells with efficiencies around 6% were reported. Si devices have been used in a wide range of applications and are the major player in the PV market. They have also been the major player as commercially available solar panels for solar farms and household use.

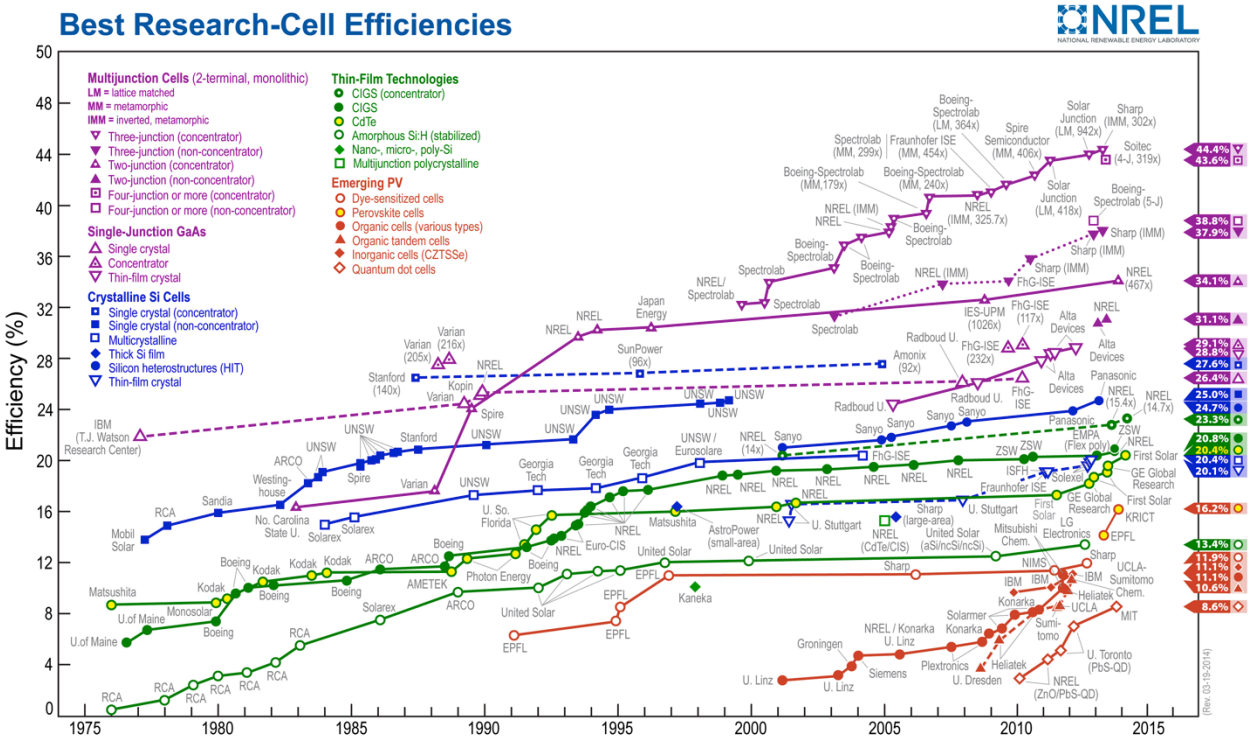

Figure 1.3. Summary of efficiencies of certified best performance research PV devices by year and solar cell type. (Taken from the National Renewable Energy Laboratory website)

There are several types of solar cells that can be classified in three main groups or generations.[6] The first generation PV devices are based on high purity Si and GaAs, among others. Although silicon is widely available and inexpensive, processing it to form defect-free crystals is very energy intensive and therefore costly. The second-generation solar cells include thin films of amorphous Si, CdTe, CuInGaSe, and dye-sensitized solar cells (DSC). Both first and second-generation PV devices are currently commercially available and widely used. The third generation includes solar cells that exceed 30% efficiency by using multiple layers of semiconductor to absorb different ranges of the solar spectrum. Solar cells can also be categorized into multijunction, single-junction GaAs, Si, thin films and emerging PV, as shown in the chart developed by the National Renewable Research Laboratory (Figure 1.3). In this chart the best certified laboratory PV devices are presented on a yearly basis. Multi-junction cells

under concentrated sunlight exhibit the highest efficiencies ever recorded. Crystalline Si and thin film devices show great performance. The emerging PV technologies are much more recent and show efficiencies up to 16.2% with perovskite cells, a system developed alongside DSCs.

2 Background

2.1 Dye-sensitized solar cells

Pioneered by Michael Grätzel in the early 90s the DSC has become one of the most promising technologies to harvest energy from the sun.[7] The solar cell has a photoanode, a cathode, and an electrolyte (Figure 2.1). The photoanode is typically made of titanium dioxide (TiO_2) nanoparticles sintered on a transparent conductive oxide (TCO) glass. A film of such particles is submerged in a bath of dye molecules, which attach to the surface of the TiO_2 (sensitization) and are responsible for absorbing light. This layer is about 10 μm-thick composed of a network of nanoparticles in the range of 20-30 nm in diameter. The porosity is about 60% in the mesopore range to allow the electrolyte to diffuse through without major resistance. Ruthenium bipyridyl complexes have commonly been used as sensitizers achieving efficiencies above 11%[8] and more recently porphyrin-sensitized DSCs obtained efficiencies above 12%.[9] The sensitizers absorb sunlight, exciting an electron that is subsequently injected into the conduction band of the semiconductor. Electrons then diffuse through this layer of nanoparticles, hopping from particle to particle until reaching the TCO glass. The hole transport material (HTM), typically a redox couple comprised of iodide triiodide (I^-/I_3^-), shuttles electrons from the platinized counter electrode to reduce the oxidized sensitizer, thus completing the electron cycle.

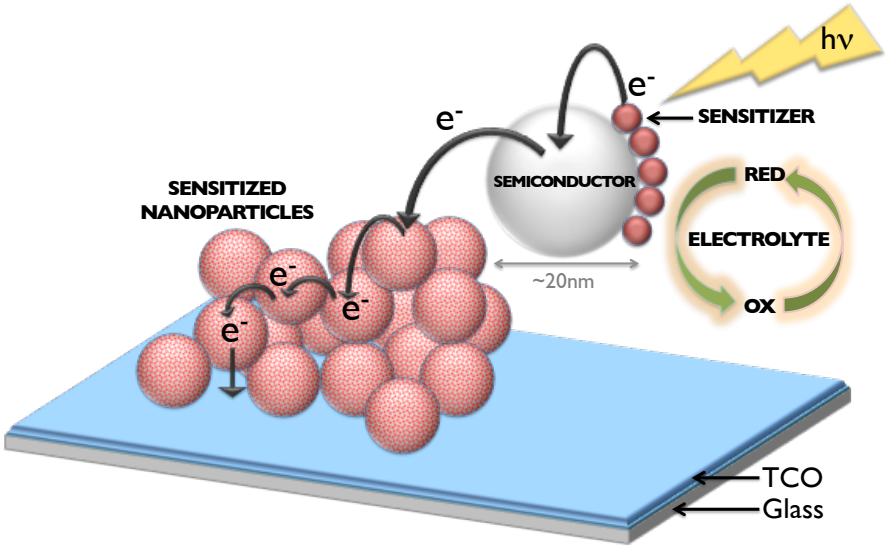

Figure 2.1. Schematic of the components of the DSC with electron pathways.

2.1.1 Key Processes in the DSC

There are six key processes important for understanding the mechanisms of electron transfer through the DSC. These are solar excitation of the dye, electron injection from the dye to the semiconductor, the back transfer of electrons from the TiO_2 to the dye, the regeneration of the dye by the electrolyte (iodide), the electron transport through the semiconductor nanoparticles and the recombination process (back transfer of electrons) from the TiO_2 nanoparticle to the triiodide. These reactions are as follows;[10] the dye absorbs a photon of a certain energy and becomes excited

$$D + h\nu \rightarrow D^* \qquad (2.2)$$

The photoexcited dye injects an electron to the conduction band of the TiO_2, which in turn oxidizes the dye

$$D^* \rightarrow D^+ + e^-_{TiO2} \qquad (2.3)$$

Electrons can recombine with the oxidized dye

$$D^+ + e^-_{TiO2} \rightarrow D \quad (2.4)$$

Alternatively the dye can be reduced by iodide,

$$2D^+ + 3I^- \rightarrow D + I_3^- \quad (2.5)$$

Lastly, electrons can recombine with triiodide

$$I_3^- + 2e^-_{TiO2} \rightarrow 3\ I^- \quad (2.6)$$

This last process will be discussed in detail in the rest of this chapter and is an important part in Chapter 5.

2.1.2 Electron Kinetic Processes

Figure 2.2 shows the energy diagram of a DSC with the electron transfer processes in each component of the device. The black arrows show the forward electron transfers, which is started by the excitation of electrons in the highest unoccupied molecular orbital (HOMO) of the sensitizer. The injection of these electrons from the lowest unoccupied molecular orbital (LUMO) into the conduction band of the semiconductor induces the energetic increase of the Fermi level from E_F to ${}_nE_F$ (Figure 2.2). The voltage of the solar cell is then determined as the difference between the latter (otherwise known as the quasi-Fermi energy) and the potential of the electrolyte. Electrons are cycled by an external circuit and are returned to the cell via the platinized TCO glass to reduce the electrolyte. Recombination processes are shown as red arrows (Figure 2.2), where electrons can be lost by back reaction within the dye by decay and from the semiconductor to the HOMO of the dye or the electrolyte (equations 2.6).

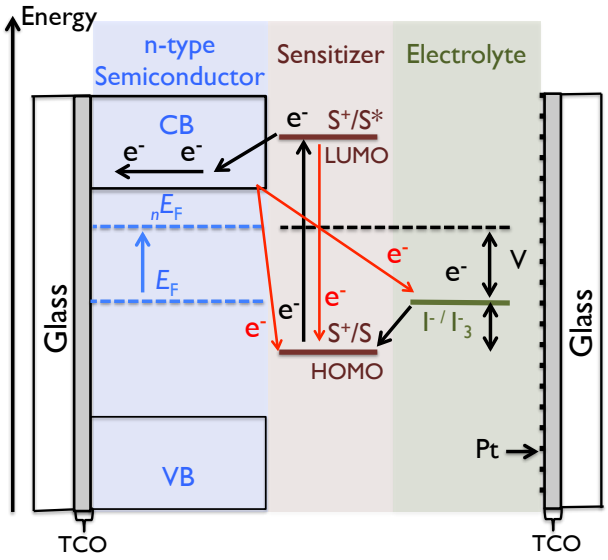

Figure 2.2. Schematic of the electron transfer processes in a typical DSC.

With the exception of this report,[11] it is widely understood that the electron injection from the LUMO of a ruthenium complex dye to the semiconductor is faster than its decay,[12,13] making this process negligible. The recombination processes from the semiconductor to the electrolyte are much more detrimental to the device performance. This is because of the similar rates between electron transport through the semiconductor array and those of recombination. In short, the electrons in the conduction band compete to either diffuse through the film and out to the TCO glass, which is described by the diffusion coefficient, D, or recombine with the oxidized dye and electrolyte, or electron lifetime, τ_e. It is well known that TiO_2 exhibits a slow electron transport rate due to its inherently low conductivity. A summary of these electron kinetic processes is presented in Figure 2.3,[14] where the black and red arrows represent the transport and recombination rates, respectively. These two components determine what is referred to as the diffusion length of the device, which measures how far electrons can go in a semiconductor film before recombination of such electrons occurs,

$$L_n = \sqrt{D \cdot \tau_e} \qquad (2.7)$$

where in order to achieve maximal collection of electrons, this expression must be larger than the thickness of the film in the device.

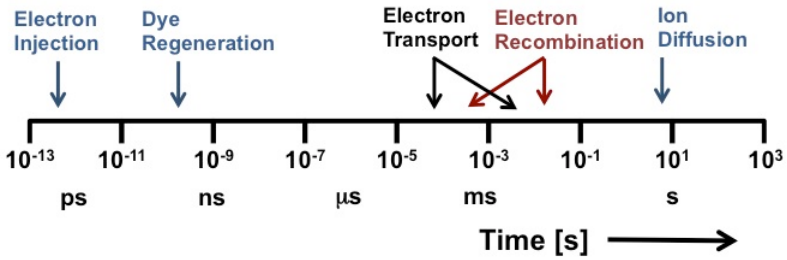

Figure 2.3. Summary of the kinetics in the DSC.[14]

2.1.3 Alternative Hole Transporting Materials

Ever since the O'Reagan and Grätzel findings were published in 1991, I^-/I_3^- has been used as a standard electrolyte. This redox couple has been intensely studied and had until very recently the highest performance compared to most other electrolytes due to its good solubility, chemical stability and relatively low recombination reaction from TiO_2. However, the I^-/I_3^- redox couple has many disadvantages, including a large overpotential (difference between redox potential and the HOMO of the sensitizer in Figure 2.2), which limits the voltage of the cell.[15] I^-/I_3^- electrolytes are also corrosive and therefore detrimental for long-term device durability.

Researchers have been looking for alternative redox couples to achieve greater efficiencies. Over the past few years, alternative liquid and solid state HTM have been explored with great success, which has made them potential replacements for the ubiquitous I^-/I_3^-. One issue still remains which is the faster electron recombination of these materials when compared to I^-/I_3^-, which has yielded solar cell efficiencies below 0.4%.[16,17] This was changed by Daeneke and coworkers who used ferrocene/ferrocenium (Fc/Fc^+)-based DSC and demonstrated much improved performance with a bulky metal-free dye.[18] Thanks to the modified HOMO/LUMO of the dye, the single electron redox reaction (lower overpotential) and lower recombination rate,

the device achieved a remarkable 7.5%. Similarly, Yella and coworkers achieved an unrivaled efficiency of 12.3% using a cobalt redox couple. Using a bulky porphyrin dye, which retards electron recombination, they were able to absorb photons across the visible spectrum obtaining great currents and voltages. Several important studies have been published on the use of cobalt complexes as redox couples.[19-23] Solid state DSCs have become a major player in the field ever since Bach and coworkers studied the feasibility of the organic compound 2,2',7,7'-Tetrakis[N,N-di(4-methoxyphenyl)amino]-9,9'-spirobifluorene (Spiro-OMeTAD) as the HTM.[24] Highly efficient DSCs have been prepared with this material in the past few year,[25] but the challenge still remain on the efficient percolation of the molecule through thick films of semiconductor nanoparticulate films.[26] Similar to iron and cobalt-based electrolytes, this organic HTM shows higher recombination rates than traditional I^-/I_3^- electrolyte DSCs.[27] This material has been used in perovskite-based solar cells achieving efficiencies above 15%.[28-30]

2.2 Transparent Conducting Oxides

2.2.1 Doping Mechanisms

Transparent conducting oxides (TCO) are materials that transmit light in the visible spectrum while conducting electrical current.[31,32] This phenomenon was first discovered when, a over a century ago, researchers spray deposited cadmium metal, which did not oxidize properly at this high temperature, thus producing a transparent highly conductive material.[33] Whereas some metals are the most conductive materials known, they are not transparent in the visible range of the solar spectrum, making TCO materials ideal for optoelectronic device applications, such as flat panel displays. Produced as compact films, these materials can exhibit very low resistivities in the order of 10^{-3}-10^{-5} Ω cm and transmission in the visible range above 80%. Different TCO materials can transmit light at different wavelengths and their optoelectronic characteristics can change with doping, for instance for SnO_2-based materials the change in sheet resistance from 100 to 5 Ω/sq can translate to a big loss in the transmission in the infrared part of the

electromagnetic spectrum as seen in Figure 2.4.[34] The sample at 5 Ω/sq therefore may be useless for application where the transparency is needed at a wavelength of 1500 nm. This type of TCO is ideal for applications in DSCs because these devices use dyes that are active mostly in the visible range of the spectrum. Therefore, guaranteeing transparency in this range allows for minimized absorption of the material that will conduct electrons in the device.

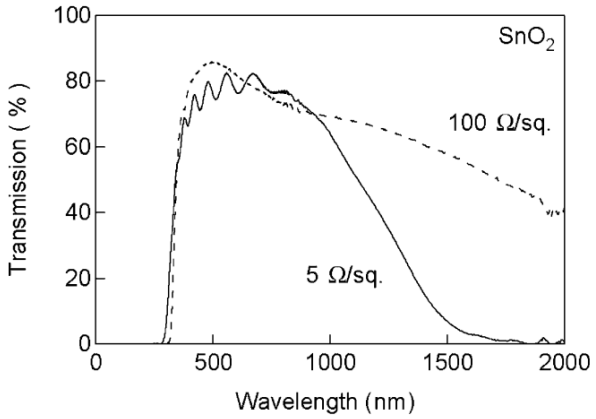

Figure 2.4. Optical spectra of a SnO_2-based TCO.[34]

Electrical conductivity in n-type semiconductors can be achieved by introduction of impurity atoms to the structure (doping) or by the creation of oxygen vacancies in materials such as oxides of indium, tin and zinc. Related ternary and quaternary compounds[35] have also been developed but the stoichiometry of these materials is difficult to control.[32] Until now most TCO materials have been developed based on single metal oxide compounds with the use of impurities; SnO_2 (doped with fluorine and antimony), indium oxide (In_2O_3, doped with tin) and zinc oxide (ZnO, doped with aluminum), but researchers have explored different configurations including complex non-stoichiometric compounds with dopants ranging from gallium to yttrium. Table 2.1[32] summarizes the different metal oxide configurations that have been explored and their dopants. It important to emphasize apart from the three first metal oxides in Table 2.1, these materials have not been viable for commercial applications. A schematic of the most

commonly used TCO host materials, SnO_2, ZnO, In_2O_3, CdO and GaO, is depicted in Figure 2.5.[36]

Table 2.1. Simple, binary, ternary and quaternary examples of TCO semiconductor materials and the impurity dopants

Material	Dopant or Compound
SnO_2	Sb,F,As,Nb,Ta
In_2O_3	Sn,Ge,Mo,F,Ti,Zr,Hf,Nb,Ta,W,Te
ZnO	Al,Ga,B,In,Y,Sc,F,V,Si,Ge,Ti,Zr,Hf
CdO	In, Sn
$ZnO–SnO_2$	Zn_2SnO_4, $ZnSnO_3$
$ZnO–In_2O_3$	$Zn_2In_2O_5$, $Zn_3In_2O_6$
$In_2O_3–SnO_2$	$In_4Sn_3O_{12}$
$CdO–SnO_2$	Cd_2SnO_4, $CdSnO_3$
$CdO–In_2O_3$	$CdIn_2O_4$
$MgIn_2O_4$	
$GaInO_3$, $(Ga, In)_2O_3$	Sn, Ge
$CdSb_2O_6$	Y
$ZnO–In_2O_3–SnO_2$	$Zn_2In_2O_5–In_4Sn_3O_{12}$
$CdO–In_2O_3–SnO_2$	$CdIn_2O_4–Cd_2SnO_4$
$ZnO–CdO–In_2O_3–SnO_2$	

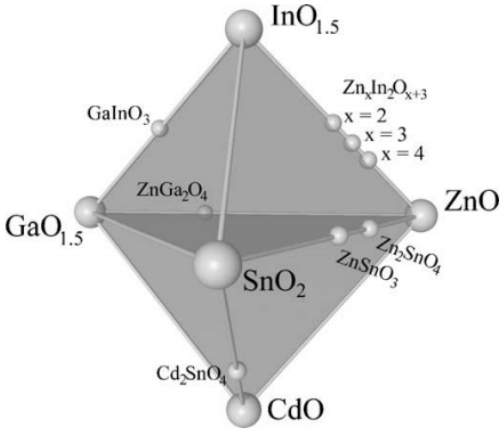

Figure 2.5. Schematic of common TCO host materials.[36]

The conduction band of intrinsic semiconductors is unfilled by electrons, but this changes with the introduction of the impurity atoms that have a lower (p-type) or higher (n-type) valence than that of host lattice atoms. This charge imbalance is “neutralized” by the abundance of holes (p-type) or electrons (n-type). In n-type semiconductors, the electron donors induce an increase in the Fermi level energy closer to the conduction band of the material where they can become free electrons, thus reducing the electronic resistivity of the material. This can be explained by the increase in energy of this impurity potential, which reduces or eliminates the energy barrier to the semiconductor energy band edge. Similarly, in p-type semiconductors, holes induce a decrease in the Fermi level energy closer to the valence band. In n-type semiconductors, these variations in the structure generate free carriers in the order of 10^{20} cm^{-3} and are positioned below or at the conduction band edge. Oxygen vacancies in the degenerate semiconductor have been found to be unstable at high temperatures, making impurity doping a preferred way to make TCOs. In n-type semiconductors that have been doped with metal impurities that can have various oxidation states (i.e. Sb^{3+} and Sb^{5+} in of oxide of Sn^{+4}), it has been found that at higher doping concentrations, both oxidation states can be present.[37,38] The ratio of these two states will then determine whether the material will be more (i.e. excess Sb^{5+}) or less (excess Sb^{3+}) conductive than the undoped material. An optimum doping level is therefore determined for each material at different synthetic procedures. Alternatively, it has been proposed that excess dopant atoms can favor the formation of dopant pairs or precipitation clusters where no free electrons are produced, limiting the conductivity gains seen in lower concentration doping levels, as depicted in Figure 2.6.[39]

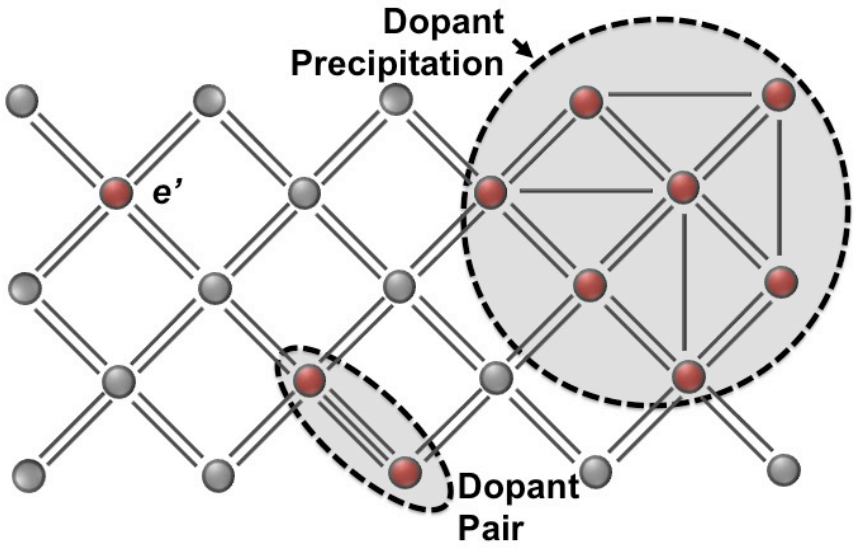

Figure 2.6. The effects of dopant aggregation in highly doped TCOs, limiting the effective free electrons in the lattice structure.[39]

2.2.2 SnO_2-based TCOs

Because of its relative low cost and the myriad of synthetic routes to prepare them, SnO_2-based TCO materials will be the main focus in the rest of this chapter. They are typically processed as thin polycrystalline compact films SnO_2 are commonly doped with fluorine (commonly known as FTO), and antimony (ATO), and similarly, indium oxide is doped with tin (ITO) to produce highly conductive TCOs. Due to their high production costs ITO materials are disadvantageous and many researchers have shifted attention to low-cost alternatives such as FTO and ATO. In the former, fluorine atoms replace oxygen sites in the lattice, and in the latter, antimony replaces tin, to make an n-doped semiconductor. TCO structures are suitable for a wide variety of applications such as solar energy conversion,[40-42] water splitting,[43] devices[44] and gas sensors.[45]

Table 2.2. Typical electronic properties of SnO_2 based compact thin films.[36]

	Doping Level (mol %)	Thickness (nm)	Resistivity (10^{-2} Ω cm)	Mobility ($cm^2V^{-1}s^{-1}$)	Carrier Concentration (10^{19} cm^{-3})
SnO_2	-	50	20	30	0.1
SnO_2:Sb	5	51	3.1	1.5 - 2	10
SnO_2:Nb	2	50	4	7	2.2
SnO_2:Ta	2	52	3.9	5	3.2
SnO_2:W	3	55	2.9	6	3.6

SnO_2 is typically of cassiterite (rutile) crystal structure exhibiting a body-centered tetragonal unit cell (Figure 2.7). The tin atoms are six coordinate and the oxygen atom three. At optimized conditions, SnO_2-based TCO materials can exhibit high Hall mobilities and carrier concentrations, low resistivity and high transmittance in the visible range, even at low temperature synthesis.[46] Typical electronic properties of these materials are summarized in table 2.2, for very thin films in the 50-55 nm range. Carrier mobility tends to decrease when doped with different metals whereas carrier concentration increases, with specially high number for the ATO samples.[36]

The interstitial substitution of Sn^{4+} atoms by Sb^{5+} in the SnO_2 lattice can be denoted as $Sn^{4+}_{(1-x)}Sb^{5+}_xO_{2ex}$. As summarized earlier and shown in Figure 2.6, the additional free electron from Sb^{5+} raises the carrier energy level into the conduction band of the semiconductor, thus increasing the conductivity of the material. The increase in charge carrier concentration gives rise to the Burnstein-Moss effect where the optical bandgap of SnO_2 is increased because the higher energy required to promote electrons from the valence band into an empty state in the conduction band.

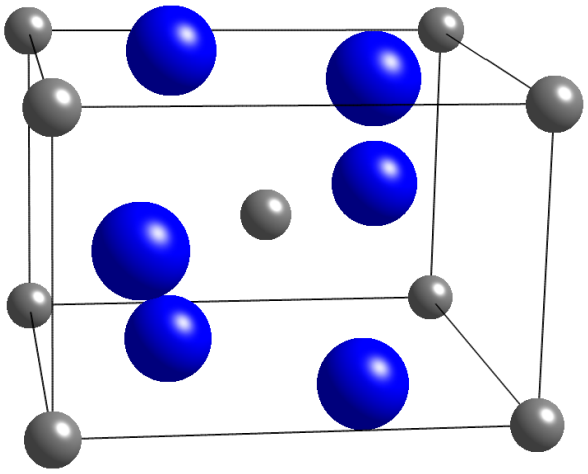

Figure 2.7. Body-centered tetragonal unit cell for rutile SnO_2. Grey spheres represent tin atoms and the blue ones oxygen.

ATO compact thin films can exhibit charge carrier concentration of about 10^{20} cm^{-3}, mobilities in the range of 1-30 cm^2 V^{-1} s^{-1}, and conductivities of about 10^3 S cm^{-1}. In addition, these materials have been extensively studied as a function of dopant concentration.[37,47-51] These high conductivity numbers are true for materials processed as compact films.[52,53] Processing materials porous nanoparticulate structures made out of ATO have also been studied, as they are interesting for applications where porosity, transparency and high conductivity are key. In compact ATO films the crystallite size are in the order of hundreds of nanometer, whereas in nanoparticle systems, the crystallites can be as small as a few nanometers. This makes a big difference in the conductivity because nanoparticles have a much higher number of grain boundaries, which in turn create electron scattering centers.[36,48,54,55] One of the most widely studied methods used to make these films is spray pyrolysis. Here, a precursor solution of tin and the dopant are sprayed on the heated substrate, typically above 400˚C, where the metals hydrolyze in-situ to form a film of the doped material.[54,56] A schematic cartoon of the spray pyrolysis method is shown in Figure 2.8 where a spray gun is held at a 45˚ angle at a certain

height from the hot plate.[56] Other researchers have synthesized highly conductive, stable nanoparticle sols, which are desirable for applications that require high surface area.[37,57] Nanoparticle systems are less conductive than their compact film counterparts due to grain boundary scattering, which limits electron mobilities.[54] However, the morphologies such sols can produce are desirable for applications that require high surface area and specific porosity.

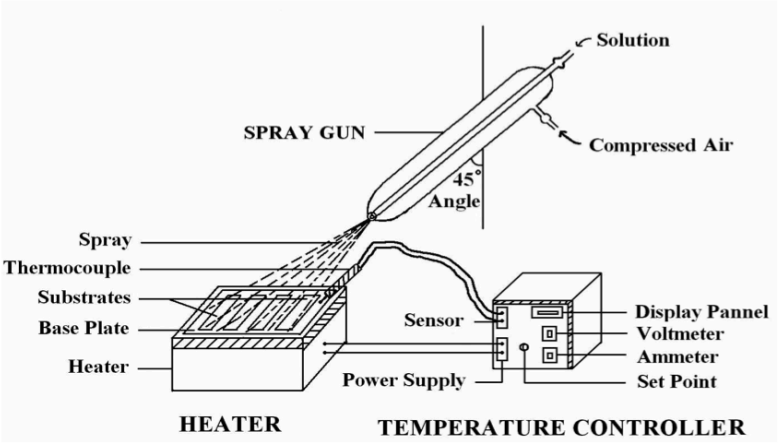

Figure 2.8. Schematic cartoon of a typical spray pyrolysis set.[56]

Because porous nanoparticulate materials are typically made into powders from sol-gel or precipitation reactions, it is difficult to make conductivity measurements due to a lack of a continuous path for electrons to travel. This is because the nanoparticles are not typically interconnected to allow electrode probes to conduct voltage-current measurements. Thus, pelletization of such nanoparticle powders has been widely used in order to compress the material and avoid empty spaces between the crystallites. Nutz et al.[48] for instance, synthesized and pelletized ATO nanoparticles containing 6% Sb in the precursor and compared them with the undoped analogues. They found that by simple refluxing of the particles at 100˚C, the resistivity did not change regardless of doping concentration. This changed, however, for samples that were autoclaved at 270˚C and pelletized where doping was found to decrease the resistivity by 5 orders of magnitude from about 10^{11} to 10^{6} Ω cm for particles in the order of 4-3

nm. A further and impressive decrease in resistivity was found after sintering the pellets at 900˚C to achieve 10 Ω cm. Goebbert et al.[55] studied the effect of temperature and time in the electrical resistivity of ATO nanoparticles pressed into pellets and found that it consistently decreases with the increase of both time and temperature. The lowest resistivity achieved was in the order of 10^{-2} Ω cm. Similarly, Mueller et al.[58] synthesized ATO nanoparticles in the range of 3-4 nm at 150˚C and found a decrease in electrical resistivity from 10^6 to 10^4 Ω cm for as prepared samples pressed into pellets. Annealing the materials at 500˚C has a dramatic impact on both undoped and doped materials; for the former a resistivity of about 10^5 Ω cm is found and the latter at 4% Sb rendered a resistivity of about 10^{-2} Ω cm. This shows the important role that temperature plays in producing low resistivity ATO materials, especially when processed as nanoparticles. The dramatic decrease in resistivity with temperature can be explained by an increase in particle sintering or interconnectivity. Furthermore, the release of organic compounds that can cause electronic barriers between the nanoparticles may aid in the improvement of the electronic properties.

In addition to a change in its electronic properties, Sb doping also changes the coloration of the materials from white for undoped materials to a range of colors for the doped counterparts. A blue coloration has been widely reported[48,49,59-61] but yellow and brown have also been shown.[37,62] This coloration effect has been suggested to be due to two phenomena. The first one is the decrease of the degenerate semiconductor's bandgap, which may occur due with the additional electrons and/or holes that are created by the introduction of the Sb impurities. Figure 2.8 adapted from Naghavi et al.[62] summarizes this effect where it is suggested that at low doping conditions (~10% Sb), a rather small change is seen in the bandgap electronic structure with only Sb^{5+} present. As the concentration of the Sb dopant is increased (20-30% Sb) Sb^{3+} is also incorporated degenerating the conduction band further and therefore reducing the effective bandgap of the semiconductor. At this point the addition of holes from the lower oxidation state

Sb may cause the quenching of the free electrons, thus increasing the conductivity. This in turn increases its absorption and the color of the material intensifies. At very high doping concentrations (>60% Sb) the holes may shift downward in energy, closer to the valence band of the semiconductor, which then enlarges the bandgap of the semiconductor leading to a decoloration of the material due to less absorption. The second approach to the free carriers is associated with Sb^{5+} doping. According with this theory the increase in absorption in the visible range can be explained by the intraband excitation or plasma absorption of free electrons in the conduction band of the semiconductor.[59,63]

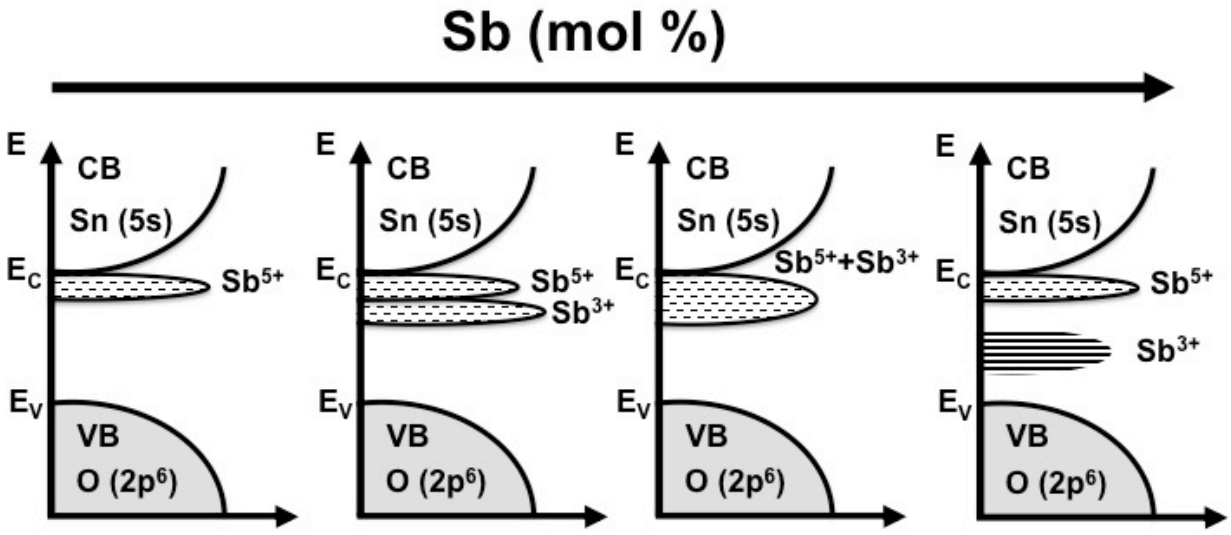

Figure 2.8. Suggested effect of increasing Sb in the band structure of ATO materials. From left to right the Sb concentration increases.[62]

2.2.3 Porous TCO Electrodes (TCE)

The use of 3D porous electrically conductive electrodes has attracted much attention in recent years. TCO nanostructure systems have been synthesized as nanorods,[64] mesoporous[65,66] and macroporous[67] materials. According with the International Union of Pure and Applied Chemistry the concept of porosity can be classified into 3 categories: microporosity (pores < 2 nm), mesoporosity (2-50 nm) and macroporosity (> 50 nm).[68] Meso and macroporosity are important

factors for applications that require large ions or molecules to diffuse through and to interact with the surface of the nanoparticle materials. In a review article by Hartmann,[69] the author stresses the important of mesoporous materials in bioabsorption and biocatalysis due to the improved diffusion over microporous materials. Aksu et al. used ITO mesoporous materials for bioelectrochemical applications.

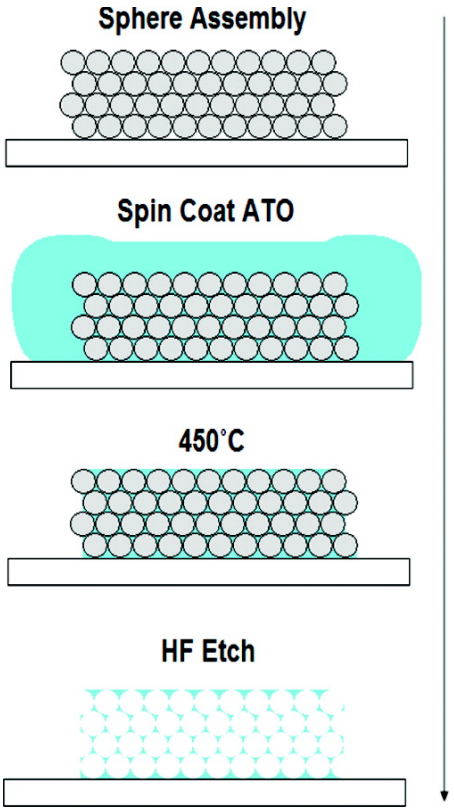

Figure 2.9. Processing route for making ATO mesostructures based on infiltration of ATO solution and the etching of silica nanospheres.[67]

Meso and macroporous materials are also interesting for improved diffusion of larger molecules such as organic compounds with large carbon chains (percolation of Spiro-OMeTAD in solid-state DSCs). Arsenault et al.[67] used silica spheres made by evaporation-induced self-assembly, a sol of ATO crystals was spin-coated and the structure was heated at 450°C. The silica template was etched by HF leaving the ATO-templated structure intact (Figure 2.9). The

structure yielded resistances in the range of 75 Ω and porosities of around 30%. The macroporous film functioned successfully as an electrooptical switch with many other potential applications.

Additional mesoporous TCO materials have been synthesized including self-assembled ATO structures made from preformed crystals. In this study the authors first prepared the conductive crystals (3-4 nm in diameter) and then used amphiphilic molecules to direct their positioning, creating a 3D array structure (Figure 2.10).[70] The formation of mesopores in this structure showed an improved electrochemical response attributed to the high surface area and the ability of ferrocene molecules to diffuse without major resistance. Other porous materials focusing on lithium batteries[71] and other energy storage applications[72,73] have been widely studied. These studies show that mesoporosity is not only important to the field of DSCs and now perhaps, perovskite solar cells, but also for a myriad of applications where high surface area and mesoporous nanoparticulate structures are vital for optimal performance.

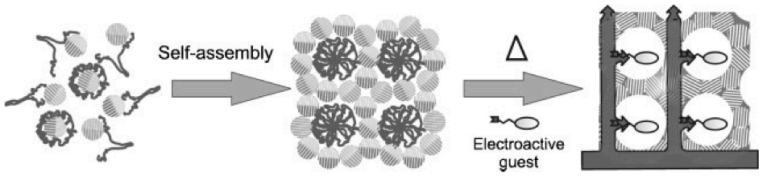

Figure 2.10. Schematic of the self-assembly process by amphiphilic molecules of ATO nanoparticles.[70]

2.3 Aerogels

Aerogels are 3D structures composed of arrays of nanoparticles that have high surface area, high porosity and good particle interconnectivity.[74] These are processed as sol-gels where a catalyst causes the gelation of the sol, commonly at low temperatures. Acid and base-catalyzed silica aerogels have been widely studied, yielding impressive properties such as high surface

area and high porosity.[75] While most wet gels are dried by evaporation of the solvent, thus obtaining so-called xerogels, aerogels are dried by driving the solvent in the pores above its critical point, a process called supercritical drying (SCD). This process produces a dry porous structure whose morphological characteristics resemble that of the original wet get. The dried materials exhibit low apparent density with very high surface area and pore volume, with pores in the micro and mesoporous range. Figure 2.11 (left) shows a schematic of an aerogel structure with interconnected particles and large open pores.[76] A SnO_2 aerogel TEM image exhibits the mesoporous features with particles in the range of 3-5 nm (right).

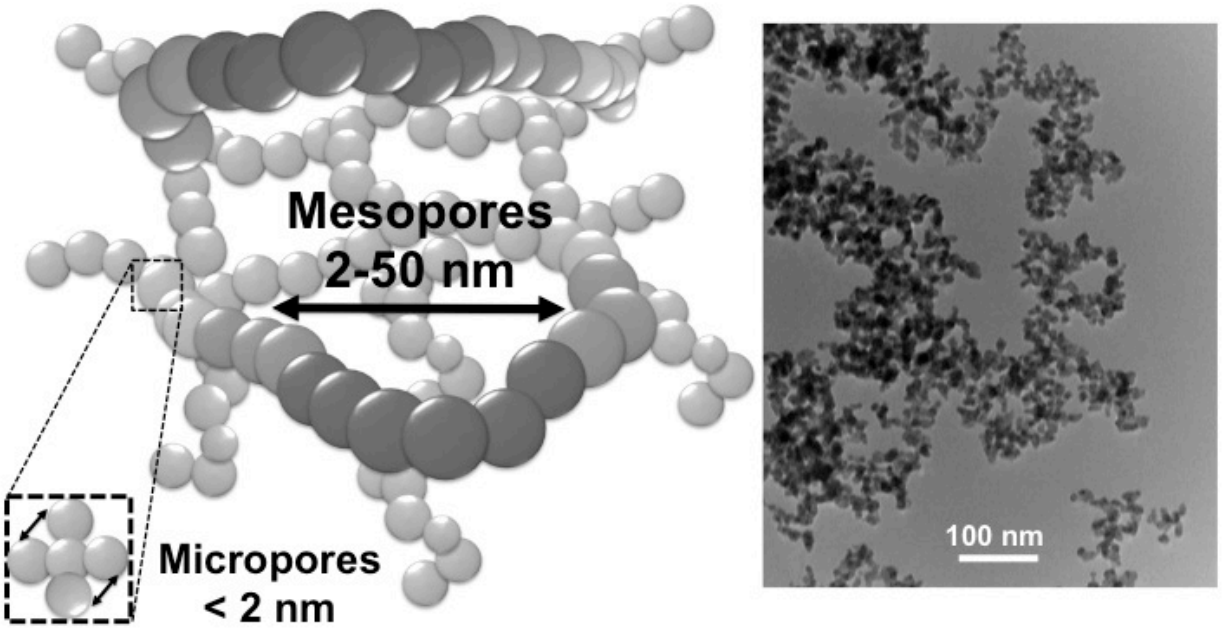

Figure 2.11. Schematic of an aerogel structure with meso- and micropores identified (left).[76] TEM image of a SnO_2 aerogel showing features typical of aerogel structures (right).

2.3.1 Sol-Gel Process

Sol-gel processing refers to the chemical process of creating an array of particles from either colloidal particles or from precursor ions in solution. Most of the inorganic synthetic process of sol-gel involves metal oxide particles, where the metal atoms polymerize by the creation of M-

OH and subsequently M-O-M bridges. This polymerization leads to the creation of particles that at a first form a suspension distributed evenly in the solvent (i.e. the sol). Next the particles can crosslink thus creating the 3D structure of interconnected particles (i.e. the gel) as seen in the TEM image of SnO_2 aerogels (Figure 2.11, right). This transformation of sol to gel is called gelation and is often induced by a catalyst. Alternatively to the direct formation of a 3D array of particles from ions in solution, is first the formation of a colloidal solution of nanoparticles, which is then catalyzed to form that same structure. In this thesis the focus will be given to former process, as it is the one used in the synthesis of the SnO_2 gels in this thesis.[74]

The most common sol-gel process involves the use of metal salts, which in solution are present as ions that in the presence of water become hydrated, $M[H_2O]$. Livage and coworkers proposed a mechanism described by Figures 2.12 and 2.13.[77] In the gelation phase, hydrolysis replaces the H_2O, releasing a proton and creating the M-OH bond, which is also called olation (from "ol" or OH).

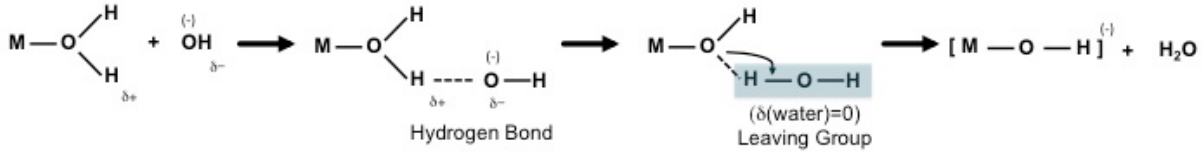

Figure 2.12. The olation process from a hydrated metal salt producing a metal hydroxide group.[77]

The combination of 2 M-OH groups in turn create the M-O-M group, also called oxolation (from oxygen), releasing water in the process.

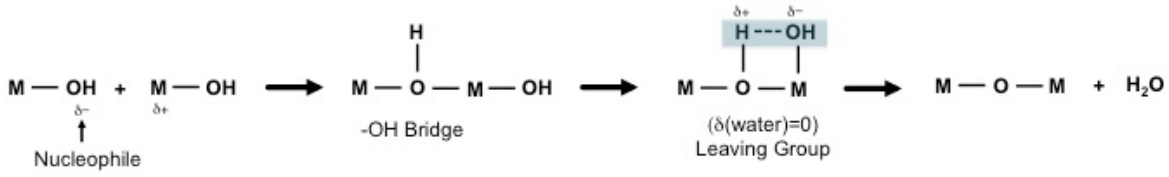

Figure 2.13. In the oxolation process 2 metal hydroxide groups combine to finish the polymerization process.[77]

2.3.2 Epoxide Catalyzed Sol-Gel

The process just described can be catalyzed with a base, which slowly reacts, and crosslinks with the M-O bridges taking hours or days.[78,79] Alternative catalysts to the traditional acid and base have been recently used, including the epoxide assisted sol-gel method which has attracted much attention due to its ease of processing. Gash and coworkers developed this synthetic route to synthesize iron oxide (Fe_2O_3) aerogels using various solvents, Fe:propylene oxide (PPO) and H_2O:Fe ratios, and iron precursors. They found that a ratio of 11:1 of PPO:Fe produced proper gelation of most solutions. A requisite of 6:1 H_2O:Fe was established in order to induce gelation; lower ratios produced no gels. The hydrated metal is deprotonated by the epoxide, which links it with other hydrated metals via olation and oxolation to form metal oxide particles, as just described. These in turn crosslink to form a 3D array of particles, otherwise called a monolithic wet gel.[80] Propylene oxide has been widely used in organic chemistry as an acid scavenger, which is rapidly protonated via the epoxide oxygen followed by subsequent ring-opening. According to the report by Gash et al.[80] the PPO extracts a proton from the hydrated Fe ion and in this case a Sn ion, as follows,

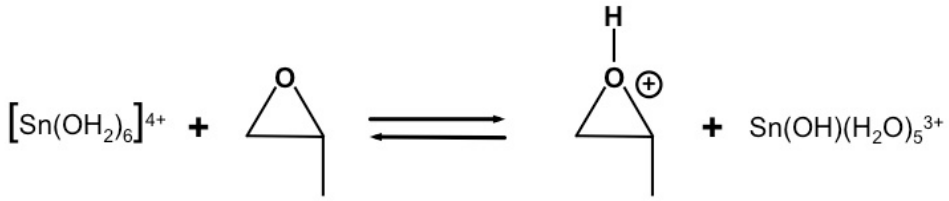

The protonated species above can then go through 2 reactive scenarios described below (process a). Water can attack a ring carbon, opening the ring structure and releasing a proton generating 1, 2-propanediol. This process is catalytic in protons and thus these are not

consumed in the process. Therefore this reaction will not lead to the olation/oxolation process, which produces the SnO_2 structure. For solutions containing chlorine ions, which is known to be better nucleophile than water, PPO is ring opened by it to form 1-chloro-2-propanol (process b) without proton regeneration as in process (a).[80]

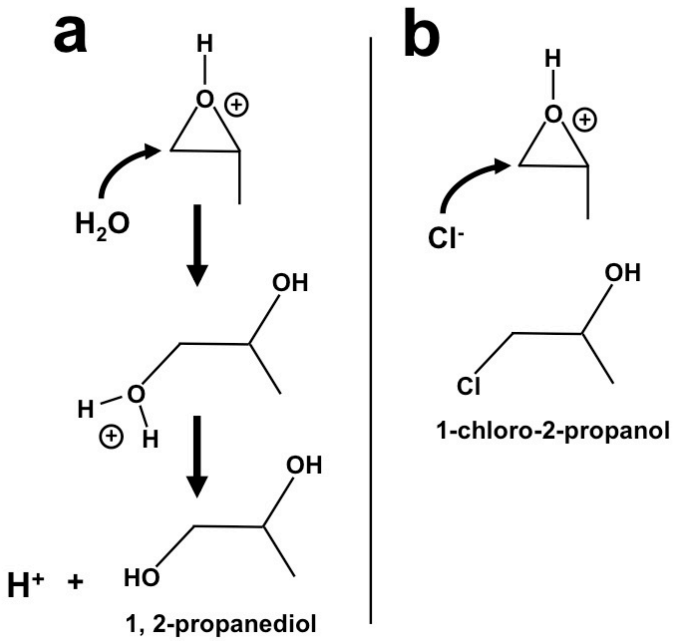

The gradual deprotonation of the material leads to the formation of Sn-OH bridges and finally to Sn-O-Sn bridges which are product of the sol-gel processing.

The Fe_2O_3 gels produced by this sol-gel process were dried supercritically to produce monolithic aerogels. This synthetic procedure produced particles in the range of 5-10 nm, high surface areas of 300-400 m^2g^{-1}, and pore sizes in the mesopore range (2-23 nm).[80] This first study on the epoxide assisted sol-gel preparation of Fe_2O_3 opened the doors to a large number of other metal oxides that can prepared in the same manner, with the advantage of a relatively fast gelation time. This sol-gel process has been used to make many other materials including zinc oxide (ZnO)[81] where high surface area (>100 m^2g^{-1}) was measured for the aerogel materials.

Fe_2ZnO_4 aerogels were synthesized by this method and SCD and high surface areas were also measured.

SnO_2 aerogels have been synthesized by other methods yielding low density and high surface areas and pore volumes.[82] However, this process involves a complicated and lengthy synthetic route including solution decanting until achieving a pH of 4. Instead, the epoxy-assisted sol-gel process for SnO_2 is quick (1-20 minutes) and only involves dissolving the Sn salt in water and ethanol and adding PPO.[83] Baumann and coworkers first used this process for SnO_2, achieving high pore volume (2.3 cm^3g^{-1}) and surface area (383 m^2g^{-1}), mesoporosity (pore diameter of 20 nm), and particle size in the range of 3-5 nm. Davis et al. produced ITO aerogels using glycidol (a compound that contains both epoxide and alcohol functional groups) as the catalytic agent with metal salts of indium and tin in the precursor solutions.[84] The samples were annealed at 600˚C in order to achieve crystallinity of the material. The structure exhibited high surface area for the as-prepared sample (117 m^2g^{-1}) but it decreased dramatically to 39 m^2g^{-1} for the annealed samples. The same phenomenon occurred for pore volume, which decreased from 0.33 to 0.16 cm^3g^{-1} for as-prepared and annealed samples, respectively. The former is indicative of particle growth, although there is no report on crystallite size from the XRD patterns, and the latter might be due to severe shrinkage of the structure as it is heated to 600˚C.

In the report by Baumann et al, no characterization was done at high temperatures. It is therefore unclear from these reports whether shrinkage is a general trend in the epoxide assisted processing of aerogels, which is crucial in obtaining the properties that are desirable in an aerogel. More importantly, shrinkage is vital for the proper processing of aerogels casted as thin films. Even small shrinkage can cause the delamination of the films. This will be an important part in this dissertation and the next chapter (3) will be dedicated to understanding the implications of calcining in SnO_2 aerogel shrinkage. The subsequent chapters will focus on the effect of conductivity in the ATO aerogels in the bulk and as films for applications in DSCs.

3 Methodology

In this chapter the general experimental procedures will be described for all subsequent chapters, as many of these descriptions apply to most experiments. The details that are specific to each chapter will be described separately within that chapter. This part of the thesis will be divided into the sol-gel processing, including bulk and thin film monolithic aerogels, materials and solar cell characterization. The general synthesis process of bulk aerogels is summarized in a schematic (Figure 3.1) and explained step by step throughout Section 3.1 below. Similarly, the process involving casting aerogel films is depicted in a schematic (Figure 3.2) and will also be described below.

3.1 Aerogel Processing

3.1.1 Sol-Gel and Supercritical Drying

All chemicals were purchased from Sigma-Aldrich, unless noted otherwise, and were ACS grade or better. In a typical procedure, 0.6 M $SnCl_4 \cdot 5H_2O$ is dissolved in absolute ethanol and stirred for 2-3 hours at room temperature. The Sn solution is placed in a water bath at 60°C and a 7 M NH_4F aqueous solution is added dropwise. The amounts of the fluorine precursor are varied over a F:Sn ratio of 0:1 to 1:1for the purpose of studying its effect on the SnO_2 aerogels (Chapter 4). The addition of NH_4F forms a white precipitate, which redissolves in solution after 3-4 hours of stirring in the water bath.[85] For the purpose of making ATO gels, $SbCl_5$ is dissolved in HCl (37%) at 2 M. The antimony is admixed in the Sn solution at different mole ratios labeled as x% Sb, where x = [Sb]/[Sn], ranging from 0-40%.

Typically, propylene oxide (PPO) is added to the solution in an ice bath at a PPO:Sn ratio of 11:1.[80] The gelation occurs after PPO addition but the time varies with the amount of F. The reaction is allowed to proceed 20-60 minutes in a capped vial, which is

subsequently filled with ethanol to age for 24 hours. The solvent and by-products are then washed with acetone 3 times over 3 days. The gels are transferred to a custom-built pressure vessel, which is filled with liquid CO_2. The acetone is washed out by the liquid CO_2 over the course of 3 days and the vessel is heated above the critical point of the CO_2 (T~31-32˚C and P~ 7.38 MPa). The temperature and pressure are held constant at about 45˚C and 9MPa, respectively, for 1 hour and then depressurized over 3 hours to room temperature and pressure. The samples are then calcined at different temperatures, mainly at 450˚C and 800˚C, in air for 30-360 minutes after heating at a rate of 3˚C/min.

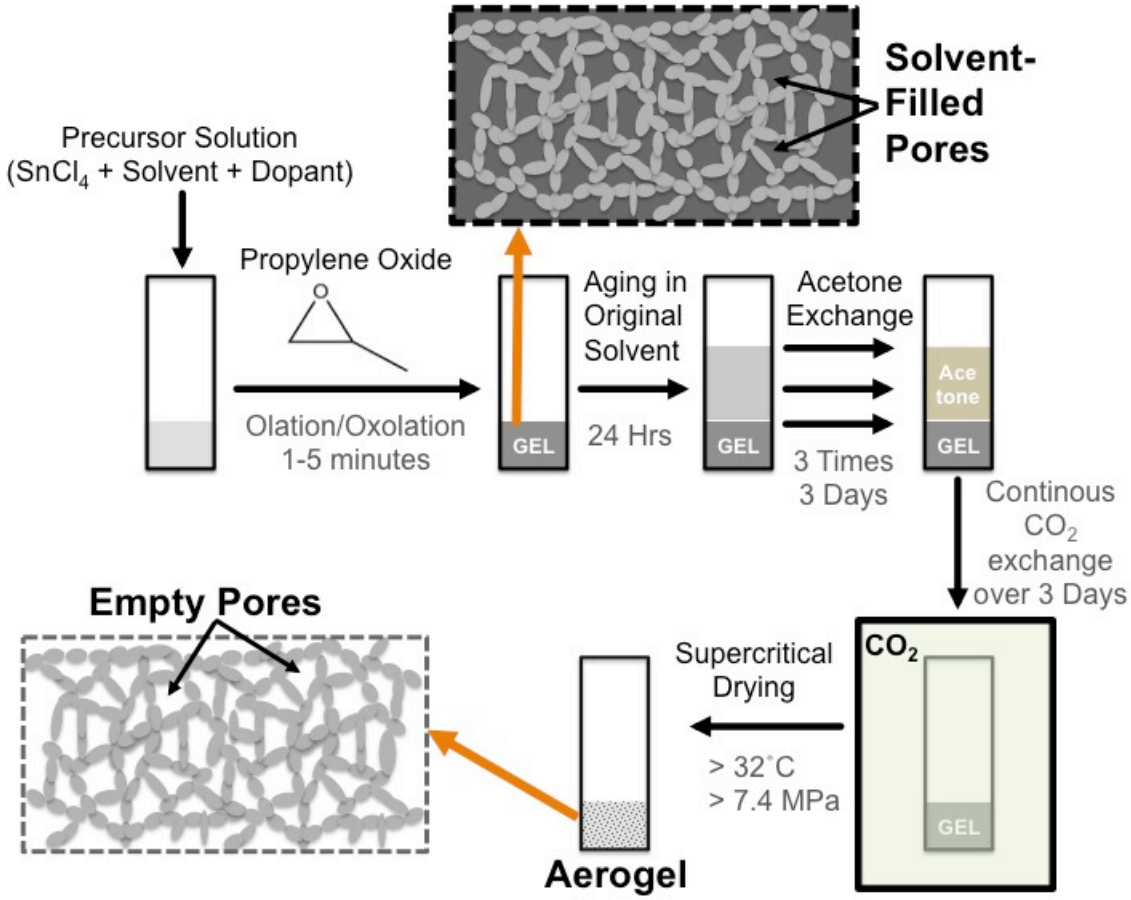

Figure 3.1. Schematic of the aerogel processing. The sol-gel process of SnO_2 and ATO is catalyzed by propylene oxide yielding a wet gel of interconnected particles and solvent in filling the pores. Acetone washes out the original solvent and reaction byproducts and it is then substituted by liquid CO_2 in a high-pressure vessel. The vessel is heated above the critical point of CO_2 and slowly depressurized isothermally to yield the aerogel structure.

3.1.2 Processing of Aerogel Thin Films

In order to make films of ATO and SnO_2 aerogels, the sols must be cast on glass before the gel point and a schematic of this process is shown in Figure 3.2. At 75 s before the gel point (which is typically ~150 s after PPO addition), 8 μL of the sol are deposited onto a borosilicate glass or a FTO glass with a masking tape frame of 1 x 1 cm^2 (Figure 3.2 left). Each vial containing 615 μL of the sol can yield up to four films in order to obtain more repeatable results, because the gelation occurs rather fast and this means a more viscous sol and presumably a thicker film. The films are immediately covered with a piece of glass in an ethanol-saturated chamber to prevent the solvent in the gels from evaporating during the gel formation process (Figure 3.2 right). The films were aged for 8 minutes and subsequently immersed in ethanol where they remained for 24 hours before being washed with acetone 3 times over the course of 24 hours. As described above for bulk wet gels, the thin film samples (immersed in acetone) are transferred to a custom-built pressure vessel, which is filled with liquid CO_2, where the acetone is displaced by the liquid CO_2 and then supercritically dried. The samples are heated at 450˚C for 30 minutes on a titanium hot plate.

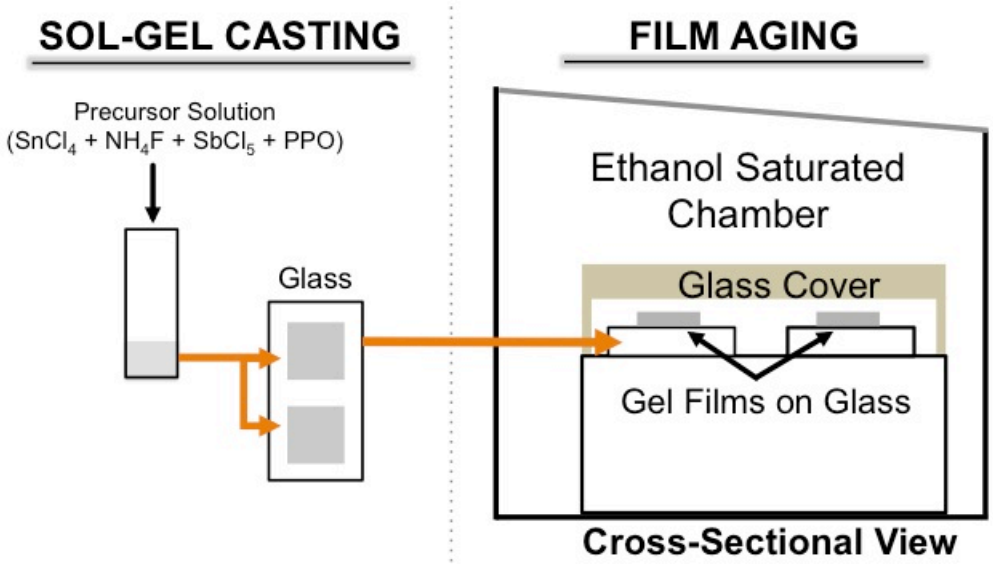

Figure 3.2. Schematic of the deposition of the sol onto a glass in 1 × 1cm^2 frames (left) and subsequent aging in an ethanol-saturated chamber under a glass cover (right).

3.2 Materials Characterization

Details on the characterization of bulk aerogels are described herein. The experimental analyses described are aimed at understanding the chemical processes that happen in the synthesis of the material and the effects of the chemical configurations on the materials' absorptivity and conductivity. The aerogel morphology, crystal structure, elemental analysis and electronic properties were determined by an array of techniques.

3.2.1 Thermogravimetric Analysis

The effect of temperature on the weight of the aerogel materials was studied using thermogravimetric analysis (TGA). The measurements were completed using a TA Instruments TGA Q-500 at a heating rate of 3 ℃ min^{-1} to 800 ℃ in air environment.

3.2.2 Temperature Programmed Desorption

To understand the effect of dopants in the SnO_2 aerogels by observing volatilized molecules from the material, temperature programmed desorption mass spectrometry

(TPD-MS) was used. The measurements were performed using a MKS PPT quadrapole Residual Gas Analyzer equipped with a vacuum sampling manifold that allows for the analysis of gas streams at or near atmospheric pressure. Powderized samples were loaded into a quartz tube and placed inside a programmable tube furnace. A 500 sscm flow of argon was maintained while the sample temperature was ramped at a rate of 10 °C/min. from room temperature to 800 °C.

3.2.3 Electron Microscopy

Scanning electron micrographs were acquired with a FEI Quanta FEG250 SEM in high vacuum mode, and were used to study the morphology of the bulk, thin film and pelletized aerogels. Energy dispersive x-ray spectroscopy (EDX) was used to quantify different elements, although this technique proved difficult for quantification of Sb since its peaks overlap with those of Sn.

Transmission electron micrographs (TEM) were acquired with a FEI Tecnai T12 S operated at 120 kV accelerating voltage and was used to study particle shape and size. Samples were prepared by a very diluted dispersion of the aerogel materials in ethanol with sonication for 30 minutes. The dispersion was then deposited on a carbon grid (Ted Pella, Inc. pure carbon film 200) and dried in air.

3.2.4 X-ray Diffraction Analysis

In order to analyze the crystallite phase, lattice structure and size the samples were crushed into powders and placed into a holder for analysis by x-ray diffraction (XRD) using a Bruker D8 Advance X-ray diffractometer using Cu Kα radiation (λ = 0.154178 nm) at a scanning rate of 0.02˚ s^{-1} in the 2θ range from 20˚ to 80˚. Miller indices were assigned to the peaks by comparing the diffracted patterns to those found in the

literature. The crystallite size of the SnO_2-based materials was determined by the Scherrer equation[86]

$$D = \frac{0.9 \cdot \lambda}{\beta \cdot cos\theta} \quad (1)$$

where D is the crystallite size, λ is the X-ray wavelength, β is the full width at half maximum (FWHM) and θ is half of the angle of diffraction. Additionally, the d-spacings of the materials can be calculated from Bragg's diffraction law[87]

$$\lambda = 2 \cdot d \cdot sin\theta \quad (2)$$

3.2.5 X-ray Photoelectron Spectroscopy

Elemental composition was determined by X-ray photoelectron spectroscopy (XPS) with a PHI 595 Multiprobe system using an aluminum anode system with Kα=1486.6 eV. Ground aerogel samples were placed and analyzed on a double-sided carbon tape. The spectra were corrected for sample charging effects using the C1*s* peak at 284.6 eV. The Sb $3d_{5/2}$ peak overlaps with the O 1*s* peak at a binding energy of about 531 eV, and therefore the Sb $3d_{3/2}$ peak is used to quantify the extent of doping. This will be further illustrated in Chapter 5.

3.2.6 Nitrogen Physisorption

Nitrogen adsorption/desorption measurements were carried out in a Micromeritics ASAP 2020 accelerated surface area and porosimetry analyzer. The isotherms were analyzed by the software to determine the Brunauer-Emmett-Teller (BET) specific surface area, Barrett-Joyner-Halenda (BJH) pore volume and size of the different SnO_2 materials. This technique was especially useful in Chapter 4, where the shrinkage of the aerogel structure is studied, but it is also used in Chapter 5 to understand the effect of the precursor antimony in the structure of the aerogels.

3.2.7 Four-Point Probe Measurements

The resistivity (ρ) of aerogel monolith and the pelletized counterparts was determined by the common 4-point probe technique.[88] A set of 2 μm tungsten needles were placed in-line with needle spacings of 600 μm atop the monolithic aerogel disks (1.2 cm diameter by 1 cm in height) and room temperature resistance was obtained from low voltage IV curves (-0.5 to 0.5 V) through the aerogel structure using the formula

$$\rho = 2\pi s F \left(\frac{V}{I}\right) \quad (2)$$

where s is the spacing of the probes (0.6 mm), F is the correction factor dependent on sample geometry (taken as unity due to the large size of samples compared to the probe spacing), and V/I were extracted from the probe measurements.

3.2.8 Diffuse Reflectance Spectroscopy

Diffuse reflectance spectroscopy (DRS) was used to understand the effect of Sb doping in the reflective characteristics of the material which is proportional to its optical bandgap and therefore its absorptivity. DRS measurements of aerogel powders diluted 10 times in barium sulfate were made using a Shimadzu UV-2450 UV-vis spectrometer with an IRS-2200 integrating sphere. Data were plotted as Kubelka-Munk versus wavelength using the function $F(R) = (1-R)^2/2R$, where R is the observed reflectance.

3.3 Aerogel Thin Film and DSC Characterization

Aerogel thin films were processed for use as conductive scaffolds in DSCs. The sintered particles were coated with a thin conformal layer of TiO_2 by atomic layer deposition. The composite materials were sensitized with a dye and their IV characteristics were measured as were their electron kinetics. In this section, these techniques will be presented in detail.

3.3.1 ALD Coatings

A Savanah ALD 100 instrument (Cambridge Nanotech Inc.) was used to deposit TiO_2 over the aerogels. The deposition was carried out at 200˚C with exposure times of 14 and 7 seconds for titanium isopropoxide and water, respectively. The chamber was flushed with nitrogen for 30 seconds between cycles to remove byproducts. The samples were then heated at 500˚C for 15 minutes.

3.3.2 Film Characterization

The aerogel films were scraped with a razor blade to obtain an active area of approximately 0.24 cm^2. The film thickness was measured with a Dektak stylus profiler. The change in morphology due to ALD processing was observed with SEM imaging (FEI Quanta FEG250 SEM in high vacuum mode). The crystal structure of the samples was analyzed by XRD using a Bruker D8 Advance X-ray diffractometer as described above. Ellipsometry (M-2000 V spectroscopic ellipsometer) was used to estimate the ALD deposition rate on a clean borosilicate glass slide (Fisher Scientific) after 300 ALD cycles and heating at 500˚C for 15 minutes. The obtained spectra were fitted by using the Cauchy model with the Completeease 4.32 data analysis software (J. A. Woollam Co., Inc) to extract the thickness of deposited TiO_2.

3.3.3 Sensitization

The films were immersed for 24 hours in 0.5 mM D149 (an organic indolin dye) in a 1:1 mixture of acetonitrile and *tert*-butyl alcohol. To measure the amount of D149 dye adsorbed by a film, a dyed and rinsed 0.24-cm^2 electrode was placed in 3 mL of *N,N*-dimethylformamide (DMF). The spectrum of the desorbed dye was measured in a 1-cm quartz cuvette using an Agilent Cary 50 spectrophotometer. Dye concentration was calculated using the peak extinction coefficient[89] for D149 in acetonitrile/*tert*-butanol (1:1) of 6.87 x 10^4 M^{-1} cm^{-1}.

3.3.4 Solar Cell Assembly

In order to have a working solar cell three main components are needed: a photoanode with sensitized nanoparticles, a platinized counter electrode separated by plastic spacers (Figure 3.3) and a liquid electrolyte in between. The counter electrode was made by depositing a Pt solution on FTO glass with two pre-drilled 1-mm holes, then heating it at 400˚C. The working electrodes were sealed against platinized counter electrodes on a hot plate at 120 °C using a hot-melt plastic frame or spacers (Solaronix, Meltonix 1170, 25 µm thick). The electrolyte was introduced through one of the two holes in the counter electrode, while the other hole allowed air to escape. Both holes were then sealed using hot-melt plastic and a thin glass cover slide. The exposed conducting glass of each electrode was coated with silver paint for improved electrical contact (Figure 3.3)

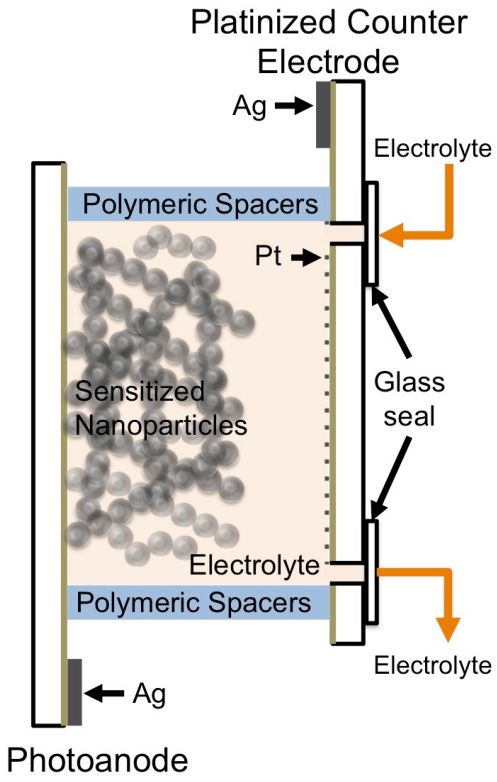

Figure 3.3. Schematic of a "sandwich" DSC including all major components: FTO glass coated with sensitized semiconductor nanoparticles, a platinized counter electrode, spacers between the two electrodes and the liquid electrolyte in between.

3.3.5 Electrolyte Composition

The I^-/I_3^- electrolyte was prepared with 0.5 M tetrabutylammonium iodide and 0.05 M iodine (I_2) in 3-methoxypropionitrile. The Fc/Fc^+ electrolyte contained 0.1 M ferrocene and 0.05 M ferrocenium hexafluorophosphate in 3-methoxypropionitrile. The Fc/Fc^+ electrolyte was prepared fresh and deoxygenated by bubbling nitrogen 10 min prior to cell fabrication to minimize reaction of ferrocene with oxygen.[90]

3.3.6 Solar Cell Characterization

Solar cell performance analysis was done by current density−voltage (*J*−*V*) measurements using a Keithley 2400 source/meter controlled by a PC, while irradiating at 100 mW/cm^2 (1 sun) with AM 1.5G simulated sunlight produced by a solar simulator (Newport 91160), calibrated against a silicon reference cell with KG5 filter (PV Measurements, Inc., Boulder, CO). The DSC active area was 0.24 cm^2.

3.3.7 Transient Measurements

Electron kinetics measurements were used to understand the fundamental processes of electron transport and lifetime, which determine the electron collection efficiency. Measurements of electron transport time were made based on the transient decay of the photocurrent upon square-wave modulation of a white-light LED as described previously[91] except in parallel with a 40-Ω resistor. Electron lifetime was measured in an analogous way based on the voltage transient at open circuit.

4 Effects of Fluorine in the Shrinkage of Tin Oxide Aerogels

In this chapter, the effect of fluorine on aerogel shrinkage will be discussed. Fluorine plays an important role in the processing of aerogel thin films because without it films delaminate or suffer from severe shrinkage. A thorough investigation of the chemistry involved in the addition of F in the precursor will be presented.

4.1 Introduction

The morphology of nanostructures is known to affect the properties of the materials in different applications, and it has become a key component in the synthesis of nanoparticulate configurations.[92,93] In order to take full advantage of such materials one must be able to manipulate the pore structure, surface area and particle size and crystallinity. Aerogels are 3D monolithic structures made of networked nanoparticles that exhibit high surface area, high porosity, and good particle interconnectivity. These structures are interesting because of the relative ease with which one can tune their physical properties.[79,94] Aerogel materials have been studied extensively, with a large portion of research focusing on silica,[74,75,95] which has been used as scaffolds for semiconducting metal oxides in solar cell devices.[96-98] Metal oxide aerogels have also been synthesized, including titania, zirconia and niobia[94] and other semiconducting materials.[99]

Tin dioxide (SnO_2) is a n-doped, wide bandgap (3.6 eV at room temperature) semiconductor widely used in solar cells,[100-102] water splitting,[103] optoelectronic devices,[104] gas sensors,[105] and transparent conducting oxides (TCOs).[106] Different types of SnO_2 structures have recently been produced including nanobelts,[107] nanowires[108] and nanoparticles.[109] SnO_2 aerogels have been produced by sol-gel processing with a facile epoxy-assisted method exhibiting high surface area with particles in the range of

3-5 nm.[110] This type of structure is ideal for dye-sensitized[7] or perovskite solar cells[28,111] where an open-pore structure, nanoparticle 3D array is the backbone for electron transport through the photoanode film before reaching the TCO glass. However, in order to achieve proper casting of an aerogel film on glass, it is imperative to minimize the aerogel shrinkage during the processing.

Silica aerogel shrinkage during processing and critical drying (SCD) has been identified and studied.[79,112,113] SnO_2 aerogel shrinkage has only been studied during the CO_2 exchange,[82] but no work has been done on aerogel monolith shrinkage after annealing at high temperatures, which is crucial in obtaining highly crystalline nanoparticles. High synthesis temperature is especially useful when doping with fluorine (FTO)[57] or with antimony (ATO) to achieve optimal conductivity of the materials. Uncalcined ATO nanoparticles for instance, can exhibit resistivities several orders of magnitude higher than those calcined at high temperatures.[37,48,55] High temperatures are also important for making porous TCO electrodes[70] and those coated with other materials that require high temperature to become crystalline, such as TiO_2.[51] It is therefore important to understand the underlying mechanisms that prevent these SnO_2 aerogels from shrinking throughout processing in order to take full advantage of the material's properties. In this study, we synthesized SnO_2 aerogels by the epoxide-assisted sol-gel process and dried them supercritically. Fluorine (NH_4F) was added to the precursor solution in different amounts to study its effect on the aerogel shrinkage and density, porosity, surface area, optoelectronic characteristics and chemical composition.

4.2 Results and Discussion

4.2.1 Aerogel synthesis

Thin films of SnO_2 aerogels were deposited on glass before the gelling point. It was found that without the addition of F, wet gels casted on an FTO glass would delaminate from the glass or become severely cracked upon supercritical drying. With a precursor F:Sn of 1:1 the films remained attached to the glass through the SCD process and after calcination at 450˚C. It was noticed then, that the bulk gels without F suffered from severe shrinkage through the SCD and calcination steps. These results prompted a thorough investigation of this effect.

Table 4.1 shows aerogel samples produced different concentrations of precursor F. The increase in fluorine consistently decreased the gel time from 300 seconds for unfluorinated samples to 105 for samples containing 1:1 of F:Sn. Similar trends have been observed where silica solutions gel faster with the addition of F precursors.[79,114,115] The effect of F in gelation times of silica has been studied and it is well known that F catalyzes the gelation process, however, the mechanisms that drive this are still not well understood.

Table 4.1. Effect of NH_4F in sol-gel processing and shrinkage ($\partial V/V_0$) of aerogels after supercritical drying (SCD) and calcination at 450˚C.

F:Sn	Gel time (sec)	$\partial V/V_0$ (%) After SCD	$\partial V/V_0$ (%) 450˚C
0.25:1	240.00	39%	88%
0.5:1	180.00	32%	85%
0.75:1	150.00	17%	78%
1:1	105.00	7%	73%

Cylindrical monolithic aerogel volume was measured for samples containing varying amounts of F after the SCD processing and calcination steps. The samples suffered from shrinkage during the ethanol and acetone exchange step even before SCD, with most shrinkage occurring in samples with less F. It has been hypothesized that this effect is due to the reorganization of clustered nanoparticles as solvents diffuse through the pores.[116] Samples with 1:1 F:Sn exhibited no apparent shrinkage during the solvent exchange step. The measured shrinkage for samples with varying concentration of F after the SCD and calcination steps is presented in Table 4.1. For the former, a significant shrinkage was measured for samples with less or no F with a 37% shrinkage at 0.25:1 F:Sn, while samples with 1:1 F:Sn showed relatively small shrinkage at 7%. Calcination of all aerogel materials at 450˚C yielded severe shrinkage for all samples, although samples with 1:1 F:Sn had the lowest shrinkage at 73% compared to 88% for samples at 0.25:1. Even if the bulk shrinkage of all aerogels is very large, the decrease in shrinkage from 88 to 73% for 0.25:1 and 1:1 F:Sn, respectively, is enough to prevent delamination of thin films.[51]

4.2.2 Elemental Analysis

Elemental analysis was performed by XPS for aerogel samples containing a precursor F:Sn of 1:1, uncalcined and calcined at 450˚C for 30 min and 800˚C for 6 h (Figure 4.1). Survey scans were performed to quantify the Sn and F in the aerogel material. Tin peaks corresponding to Sn $3d_{3/2}$ and $3d_{5/2}$ were found at 495 and 488 eV, which corroborates the oxidation state of Sn(IV).

The effect of temperature on the weight of the materials was studied by TGA (Figure 4.1). Fluorinated samples exhibit a sharp drop between room temperature and 170 degrees, followed by a second, less rapid mass loss between 170 and 350 °C. The

unfluorinated sample exhibits a more gradual mass loss between room temperature and 200 °C, followed by a rapid decrease between 200 and 350 °C.

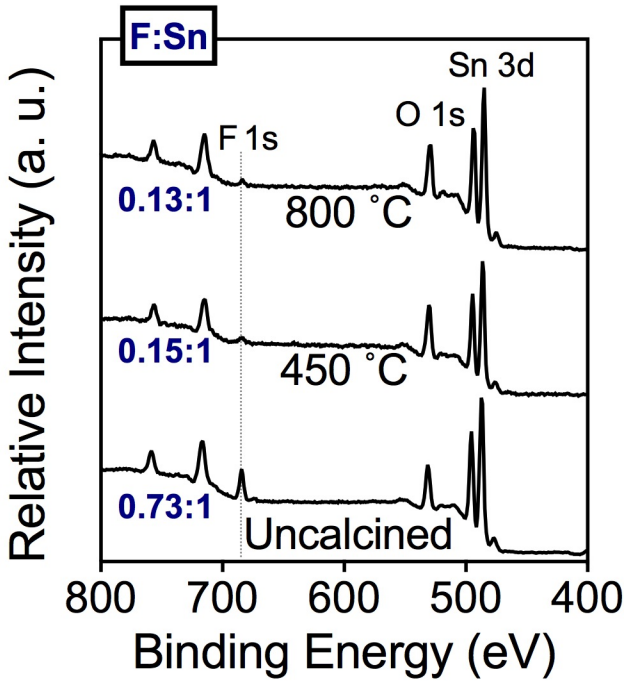

Figure 4.1. X-ray photoelectron spectra showing the Sn 3d, O 1s and F 1s peaks as a function of heat treatment after supercritical drying, for samples with precursor F:Sn of 1:1.

TPD-MS (Figure 4.2) experiments were completed to identify the species evolved during the heating process. A significant portion of the mass lost from the fluorinated sample (Figure 4.2b) is due to water evolution (m/z = 18). The broad signal between room temperature and 250 °C is due to surface adsorbed water. This is followed by a second less intense peak that is due to water being removed from the mesopores of the material and surface hydroxyl groups condensing to form Sn-O-Sn linkages and releasing water. A similar desorption profile is observed for m/z = 17 due the fragmentation of water to –OH when exposed to the electron impact ion source, with an additional peak at 400 °C indicating the desorption of ammonia. Sharp signals are also observed centered at 170 °C that indicate the release of residual propylene oxide from

the surface of the material. The parent ion (m/z = 58) is observed concurrently to two major fragment ions at m/z = 43, the epoxide moiety, and m/z = 15, the methyl group. Additional signals were seen at 190 °C (m/z = 38) and 550 °C (m/z = 85) and are attributed to the desorption of a small amount of diatomic fluorine and residual carbonaceous species, respectively (Figure 4.2c).

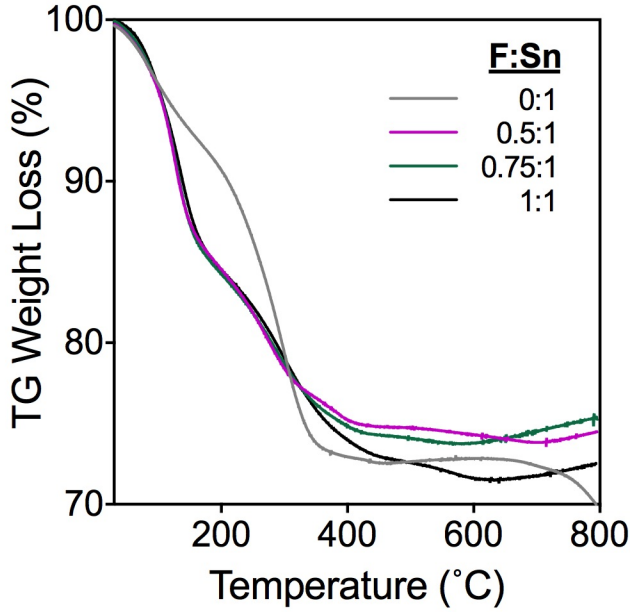

Figure 4.1. Thermogravimetric curves for SnO_2 samples with different amounts of precursor NH_4F.

The unfluorinated sample (Figure 4.2a) exhibits a similar water desorption profile, though the ratio of surface-adsorbed water to pore-bound water and surface hydroxyl groups is reversed. In stark contrast to the fluorinated sample, however, no signals indicating PPO desorption were observed. The only carbon-containing species detected were CO and CO_2. Since the only oxygen source is the tin oxide, the observation of oxidized carbon suggests that the PPO is decomposing on the surface of the unfluorinated material while removing oxygen from the structure, inducing cracking and shrinkage of the structure.

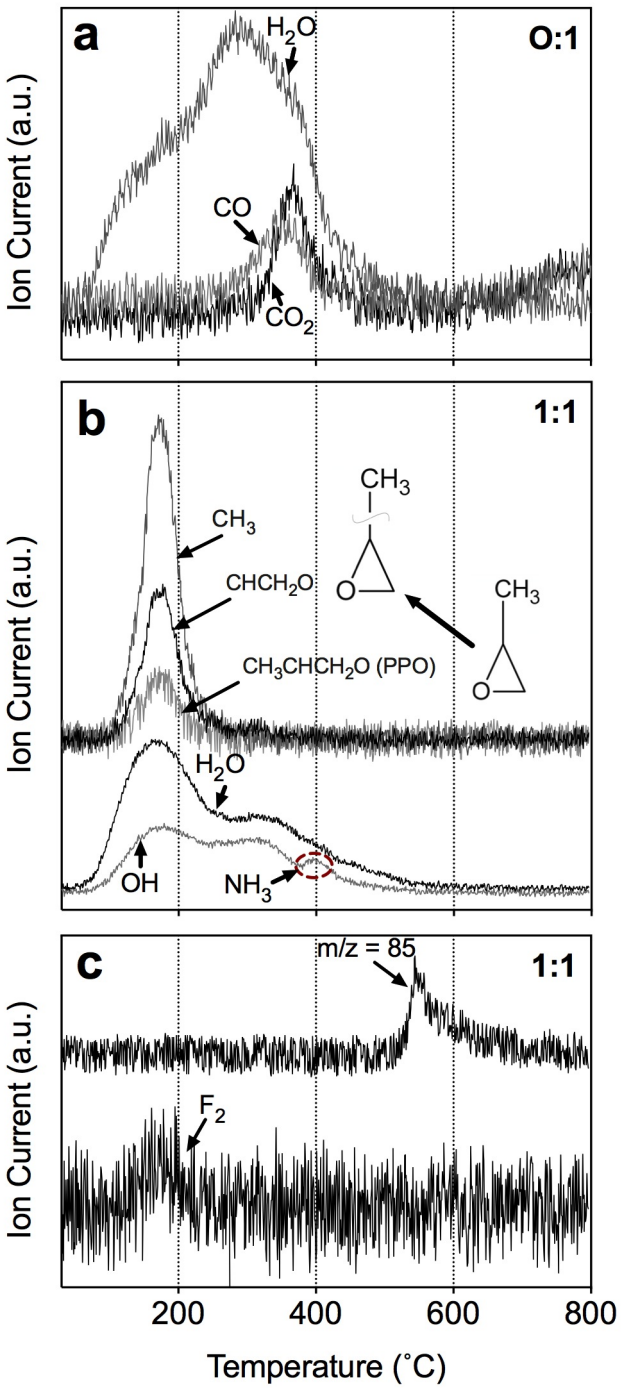

Figure 4.2. Temperature programmed desorption curves for a SnO_2 material (a) and the fluorinated analog (b)

These experiments indicate that the presence of fluorine is critical to the release of PPO during heat treatment and may explain why the fluorinated aerogels are more thermally stable.

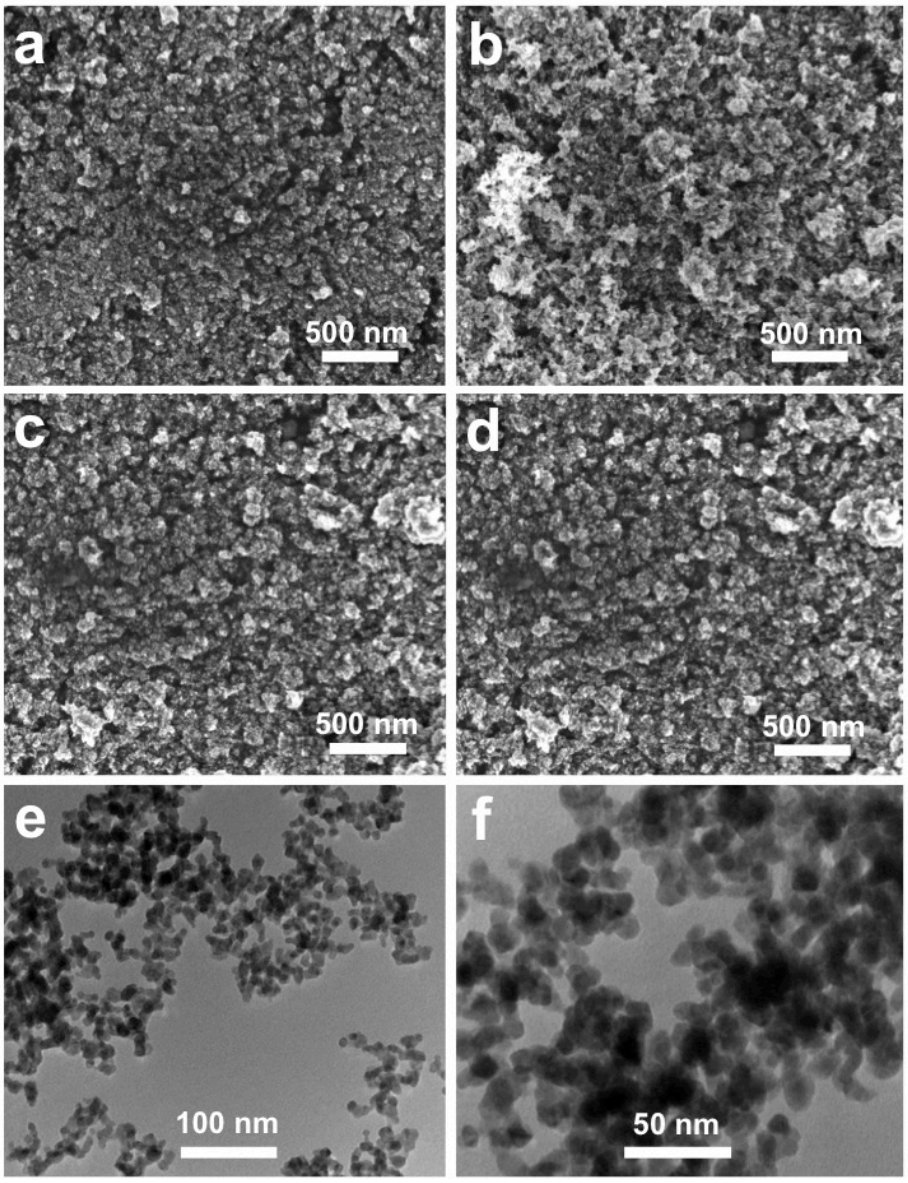

Figure 4.3. Scanning electron micrographs of SnO_2 aerogels with (a) 0:1 (b) 0.5:1 (c) 0.75:1 and (d) 1:1 of F:Sn precursor ratio. TEM images of 1:1 F:Sn materials at different magnification (e and f).

4.2.3 Aerogel morphology

SEM images of the SnO_2 aerogels with precursor fluorine at 0:1, 0.5:1, 0.75 and 1:1 F:Sn (Figure 4.3a, b, c and d, respectively) are shown. The aerogels exhibit an open pore structure typical of these mesoporous materials. Qualitatively at this magnification, fluorine does not seem to have an effect on the morphology of the powderized aerogels. Because the SEM images did not present a clear view of the materials' morphology, low magnification HRTEM (Figure 4.3 e and f) was performed examine the porous structure of 1:1 F:Sn aerogel. The image reveals the branch-like structure composed of spherical interconnected particles. Qualitatively, the aerogel exhibits well-defined mesopores in the range of 10-70 nm similar to an earlier report.[80] Our TEM images are different from those reported on unfluorinated SnO_2 aerogels by the epoxy-assisted method, in that, qualitatively, their materials did not exhibit well-defined mesoporosity.

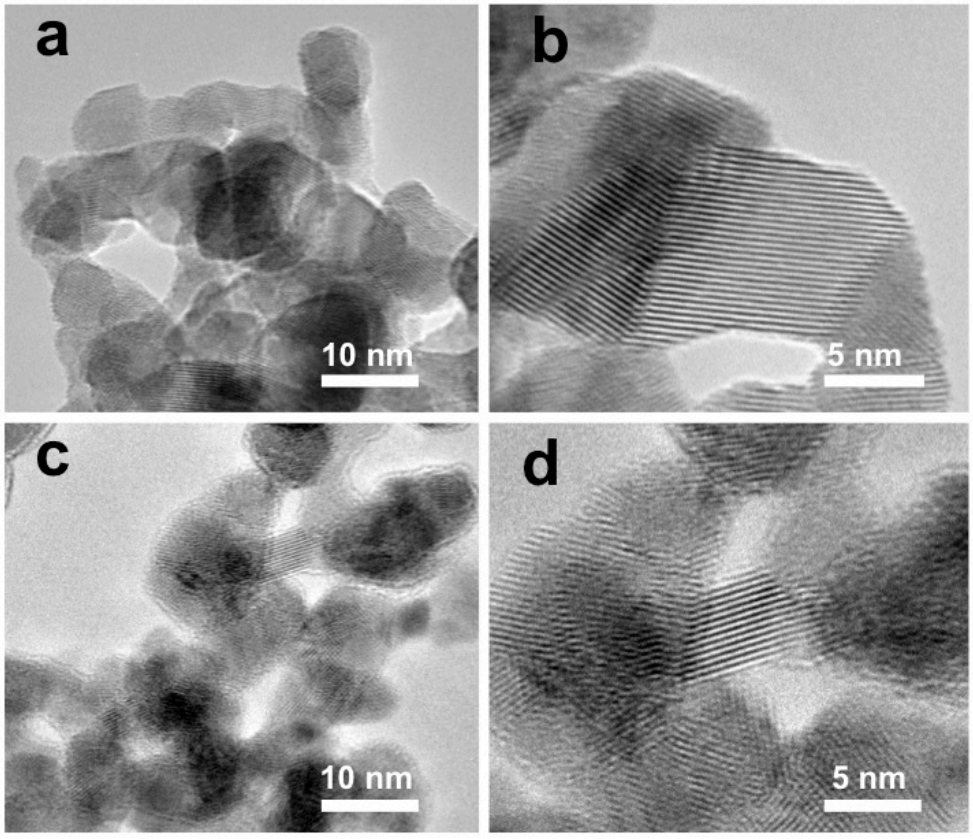

Figure 4.4. High resolution transmission electron micrographs of SnO_2 aerogel structures showing a close-up of the particles of 0:1 (a,b) and 1:1 (c,d) at different magnifications.

HRTEM images at different magnification are presented for 0:1 and 1:1 precursor F:Sn (Figure 4.4a-b and c-d, respectively) aerogel samples and aims at understanding the crystallinity, size, shape and interconnectivity of the particles. It appears that most particles are spherical with the exception of few elongated ones that seem to be sintered into other particles such as those seen in Figure 4.4a and c. These images reveal nanoparticles in the range of 3-10 nm, with the fluorinated samples (1:1 F:Sn), exhibiting slightly smaller particles. It is important to note that this presumable decrease in particle size is not based on calculations but rather on observation. XRD analysis will help in evaluating this further. Figure 4.4b and c shows the highly crystalline nature of the particles with well-defined lattice fringes. The particles appear to be interconnected forming the network typical of other metal oxide aerogel materials.[84]

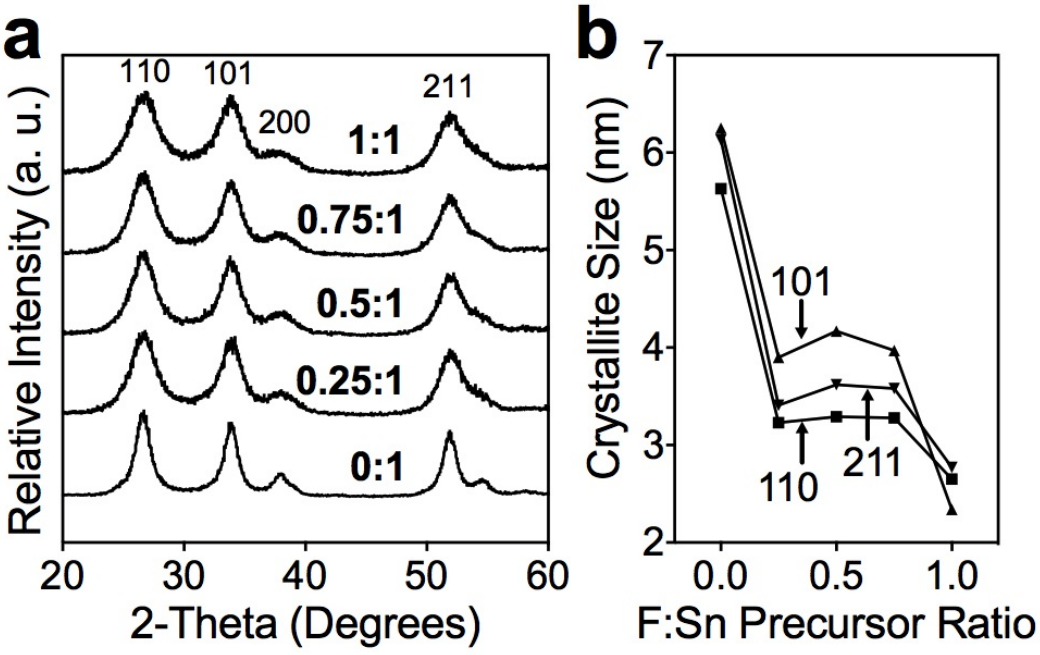

Figure 4.5. Powder XRD patterns for SnO_2 aerogels as a function of F (a) and crystallite size calculated with the Scherrer equation from the three main peaks (b). Samples were prepared with precursor F:Sn ranging from 0:1 to 1:1.

Table 4.2. Nitrogen physisorption information as a function of precursor fluorine (F:Sn) content in SnO_2 materials before and after calcination at 450˚C for 30 minutes.

F:Sn	BET surface area (m^2g^{-1})		BJH pore volume (cm^3g^{-1})		BJH mean pore radius (Å)	
	Uncalcined	450˚C	Uncalcined	450˚C	Uncalcined	450˚C
0:1						
0.25:1	451	98	1.62	1.24	118	282
0.5:1	357	149	1.66	1.10	155	208
0.75:1	257	135	1.07	1.06	144	255
1:1	183	101	0.77	0.89	140	232

4.2.4 Crystal structure

Powder XRD patterns are presented for samples of SnO_2 unfluorinated and fluorinated (Figure 4.5a). The analysis of the patterns revealed that all samples have the tetragonal rutile phase of SnO_2 (JCPDS card no. 041-1445), which belongs to the space group P42/mnm (no. 136). No other crystal phases were detected for any of the materials. Major peaks for the (110), (101), (200) and (211) orientations were detected with high intensities, although a preferred orientation was found to be along the 110. The peaks became noticeably broader with the addition of F, regardless of concentration. The crystallite size was calculated with the Scherrer equation (Figure 4.5b) from the well-defined peaks of (110), (101) and (211) with fairly invariable results from peak to peak. It was found that there is a significant decrease in crystallite size with even small amounts of F added with the smallest crystallite size found when F is introduced at a precursor

ratio of 1:1 F:Sn. These numbers are within the qualitative estimate in the TEM images (Figure 4.4), which showed particle sizes in the range of 3-10 nm.

4.2.5 Nitrogen Physisorption Analysis

Nitrogen physisorption data is presented in table 4.2 and Figure 4.6 for SnO_2 aerogel materials with varying F content. The measurements were performed on uncalcined and calcined (450˚C) aerogels to understand the effect of temperature as well as F content on aerogel morphology. The isotherms for both uncalcined and calcined samples were type IV with a H1 hysteresis typical of mesoporous materials with spherical particles (Figure 4.6a, b). The pore size distribution confirmed the materials are in the mesoporous range (Figure 4.6c, d) as reported for other SnO_2 structures.[83] All materials exhibited high surface area in the range of other calcined metal oxide aerogels.[81,117] The addition of F consistently decreased the surface area and pore volume of the uncalcined aerogels as seen in Figure 4.6a and c, respectively. The former can be explained by the pore size distribution (Figure 4.6c), where an increase in the F has a more pronounced effect in lowering pore volume in the smaller pore size range (<8 nm) than in the region with larger pores. This suggests that either (1) fluorinated particles are interconnected more closely than the unfluorinated counterparts or (2) that fluorinated particles are smaller than those with no fluorine. Both hypotheses would yield increase in pore volume. According with the TPD data, it is possible that some carbonate species are attached to the unfluorinated samples as evidenced from CO_2 volatilization (Figure 4.2a) and this may cause the uncalcined samples to be more spread apart.

In contrast, the addition of F yielded no significant change in BET surface area for aerogel samples calcined at 450˚C, at around 100-150 m^2g^{-1} (Figure 4.6b) This is not surprising as TEM data showed no significant change in the particle size, therefore, these calcined materials were expected to render similar surface area. The decrease is

surface area from uncalcined to calcined samples is consistent with other studies where an increase in calcining temperature yields decrease surface area as particles become larger and sinter together, effectively reducing the surface area.[118]

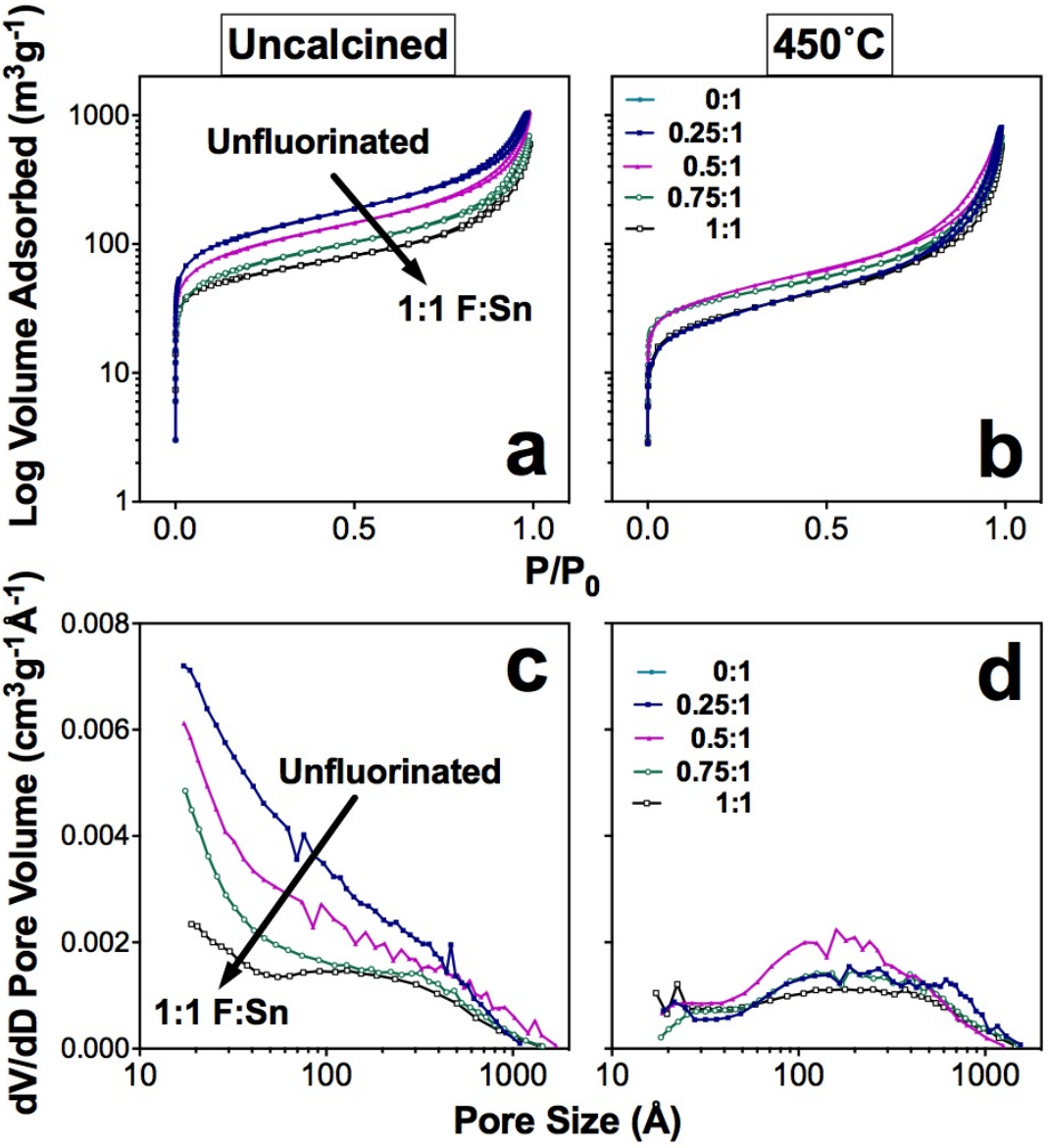

Figure 4.6. Nitrogen physisorption isotherms and pore distribution analysis for SnO_2 aerogels as a function of Fluorine uncalcined (a,c) and calcined at 450˚C (b,d).

For calcined materials the pore distribution changes dramatically. The smaller size pores seen in uncalcined samples almost completely disappear with pores in the

mesoporous region becoming dominant for calcined samples (Figure 4.6c and d, respectively). This can be explained by particles sintering which closes off smaller pores inducing necking. Additionally, pore volume of these calcined aerogels sees little change with the increase of precursor F content throughout the mesoporous region. These results were unexpected, because the increase in F content in the aerogels exhibited a decrease in monolith shrinkage, and therefore it was expected that these materials render higher pore volumes than the less fluorinated counterparts. It is important to note that materials with less F content show a large decrease in pore volume after calcination, whereas those with higher F content (specially 1:1 F:Sn) retained their uncalcined pore volume (Table 4.2). Pore radius remained fairly constant with the increase of F for uncalcined samples, with an average of 11-15 nm. Calcination of the aerogels increased the average size of the pores to 20-28 nm as particles sinter and necking is induced as seen in the TEM images (Figure 4.3e and f).

4.3 Conclusions

The effect of NH_4F on the morphology of SnO_2 aerogels synthesized by a facile sol-gel process has been thoroughly studied. Addition of F significantly decreased the gelation time of the Sn solution. Apparent shrinkage after SCD decreased with the addition F with unfluorinated samples exhibiting 39% shrinkage while fluorinated samples (at 1:1 precursor F:Sn) only 7%. All samples showed large shrinkage after calcination, but fluorinated samples (1:1) showed the smallest shrinkage. TGA and TPD experiments indicated no PPO release for unfluorinated samples but instead CO2 was detected, suggesting the reaction of PPO with the oxygen in SnO_2. In contrast, fluorinated samples (1:1) exhibited no CO_2 signal, whereas PPO was readily detected. This suggests that F prevents the bonding with a PPO moiety, thus preventing additional shrinkage presumably caused by the removal of oxygen atoms in SnO_2. All aerogel materials

exhibited a cassiterite (rutile) crystal structure with well-defined lattice fringes as observed by TEM and XRD. Crystallite size decreased with the addition of precursor fluorine. Uncalcined materials exhibited a decrease in surface area with increasing F concentration, but this trend disappeared after calcination at 450˚C with surface area for all materials remaining around 100-150 m^2g^{-1}

5 Transparent Conducting Aerogels of Antimony-Doped Tin Oxide

In this chapter the synthesis and material characterization of antimony-doped tin oxide aerogels will be studied. The improvement in electronic properties with Sb doping is essential in having a porous TCO. This chapter will be stepping stone to Chapter 6, where the aerogel materials will be used as conductive scaffold in solar cell preparation.

5.1 Introduction

Tin oxide materials are commonly doped with fluorine (FTO) or antimony (ATO) or dissolved in indium oxide (ITO) to make transparent conducting oxides (TCO). The high cost of indium is disadvantageous for ITO and has led many researchers to shift attention to low-cost alternatives such as FTO and ATO. In the former, fluorine atoms replace oxygen atoms in the lattice, and in the latter, antimony replaces tin, in either case resulting in a highly n-doped semiconductor. Under optimized conditions, TCO materials can exhibit high Hall mobility, low resistivity and high transmittance in the visible range, even from low-temperature synthesis.[46] These properties make TCOs essential in a wide variety of applications such in solar energy conversion,[40,41,46] water splitting,[43] optoelectronic devices[44] and gas sensors.[45] These have traditionally been processed as compact films[52-54,56] exhibiting high conductivities. While achieving high doping levels in nanoparticles by wet-chemical synthesis is challenging,[119] nanoparticles of FTO[57] and ATO[37,49] have been realized from solution. Mesoporous films of such nanoparticles have been made by block-copolymer templating[70,120,121] or by simple doctor-blading.[49] Nanoparticle systems are significantly less conductive than their compact film counterparts due to grain boundary scattering, which limits electron mobilities.[54] However, the morphologies such sols can produce are desirable for applications that require a high surface area for contact between the TCO[122] and another

phase, such as core-shell architectures in dye-sensitized solar cell[41] and water splitting devices.[123]

Aerogels are 3D monolithic structures composed of networked nanoparticles and exhibit high surface area, high porosity, and good particle interconnectivity.[74] These are processed as sol–gels where a catalyst causes the gelation of the sol, commonly at low temperatures. Acid- and base-catalyzed formations of silica aerogels have long been widely studied.[75,78] More recently, Gash and coworkers developed an epoxide-initiated sol–gel process used to synthesize iron oxide aerogels.[80] The hydrated metal is deprotonated by the epoxide, which links it with other hydrated metals via olation and oxolation to form metal oxide particles. These in turn crosslink to form a 3D array of particles, i.e., a gel. This sol–gel process has been used to make other materials such as ZnO[81] and SnO_2 aerogels.[83] Its main advantage is that the wet-gels can be prepared from many metal salts that are low-cost and easy to handle.

Silica aerogels have been used in dye-sensitized solar cells as mesoporous templates for TiO[98] and ZnO[97] coatings. Given the insulating nature of silica, electrons are transported by the thin semiconducting shells. For such a system, it is desirable to synthesize a transparent conducting material with high surface area and mesoporosity as the scaffold for electron collection. TCO aerogels have a combination of these properties

In this chapter, we synthesized a TCO aerogel by supercritically drying gels of ATO. We use the epoxide-assisted method to form gels with varying concentrations of Sb. We used scanning electron microscopy, X-ray photoelectron spectroscopy and electrical conductivity measurements (among others) to study the effects of Sb doping on the morphological, optical and electronic properties of SnO_2 aerogels.

5.2 Results and Discussion

5.2.1 Synthesis

Several solvents were investigated in the sol–gel process to produce monolithic gels. Table 5.1 presents the solvents, the ratio of the F to Sn in the precursor solution, whether it dissolves and gels, and the time required to gel (t_{gel}). The tin salt dissolved readily in all solvents when no fluorine was present, and precipitates were formed as NH_4F was added to the solution which redissolved in solution after 2 hours of stirring in a 60˚C water bath. Up to a F:Sn atom ratio of 1.25:1, ethanol was able to effectively dissolve the salts, but white precipitates formed above that ratio. Gel formation was observed for all 0:1 samples, regardless of the solvent. These yielded translucent gels with an initial firm bounce, but shrank in the capped vial after 30 minutes of PPO addition. To avoid the evaporation of the solvent and prevent the aforementioned shrinkage, the gel's original solvent was added to the vial after 20 minutes of PPO addition and it was subsequently capped.

Fluoride is commonly used as a catalytic agent in silica sol-gel processing, and affects its gel times[115] and physical properties.[79] The addition of F has also been found to decrease the shrinkage in silica gels and aerogels.[78] We found that gels with no fluorine content tended to shrink during the aging and SCD processes, and show severe shrinkage after calcination at 450˚C. In contrast, gels with higher fluorine content experienced little gel shrinkage after PPO addition during aging, SCD and calcination. Furthermore, fluorine-containing gels proved vital to achieving aerogel monolithic thin films without cracks or delamination (Figure 5.1, bottom). However, resistivity was not significantly changed by the use of NH_4F in the reaction. For aerogels made with NH_4F, XPS analysis revealed only a small F 1s peak in an uncalcined sample, and no F in a sample calcined at 450°C. We conclude that F incorporation into the tin oxide was

minimal. Ammonium fluoride therefore had a significant structural effect on the SnO_2 aerogel despite a lack of electronic effect. The effects of fluorine on the gel structure will be the subject of a future study. The basic approach selected for the aerogels described in the remainder of this paper was ethanol-based synthesis of SnO_2 aerogels with NH_4F included at a F:Sn ratio of 1:1 for the favorable resulting structure, while antimony was added as a dopant to render the aerogel electrically conducting.

Table 5.1. Summary of solvent and NH_4F effect on solutions and gelation of SnO_2 (0.6M $SnCl_4$, H_2O/Sn =13, PPO/Sn = 11).

Solvent	Precursor F:Sn	Clear Solution	Gel Formation	t_{gel} [min]
Methanol	0:1	Yes	Yes	50
	0.5:1	Yes	No	-
	1:1	No	No	-
Ethanol	0:1	Yes	Yes	12
	0.5:1	Yes	Yes	7
	1:1	Yes	Yes	2.5
Propanol	0:1	Yes	Yes	13
	0.5:1	Yes	Yes	2.5
	1:1	No	No	-
Butanol	0:1	Yes	Yes	13
	0.5:1	No	No	-
	1:1	No	No	-
Acetonitrile	0:1	Yes	Yes	13
	0.5:1	No	No	-
	1:1	No	No	-
Dimethyl-formamide (DMF)	0:1	Yes	Yes	20
	0.5:1	No	No	-
	1:1	No	No	-

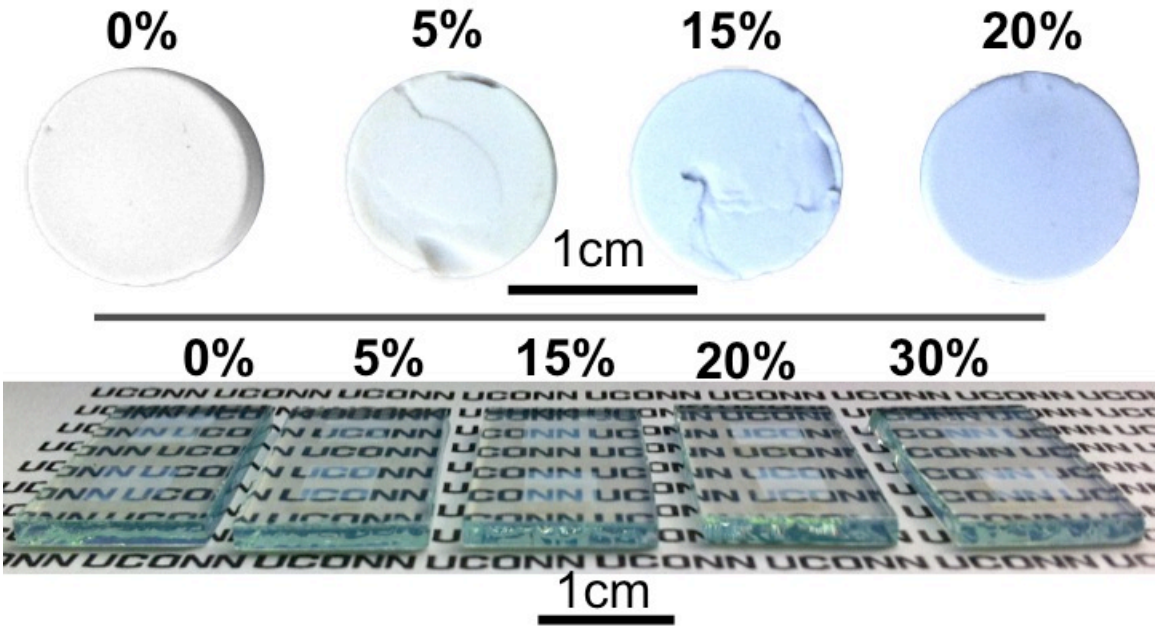

Figure 5.1. SnO_2 cylindrical aerogel monolith (top) and thin films on glass (bottom) photographs at different Sb/Sn precursor mol ratios after calcination at 450˚C for 30 minutes.

Bulk aerogels made as just described exhibited no visible shrinkage during SCD, although minor shrinkage was noticed after calcination at 450˚C for 30 minutes. The addition of Sb had no visible change in the bulk aerogel appearance except for a blue-grey color that appeared following calcination in materials doped with more than 5% Sb (Figure 5.1, top). Calcination at 800˚C induced further shrinkage of the aerogel monoliths and the blue color became more intense. This color has been attributed to the absorbance of electrons in the conduction band of the semiconductor.[59,63,124] Alternatively, it has been suggested that Sb^{5+} and Sb^{3+} create impurity levels at or below the conduction band of the semiconductor, effectively reducing its bandgap which in turn gives out the blue coloration observed here.[62] The color change has been consistently observed in different synthetic processes using antimony as a dopant[37,48,63] and with the introduction of oxygen vacancies.[49] The aerogels were scattering in the bulk form but

they are transparent when made as thin films, as is demonstrated in the photograph of thin films on FTO glass with different Sb content (Figure 5.1, bottom). The fabrication and characterization of the thin films will be detailed in a separate paper.

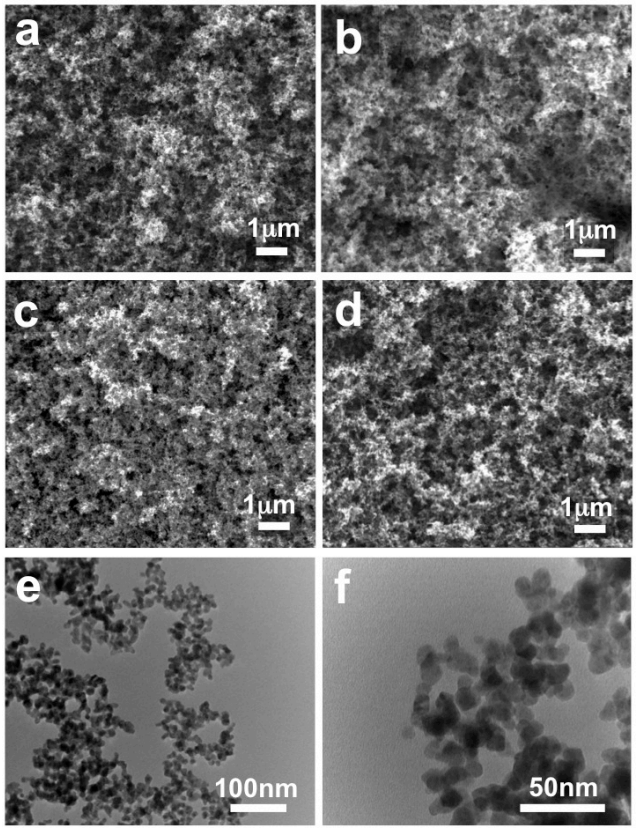

Figure 5.2. SEM images of SnO_2 aerogels undoped (a) and doped with 5 (b), 10 (c), and 15 (d) % Sb as the precursor Sb/Sn mol ratio. TEM of undoped SnO_2 at different magnifications (e and f).

5.2.2 Structure

SEM images of the undoped (Figure 5.2a) and 5, 10 and 15% Sb (Figure 5.2b, c and d, respectively) doped aerogels revealed the open pore structure and good particle interconnectivity characteristic of aerogel materials. At this magnification, all samples are qualitatively of the same morphology regardless of the Sb doping level. However, some quantitative differences were revealed by more detailed analyses. The results of nitrogen

adsorption/desorption measurements are shown in Table 5.2.[125] The isotherms (Figure 5.3, top) were type IV with an H1 hysteresis, and the pore size distribution (Figure 5.3, bottom) showed that the materials are in the mesoporous range as reported for other SnO_2 structures[83] and in agreement with the TEM images (Figure 5.2e and f).

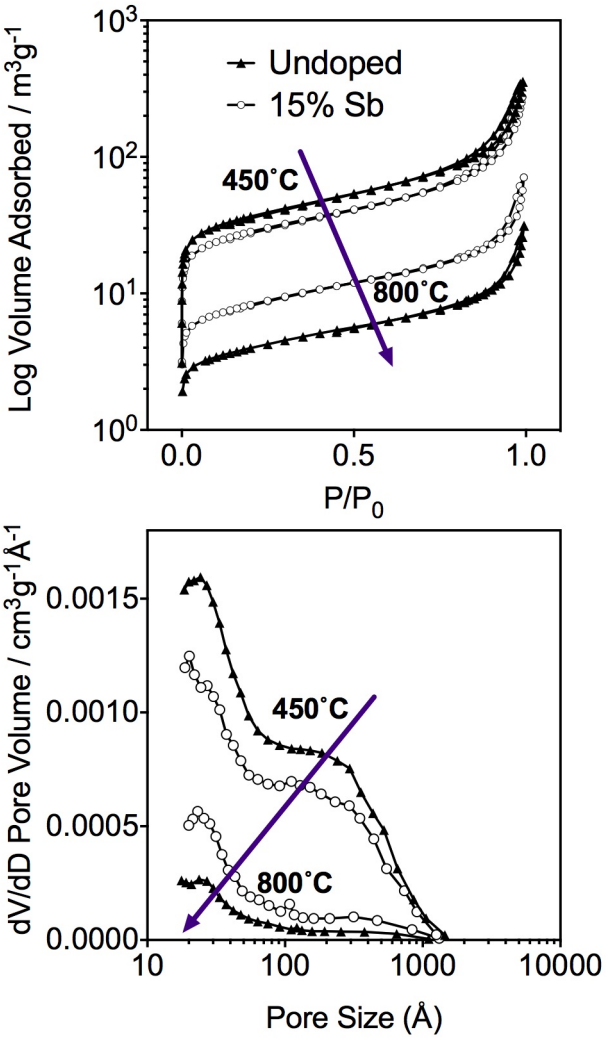

Figure 5.3. Nitrogen adsorption/desorption isotherms for undoped and 15% Sb doped SnO_2 aerogels calcined at 450˚C and 800˚C (top) and their respective pore size distribution (bottom). Lines were added to aid the eye.

ATO aerogels calcined at 450˚C exhibited high surface area (~100-200 m^2/g) in the range of other calcined metal oxide aerogels.[81,117] However, the addition of the Sb

precursor up to 15% consistently decreased the surface area and pore volume of the aerogels. No significant change in BET surface area is seen from 15 to 30% Sb. Similarly, the pore volume saw no significant change from 15 to 30% Sb, although it shows an increase at 20%. The average pore radius shows no clear overall trend with dopant concentration. The ATO aerogels prepared in this study show higher surface area and pore volume than those found by Davis et al. with ITO aerogels prepared by an epoxide-initiated process.[84] Calcined at 600˚C, these materials showed a low surface area (39 m^2g^{-1}) and pore volume (0.16 cm^3g^{-1}).

Aerogels calcined at 800˚C for 6 hours were found to suffer apparent monolith shrinkage and this was shown quantitatively in the nitrogen physisorption analysis (Figure 5.3). Pore volume decreased (Table 5.2) from 0.93 and 0.42 to 0.111 and 0.049 cm^3g^{-1} for undoped and 15% Sb doped aerogels, respectively. The pore size distribution shows a pronounced decrease in the mesopore region with higher pore volume of smaller pores. The BET surface area decreased from 206 and 103 m^2g^{-1} to 14.2 and 29.8 m^2g^{-2} for 0 and 15% Sb, respectively, which is indicative of particle growth and sintering.[118]

XRD patterns of aerogel powders were obtained for undoped and doped samples (Figure 5.3, left). All samples matched the cassiterite pattern (JCPDS No. 41-1445) with 110, 101, 200 and 211 lattice planes. No peaks representing other phases were observed, suggesting that the antimony atoms were accommodated in the SnO_2 lattice. Undoped materials calcined at different temperatures were analyzed and found to be amorphous below 400˚C, with clear peaks emerging at and above 450˚C (data not shown). The introduction of Sb caused a broadening of the peaks suggesting a decrease in the particle size. The aerogels calcined at 800˚C exhibited much sharper peaks with evident improvement in crystallinity (Figure 5.3, left). At 450˚C the 211 peak overlaps

with a neighboring peak, whereas this phenomenon disappears at 800˚C. The Scherrer equation was used on the three main peaks of aerogels calcined at 450˚C and 800˚C to quantify the effect of doping and temperature on crystallite size. For samples calcined at the lower temperature, the 110 and 211 peaks show a similar trend: the crystallite size decreased from about 3.6 nm for undoped samples to 2.9 nm for 30% Sb (Figure 5.3, right). A negative effect of doping on crystallite size is consistent with other reports for doped metal oxide nanoparticles with similar synthetic processes.[63,126-129] Goebbert et al., for example, reported a similar trend for ATO nanoparticles prepared at 150˚C, where doping reduced the crystallite size from 7 nm to 3 nm.[55]

Table 5.2. Compositional analysis and physical and electronic properties of doped and undoped SnO_2 aerogels.

Calcining Temperature [˚C]	Precursor Sb/Sn [%]	XPS Sb/ Sn [%]	BET surface area [m^2g^{-1}]	BJH pore volume [cm^3g^{-1}]	BJH mean pore radius [Å]
450	0	-	206	0.93	172.2
	5	3.1	169	0.68	142.6
	10	5.6	143	0.55	139.4
	15	7.6	103	0.42	157.3
	20	12.4	97	0.65	142.7
	30	13.2	98	0.43	193.6
800	0	-	14	0.05	130.1
	15	16.2	30	0.11	146.7

Calcined our aerogels at 800˚C dramatically increased the crystallite size. This was especially true for undoped samples, which yielded crystallites about 30 nm in size. Interestingly, the effect was not as marked for samples doped with 15% Sb, which

produced crystallites of about 9 nm. These results are confirmed by the decrease in surface area of samples calcined at 800˚C.

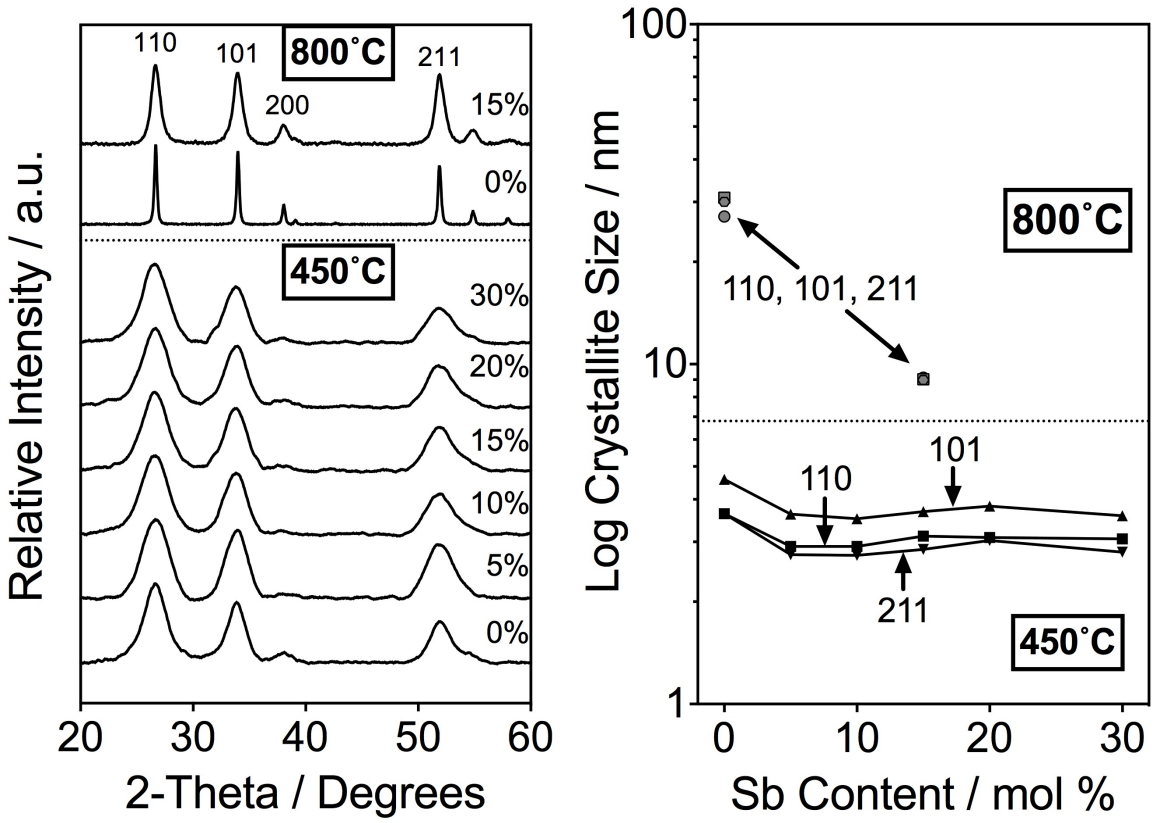

Figure 5.4. The effect of calcination temperature and Sb doping on crystal structure with XRD pattern of undoped and doped SnO_2 aerogels (left) and crystallite size calculated with the Scherrer equation from the three main peaks (right), listed by precursor %Sb.

5.2.3 Sb analysis

X-ray photoelectron spectroscopy (XPS) was conducted for of aerogel samples with 0, 5, 10, 15, 20 and 30 %Sb calcined at 450˚C (Figure 5.4, left) and 0, 15 and 30 %Sb calcined at 800˚C (right) to study the elemental composition of the aerogel materials and to analyze the oxidation state of Sn and Sb. Survey scans between binding energies of

470 and 550 eV were made for all samples, and high-resolution spectra (1000 scans) from 525 to 545 eV for the doped samples. The tin peaks corresponding to $3d_{3/2}$ and $3d_{5/2}$ electrons were found at binding energies of 495 and 488 eV, respectively, confirming the presence of Sn(IV) in the material regardless of calcination temperature.[130] No chlorine, nitrogen or fluorine was detected suggesting that these by-products had been either washed out in the gel aging/washing process or volatilized during the calcination step.

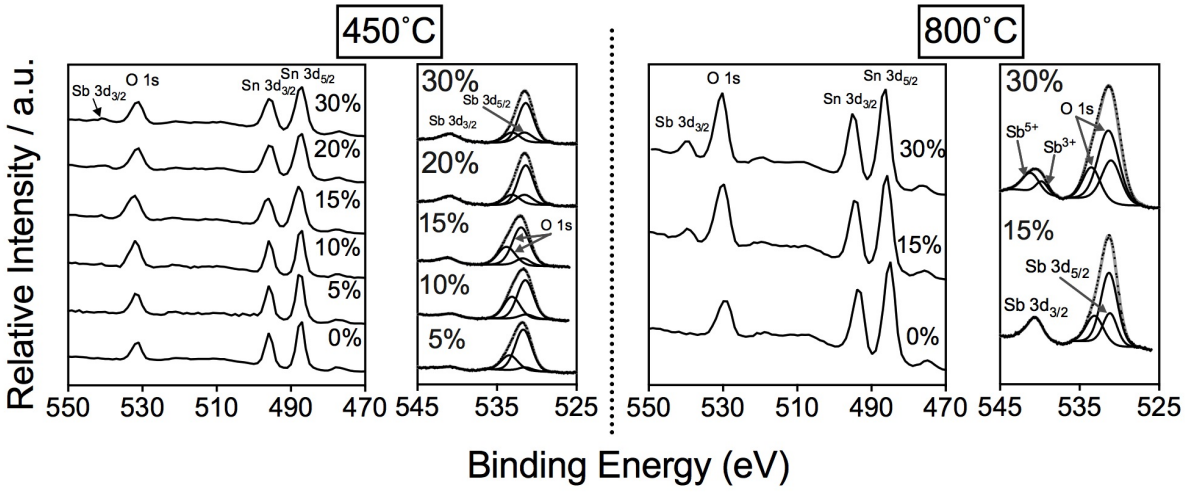

Figure 5.5. XPS spectra of undoped and Sb doped SnO_2 and the respective high-resolution spectra of the Sb 3d and O 1s peaks with fitted lines using CasaXPS software at 450˚C (left) and 800˚C (right). Each trace is labeled with the precursor %Sb

The high-resolution scans allowed the quantification of Sb relative to Sn, and the resulting values are included in Table 5.2. The $3d_{3/2}$ peak of Sb at ~541eV was used since its $3d_{5/2}$ peak interferes with that of O 1s at a binding energy of ~531eV. For aerogels calcined at 450 °C, the measurement confirmed the presence of the dopant and the Sb:Sn ratio was consistently slightly more than half of its value in the precursor solution. Such incomplete incorporation of dopants is common in sol–gel processes.[131] Surprisingly, the 800˚C samples had higher Sb:Sn ratios, close to the precursor values.

Since XPS is a surface-sensitive technique, we attribute this observation to the migration of antimony atoms towards the surface as has been suggested by other reports.[132,133]

It has been widely reported that the conductivity of ATO materials depends on an excess of Sb(V), which introduces donor states (electrons), with respect to Sb(III), which provides acceptor states (holes).[37,38] The resistivity of the material is therefore correlated to the concentration difference between the two oxidation states. While some reports[38,131] have found some conversion of Sb(V) to Sb(III) at high doping levels, our XPS results showed that only Sb(V) was present, with the exception of a small amount of Sb(III) found in 30% Sb samples calcined at 800˚C. The $3d_{3/2}$ Sb peaks of all but one sample are found at ~540.5 eV (high resolution spectra in Figure 5.4), which is attributed to Sb(V).[134,135] The $3d_{3/2}$ Sb peak of the 30% Sb sample calcined at 800˚C was found at 539.4 eV (high resolution spectra in Figure 5.4, right), corresponding with values for Sb(III) found elsewhere.[134,136] An X-ray absorption finite structure measurements (XANES) study[63] found that Sb(III) is more prevalent for materials using Sb(III) in the precursor, with lower Sb(III) found when using Sb(V) in the precursor solution. This trend disappears and Sb(III) detected increases when the material is calcined at high temperatures, similar to our findings. This results support the supposition that the consistent decrease in resistivity is due to the additional electrons from Sb(V) in the conduction band. The deconvoluted O 1s curve exhibits two fitted peaks at ~533 and 531eV which suggests there are two oxygen types. The O 1s peak at ~531eV corresponds to the lattice oxygen atoms in SnO_2,[137,138] and the one at ~533eV to water and hydroxyl groups not part of the SnO_2 crystal structure.[139-142]

5.2.4 Electrical properties

Electronic properties of bulk aerogels calcined at 450˚C for 30 min in air without any further treatment were characterized. To the best of our knowledge, this is the first time

conductivity measurements are made on uncompressed, nanoparticulate materials without a modification to the bulk structure, such as those made via the use of block copolymer methods to cast as films[70] or by pelletization of powders.[48,61,62,76,84,143] Because of the networked structure of interconnected particles inherent to aerogel structures, we were able to measure current-voltage characteristics, which is not feasible for powders that have not been pelletized. Figure 5.5 (top) summarizes the resistivity of ATO monolithic aerogel disks at different doping concentrations calcined at 450˚C. We found that the addition of 15% precursor Sb (7.6% by XPS) gave an optimum resistivity that was more than 3 orders of magnitude lower than the undoped analog. These undoped samples exhibited a high resistivity of $\rho = 4 \times 10^6$ Ω-cm, which then dropped consistently to reach a minimum of $\rho = 1.1 \times 10^3$ Ω-cm at 15% Sb and then increased slightly up to 20 and 30% precursor Sb. Comparable resistivities on the order of 10^3 Ω-cm[144] and 10^2 Ω-cm[84] have been observed for pelletized ITO materials calcined at 400˚C and 600˚C, respectively.

Measurements were performed for aerogel monoliths containing 0 and 15% Sb and calcined at 800˚C for 6 hrs. The results show a further 2-order of magnitude decrease in resistivity to ~30 □-cm for the 15% Sb samples, and 1 order of magnitude increase to ~2×10^8 □-cm for the undoped samples (Figure 5.5, top). These results yield a 7 order of magnitude decrease in resistivity. The reduction of the resistivity of the 15% Sb sample by high-temperature calcination can be explained by the increase in crystallite size from ~3 to ~9 nm and particle sintering, and the burning off of some carbon species left over from the synthesis process. These results are consistent with those reported by Nutz et al. with pelletized ATO nanoparticle (~7 nm) materials calcined at 900˚C that exhibited resistivities of ~10 □-cm. Calcination of the undoped SnO_2 aerogel at 800 °C greatly

increases its crystallite size to ~30 nm; it is unclear why its resistivity is not reduced as is that of the 15% Sb samples.

In order to compare the resistivities of these materials with those in the literature for pelletized materials, we measured resistivities of pelletized undoped and 15% doped SnO_2 aerogels that had been sintered at 800 °C for 6 h. Pelletization reduced the measured resistivities by about an order of magnitude compared to bulk aerogel samples, with the pelletized 15 %Sb-doped sample reaching a resistivity as low as 3 Ω-cm. This is not surprising since the reduction of pore space and the increase of contact area between particles should decrease resistivity.

Compact ATO films have been reported to possess several orders of magnitude lower resistivity than these porous materials.[145] This can be explained by the nature of nanoparticulate grain boundary electron scattering,[54] which decreases electron mobility in the nanoparticle array. For crystallite sizes in the range of 3-4 nm, the number of grain boundaries is very large, thus our resistivity numbers may be improved with higher calcination temperatures which in turn increase the crystallite size. Calcining the aerogel samples at 450˚C guaranteed both decreased resistivity and little shrinkage of the aerogel structure, both important components for making conducting thin films of aerogel without causing cracking or delamination.

5.2.5 Optical properties

The optical absorbance for aerogel samples calcined at 450˚C was characterized by diffuse reflectance (Figure 5.5, bottom). It was found that undoped aerogels have negligible Kubelka-Munk absorbance in the visible range. With increasing Sb content, the absorbance increased but overall remained low. The doped aerogels absorbed more in the 700 to 800 nm range, which explains the blue coloration of materials in Figure 5.1 (top). This trend is similar to those seen in reports of doped SnO_2 materials.[61]

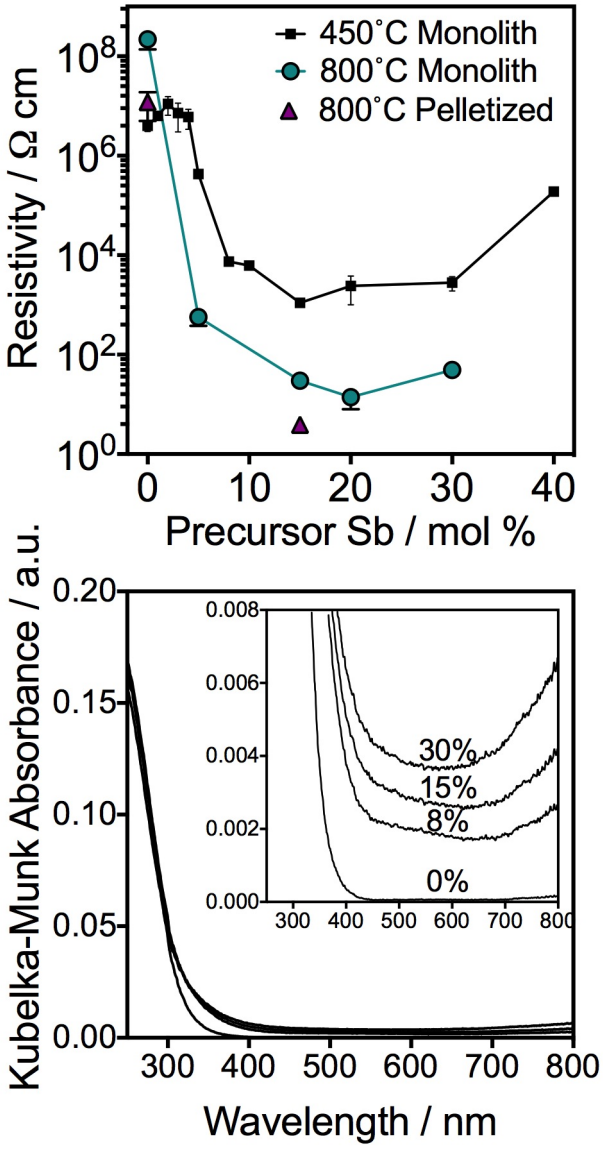

Figure 5.6. Resistivity plot of monolithic aerogel disks and pellets as a function of Sb precursor concentration and temperature (top) and Kubelka-Munk transform of UV-vis diffuse reflectance of doped and undoped SnO_2 calcined at 450˚C with an expanded view of visible region in the inset (bottom)

5.3 Conclusions

The first antimony doped tin oxide aerogel has been synthesized and characterized based on facile epoxide-assisted synthetic processing. In our sol–gel procedure, the addition of NH_4F to the precursor solution did not result in significant incorporation of F or reduction of resistivity, but it significantly reduced aerogel shrinkage during calcination. The use of $SbCl_5$ together with NH_4F resulted in Sb incorporation and a 3.5-order-of-magnitude reduction in resistivity to $1.1x10^3$ Ω-cm for samples calcined at 450˚C at the optimal Sb:Sn precursor ratio of 15%. The Sb-doped materials exhibited low visible light absorbance. Calcining at 800˚C yielded a further 2 orders of magnitude decrease in the monolithic aerogel resistivity to ~30 □-cm, partly due to increased crystallite size. However, a tradeoff exists as materials calcined at this temperature also yield low surface area and pore volume, which are important properties of aerogels. Sb doped materials calcined at 450˚C therefore yield both improved conductivity and morphological traits typical of aerogels. The high surface area and open-pore structure of these materials, along with their high conductivity and low absorbance, make them well suited to optoelectronic applications. Work is ongoing on the preparation and characterization of thin films of these aerogels and their applications in solar cell devices.

6 Antimony-Doped Tin Oxide Aerogels in Dye-Sensitized Solar Cells

The aerogel materials that were synthesized and characterized in chapters 4 and 5 will be used in this chapter as electron collectors in a core-shell DSC setup. Thin film and solar cell characterization will be thoroughly analyzed.

6.1 Introduction

Dye-sensitized solar cells (DSCs) have emerged as low-cost devices for solar energy conversion.[146] A standard DSC photoanode consists of a dye-sensitized titanium dioxide (TiO_2) nanoparticle film on transparent conductive oxide (TCO)-coated glass. A photoexcited dye molecule injects an electron into the conduction band of the nanostructured semiconductor and is regenerated (reduced) by a dissolved redox couple. Electrons diffuse through the semiconductor layer to the collector, in kinetic competition with recombination of the electrons with the redox couple. Although electron transport through the TiO_2 film is slow, DSCs based on iodide/triiodide (I^-/I_3^-) perform well because of the slow electron recombination associated with triiodide, translating into efficient charge collection.[147]

The large overpotential (ca. 0.5 V) required for regeneration of oxidized dyes by iodide[148] has motivated the development of alternative outer-sphere, one-electron redox couples, often centered around iron (i.e., ferrocene/ferrocenium) or cobalt. While cells based on these couples can give excellent performance,[9,21,149] they are constrained by the faster recombination typical of these redox couples[150] to use very thin films and therefore only dyes with very high optical extinction coefficients. To maintain good charge collection efficiency with thicker films, allowing a greater surface area for dye adsorption, requires more rapid transport of electrons from the semiconductor to the collector.

The aerogel structure is attractive for use in DSC photoanodes due to its high surface area, high porosity and particle interconnectivity.[74] Electronically inert silica aerogels have recently been used as scaffolds for TiO_2 and ZnO thin layers deposited by ALD.[97,98,151,152] The films were used as photoanodes and assembled in DSCs yielding relatively high efficiencies. However, electron transport in these photoanodes is confined to the thin ALD semiconductor layer around the scaffold. On the other hand, researchers have made porous films from colloidal TCO nanoparticles, which can then be coated with wide bandgap semiconductors and used as photoanodes.[41,153-155] A TCO aerogel material would allow current collection through the aerogel support, extending the current collector throughout the mesoporous TiO_2 film while preserving the desirable aerogel structure. As a step in that direction, we recently[156] fabricated bulk TCO aerogels of antimony-doped tin oxide (ATO) and demonstrated a three-order-of-magnitude decrease in resistivity in 15% Sb-doped SnO_2 versus undoped SnO_2. Here, we have adapted the synthesis process of these materials to make thin films of ATO aerogels while adjusting the degree of Sb doping to modify its electronic properties by means of doping.

In this chapter, we present monolithic ATO aerogel thin films with varying Sb content prepared via sol-gel synthesis and supercritical drying (SCD). Conformal layers of TiO_2 were deposited by ALD over the sintered aerogel structure and these were sensitized with D149 dye (Figure 6.1). We used SEM imaging and XRD patterns to characterize the films. DSC devices were fabricated and current–voltage characteristics as well as electron transport and recombination timescales were measured and compared for systems with varying Sb content as well as number of ALD cycles. The device performance in I^-/I_3^- and Fc/Fc^+ electrolytes was evaluated. In the latter case, the ATO

aerogel film exhibited improved performance over a TiO_2 nanoparticulate film suggesting superior electron collection in the novel system.

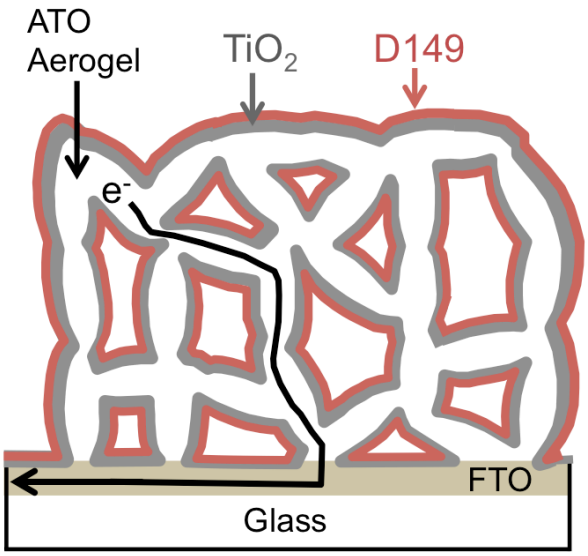

Figure 6.1. Schematic of an ATO aerogel structure with a conformal TiO_2 layer sensitized with D149 dye. The black arrow shows a potential electron pathway through the ATO after photoinjection into the TiO_2 layer.

6.2 Results

6.2.1 Physical Properties of Aerogel Films

Chapter 5 we studied the effect of F and Sb doping on the morphological and resistive characteristics of bulk SnO_2 aerogels, which served as a basis for the present preparation of these materials as thin films. To test the effect of aerogel conductivity in solar cell performance we produced triplicate samples of undoped and 5, 15 and 20% Sb-doped aerogel films. Before supercritical drying (SCD), the aerogel films were transparent with a slight haze, with no noticeable difference between doped and undoped samples.

The addition of NH_4F (at a F:Sn ratio of 1:1) in the precursor solution proved to be crucial in producing monolithic aerogel films that properly adhered to the glass. At a precursor F:Sn ratio lower than 1:1, large cracks formed and parts of the film delaminated. At higher ratios, the solution failed to gel. Therefore, all samples in this study contained 1:1 F:Sn in the precursor solution. Our work with bulk aerogels[156] showed that the fluoride is not significantly incorporated into the SnO_2 and does not affect its resistivity; therefore electronic effects are the result of Sb doping, not F doping. That work also showed that the resistivity of the aerogels (as measured by a 4-point probe) was minimized at 15% precursor Sb doping, with a value of ca. 10^3 Ω cm for uncompressed aerogel monoliths, which is over 3 orders of magnitude lower than the undoped SnO_2 aerogel, while exhibiting low optical absorbance in the visible range.

With thin aerogel films on borosilicate glass, the resistivity measurement was not possible as the four-point probe penetrated through the aerogel to the glass substrate, making poor contact with the aerogel and yielding erratic I–V curves. However, on a doctor-bladed film of TiO_2 nanoparticles, the measurement yielded proper I–V curves and a resistivity of 10^7 □-cm or 4 orders of magnitude more resistive than the bulk 15% Sb doped aerogel. This large decrease in resistivity for the ATO aerogel is seen despite the larger particle size of TiO_2 compared to the ATO aerogel crystallite size (~4nm); the TiO_2 nanoparticulate film should have a smaller number of grain boundaries and therefore less electron scattering.[37,48,54]

Immediately after SCD, the aerogel films were very fragile: minimal pressure exerted on the films would severely damage them. Additionally, it was found that humidity in the environment caused the films to shrink, leading to cracking and delamination. This was avoided by calcination of the aerogels on a preheated hotplate immediately after SCD.

TiO_2 coatings were applied by ALD to the bare aerogels at a rate of ca. 0.04 nm/cycle as determined by ellipsometry and in agreement with similar deposition rates reported by others.[98,123,157-159] Uncoated aerogel films were too fragile for contact measurements such as profilometry, but 50 cycles (~2 nm) of ALD sufficiently fortified the structure to allow such measurements. In addition, ALD-coated aerogels remained intact following wet/dry cycles, e.g. immersion in a dye bath followed by air-drying prior to cell assembly. Uncoated aerogels collapsed upon air-drying; this is why they must be fabricated by careful supercritical drying.

The average thicknesses of samples with varying Sb content and ALD cycles were studied. We found, unsurprisingly, that there is no significant effect of ALD cycles on the film thickness, since the ALD layers are orders of magnitude thinner than the aerogel. However, the increase of Sb content tended to increase the film thickness (Figure 6.2a). This is likely due to the effect of the Sb precursor on the gelation time. During synthesis, it was noticed that higher-Sb-content samples gelled a few seconds earlier than less doped samples, making them slightly more viscous at the time of casting the film and therefore producing thicker films.

The dye-accessible surface area was determined by desorption of the dye from the films followed by spectroscopic quantification. The results, shown in Figure 6.2b, showed some variability as a function of Sb content, with slightly higher loading of the dye D149 for 5 and 15% Sb. Additionally, a general trend of decreased dye loading was observed with increasing numbers of ALD cycles. For undoped samples (0% Sb), for example, the dye loading declined from 39 nmol cm^{-2} after 50 ALD cycles to 32 nmol cm^{-2} after 300 ALD cycles. This results from the closing of small pores by the increasingly thick TiO_2 coatings.

Dark currents of bare aerogels (no ALD) were measured for samples without dye to investigate the effect of Sb doping on the recombination rates with I^-/I_3^- (Figure 6.2c) Recombination rates were noticeably different for the undoped sample, whereas all Sb doped films showed a similar pattern of lower recombination, with 15% Sb exhibiting the lowest dark current. This effect has been observed in other studies[155] and has been suggested to be due to the increase in the quasi-Fermi level of SnO_2 which in turn should increase the open-circuit voltage (V_{OC}) of the device.[41] Dyed bare aerogels were not produced in this study, since immersion of an uncoated aerogel in a dye bath followed by removal and drying resulted in collapse of the aerogel structure.

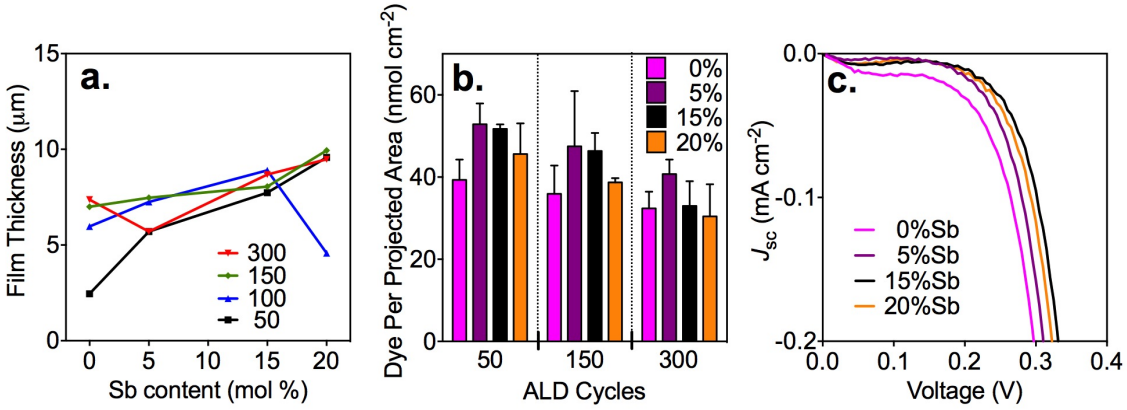

Figure 6.2. Characterization of the aerogel films. (a) Thickness of films (b) and dye uptake measurement of D149 desorbed in DMF as a function of Sb content in ATO aerogels and TiO_2 coatings by ALD. (c) Dark currents in I^-/I_3^- of unsensitized, bare aerogel films as a function of Sb content.

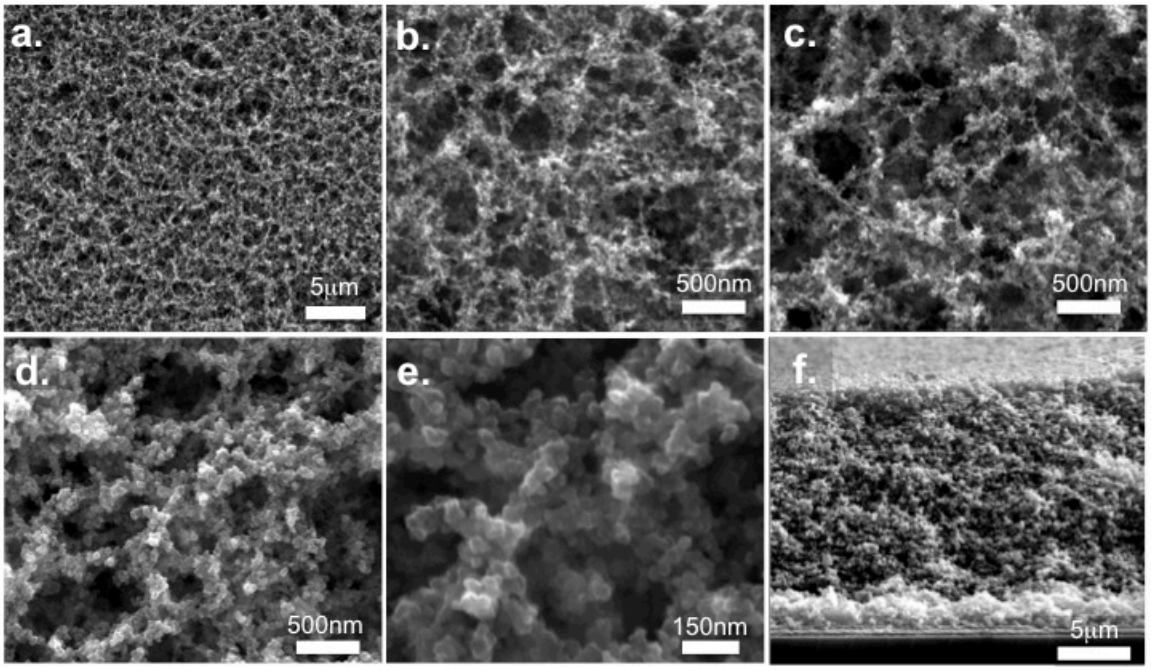

Figure 6.3. Top views of a 15 %Sb ATO aerogel without TiO_2 coating at different magnifications (a and b) and of the aerogel with (c) 150 and (d and e) 300 cycles of TiO_2; cross-section (f) of the sample shown in (c).

SEM images were used to study the morphological changes with varying Sb content and ALD cycles. There was no noticeable effect of Sb content on the surface morphology. The films were homogenous and exhibited crack-free coverage as seen, for example, in Figure 6.3a for a 15% Sb sample with no TiO_2 coating. At higher magnification (Figure 6.3b) the nanoparticulate, open-pore structure typical of aerogels is seen. The addition of 150 ALD cycles of TiO_2 (Figure 6.3c) does not have a significant impact on the morphology of the film at this magnification. At 300 cycles the TiO_2 overlayer is thick enough to be clearly seen by SEM (Figures 6.3d and e). Figure 6.3f shows a cross-section image of a 15% ATO sample coated with 150 cycles of TiO_2.

6.2.2 Crystal Structure

XRD was used to study the crystalline phases of the aerogel films (Figure 6.4a). All samples matched the SnO_2 rutile pattern (JCPDS No. 41-1445) with 110, 101, 200 and 211 lattice planes. A sample with a thick coating of 700 ALD cycles of TiO_2 was produced to clearly show TiO_2-derived XRD features. An increase in the number of ALD cycles shows the gradual formation of rutile TiO_2 (Figure 6.4b, labeled TiO_2-R) becoming evident at 300 and fully visible at 700 ALD cycles. The TiO_2 rutile phase may be present at the lower cycles (50, 100 and 150) but the low signal from these thin layers leaves somewhat ambiguous whether these thinner layers are amorphous or crystalline (rutile phase).[160] Rutile TiO_2 has been shown to grow epitaxially on the SnO_2 rutile structure due to the relatively low lattice mismatch (~4%).[161,162] Several methods, including $TiCl_4$ treatment[163] and ALD[123,164] on SnO_2[123,164] materials have shown a rutile crystalline phase.

No peaks representing the anatase phase were observed for samples with 300 (~12nm) or fewer ALD cycles. Law et al. showed that ZnO nanowires coated by with TiO_2 up to 5 nm-thick show an amorphous phase, which becomes anatase only above that threshold when using $TiCl_4$ treatment.[160] Because of the large lattice mismatch (~34%) between rutile SnO_2 and anatase TiO_2, it is not surprising that even at 300 cycles no anatase TiO_2 is observed. However, it was found that at 700 ALD cycles a clear peak for anatase TiO_2 emerges, a phenomenon not observed for SnO_2 samples coated by a similar ALD process ($TiCl_4$ used as a precursor) even at very thick TiO_2 coatings.[123] Similarly, in silica aerogels coated with TiO_2 by ALD, it was found that thinner layers did not exhibit any crystalline structure other than those of the FTO glass. The anatase phase of TiO_2 was found with 10-nm overlayers, and no TiO_2 rutile phase was reported, which is not surprising given the amorphous nature of the silica substrate.[96,165]

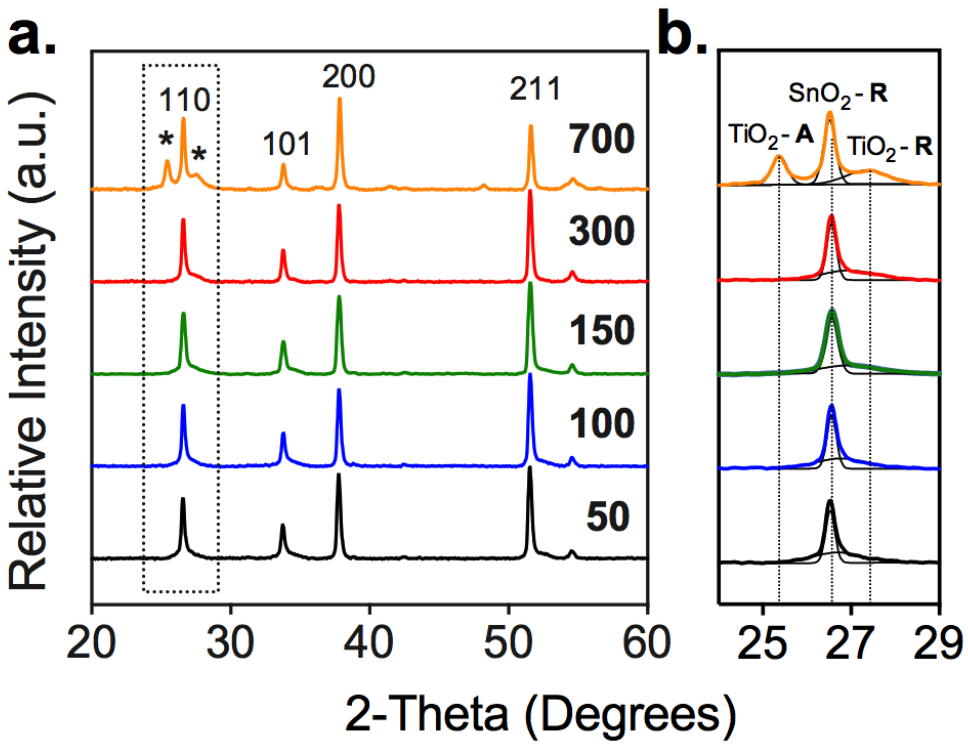

Figure 6.4. (a) X-ray diffraction patterns of ATO aerogel films on FTO glass coated with varying cycles of TiO_2 by ALD. (b) Expanded view of the patterns showing the rutile phase of SnO_2 and TiO_2 (labeled TiO_2-R) and the anatase phase of TiO_2 (labeled TiO_2-A).

6.2.3 Device Performance

Figure 6.5 summarizes device performance characteristics in I^-/I_3^- with varying Sb content and number of TiO_2 ALD cycles. V_{OC} increased consistently with the increase in TiO_2 cycles from about 0.6 to over 0.7 V (Figure 6.5a) as reported for related core-shell systems.[41,161,166] The short-circuit current density (J_{SC}) saw the highest improvement from 50 to 150 cycles, where it plateaus yielding no further improvement. A possible explanation is that the low currents at 50 cycles (~2 nm) may be caused by the lack of a crystalline phase at such thin layer thickness, which makes for inefficient electron injection from the photoexcited dye,[167] while thicker TiO_2 layers seem to crystallize

epitaxially in the rutile phase (Figure 6.5b). Samples with 50 ALD cycles exhibit a remarkable fill factor (FF) of ca. 0.62 (Figure 6.5c), unseen for devices using similar configurations.[41,155] This can be attributed to the successful deposition of a conformal layer that prevents shunt leaks to the dye and electrolyte. However, the FF diminished with the addition of TiO_2 layers, which suggests mass transport limitations as the constriction of pores impedes the diffusion of the electrolyte. This effect was also reported by Hamann et al. with ZnO layers grown by ALD on silica aerogels.[97] The slight increase of fill factor at 300 ALD cycles reflects a stagnant maximum power point while the V_{OC} increases relative to the 150-cycle sample. With the I^-/I_3^- electrolyte, Sb doping does not have a significant effect on the device performance. This is unsurprising since charge collection is typically high regardless of the collector due to the slow recombination rates with this redox couple. The power conversion efficiencies (Figure 6.5d) follow a similar trend to that of the J_{SC}, slightly decreasing after 150 cycles.

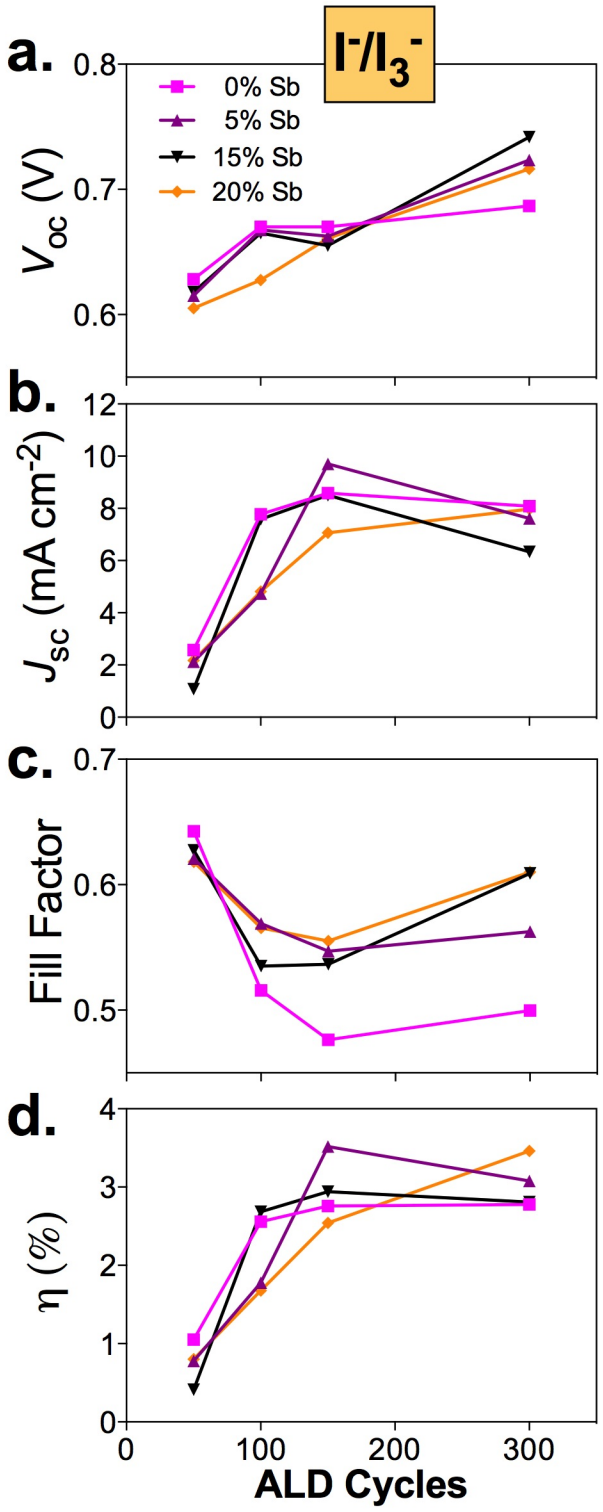

Figure 6.5. Effects of TiO2 layer thickness by ALD on the photovoltaic parameters of devices with undoped and ATO aerogels at different Sb concentrations and I^-

/I_3^- electrolytes: (a) open circuit voltage, (b) short circuit current, (c) fill factor and (d) power conversion efficiency.

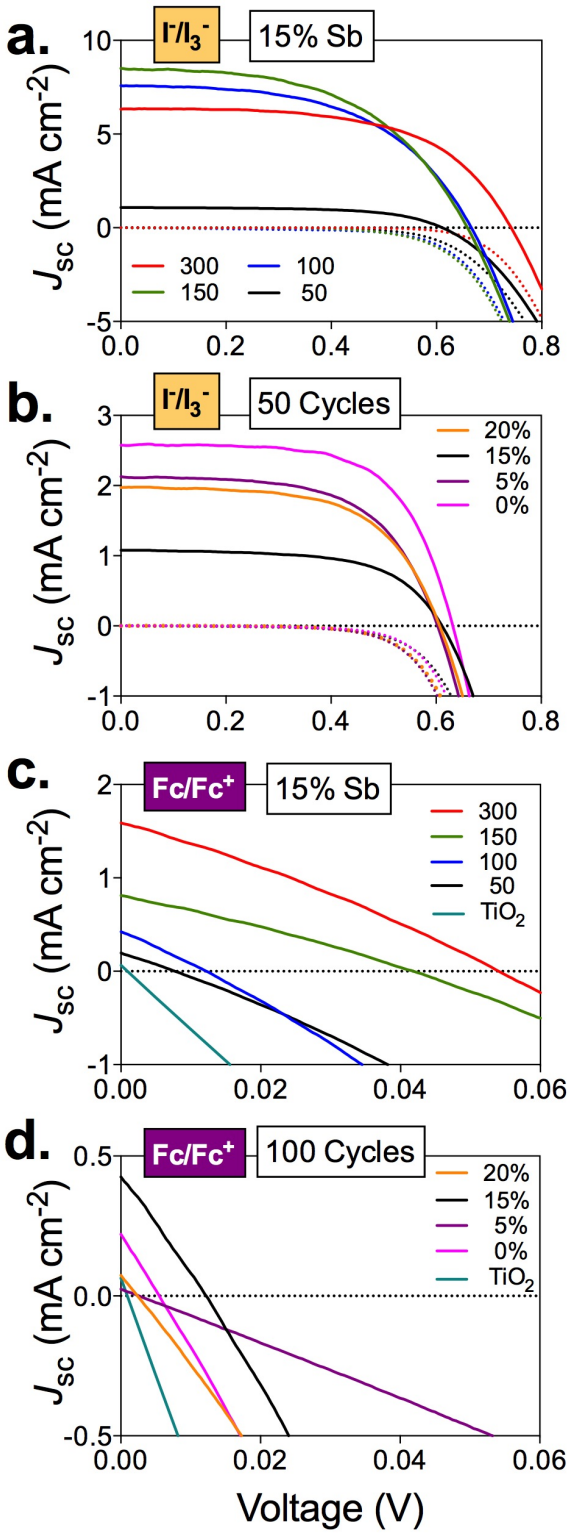

Figure 6.6. Current-voltage characteristics of solar cells under 1 sun. ATO 15% Sb aerogels with varying ALD cycles (a) and 50 ALD cycles with varying Sb content (b) in I^-/I_3^-. ATO 15% Sb aerogels with varying ALD cycles (c) and 100 ALD cycles with varying Sb content (d) in Fc/Fc^+.

Figure 6.6 shows the current-voltage characteristics of the devices with varying Sb content and number of TiO_2 ALD cycles in I^-/I_3^- and Fc/Fc^+. Figure 6.6a shows the effect of TiO_2 cycles in I^-/I_3^- for ATO aerogels with 15% Sb. All curves show typical shapes with increasing currents with increasing number of TiO_2 ALD cycles. Samples coated with 300 ALD cycles exhibit a considerable decrease due to lower dye loading compared to 50 and 150 ALD cycles (from 33 to 51 nmol cm^{-2} for 15% Sb samples coated with 50 to 300 ALD cycles, respectively), as seen in Figure 6.2b. Dark currents showed no clear pattern, with the exception of samples with 300 cycles, which demonstrated lower recombination. This can be attributed to the full formation of a thick rutile TiO_2 coating (shown in Figure 6.4b) and therefore a well-defined band structure. The band edge of TiO_2 is more positive than that of SnO_2[168] thus creating an energy barrier that slows down recombination of electrons with the electrolyte. With thinner rutile TiO_2 layers (50, 100 and 150 ALD cycles) a tunneling effect, seen in other core-shell configurations in DSCs,[169] may occur giving rise to higher recombination rates. Varying Sb content in the aerogel does not have a significant impact in devices with 50 ALD cycles (I^-/I_3^-), except for the 15% Sb sample, which showed currents well below the others.

Fc/Fc^+ was used as a model electrolyte with a high recombination rate to test the effect of the TCO aerogel on charge collection. Figure 6.6c shows the device characteristics of ATO aerogels with 15% Sb and a varying number of TiO_2 ALD cycles; the results are also compared to a TiO_2 nanoparticle film. Some photocurrent is produced by all devices but there is a sharp increase in the J_{SC} and V_{OC} with increasing ALD cycles, which again

can be attributed to the formation of better-crystallized (rutile) TiO_2 layers resulting in improved electron photoinjection. The TiO_2 current–voltage characteristics of ATO aerogel devices with varying Sb content and 100 ALD cycles are shown in Figure 6.6d. Samples with 15% Sb produce the highest photocurrent, suggesting improved charge collection efficiency. This agrees with our previous finding in bulk ATO aerogels that 15% Sb was optimum doping level for minimum resistivity.[156] A similar trend is seen for samples with 50 ALD cycles, but the Sb doping level had only small effects for samples coated with 150 and 300 TiO_2 ALD cycles (data not shown here). In general, these core-shell systems have a superior performance than TiO_2 nanoparticle films in Fc/Fc^+, suggesting faster electron transport and consequently improved charge collection efficiency.

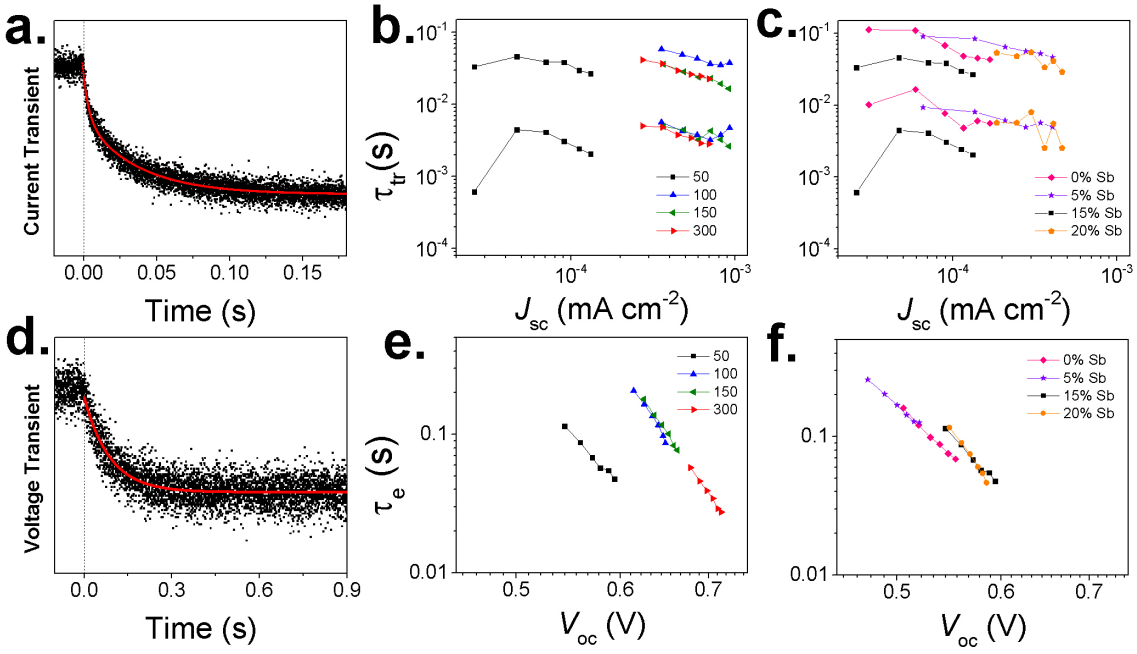

Figure 6.7. (a) An example current transient with a biexponential decay fit; fitted electron transport time constants versus short circuit current for (b) 15% Sb ATO aerogel devices with varying TiO_2 ALD cycles and (c) 50 TiO_2 ALD cycles with varying Sb content; (d) example voltage transient with single exponential decay fit; fitted electron lifetime

constant versus V_{OC} for (e) 15% Sb ATO aerogel devices with varying TiO_2 ALD cycles, (f) 50 TiO_2 ALD cycles with varying Sb content.

6.2.4 Electron Kinetics in the DSC

In order to further understand the performance of the TiO_2-coated ATO aerogel systems we investigated the electron kinetics in these devices. The data are summarized in Figure 6.7. Electron transport transient data required a double exponential decay expression for a good fit (Figure 6.7a) and therefore there are two points plotted for each measurement in Figures 6.7(b) and (c). We posit that the two time constants may be due to slower transport along the TiO_2 shell and faster transport through the conductive ATO aerogel core. The partly amorphous nature of the TiO_2 shell results in slower electron transport than typically observed in crystalline TiO_2 nanoparticle films. 15% Sb ATO aerogel samples with 100 or more ALD cycles of TiO_2 did not show significant differences in the electron transport kinetics, but at 50 cycles the time constants were noticeably faster than for the other samples. However, the short times observed at the lowest current for the 50-cycle sample in Figure 6.7(b) is likely an artifact as the transient was not sufficiently small compared to the mean current to maintain linearity of the measurement. In comparing Sb doping levels among samples with 50 ALD cycles (Figure 6.7c), samples composed of 15% Sb ATO aerogels exhibited faster electron transport than undoped, 5% Sb and 20% Sb samples. This finding is again in agreement with our finding[156] that the ATO aerogel is most conductive at a 15% Sb doping level.

In contrast, voltage decays were well fit by single-exponential decay expressions, which were used to extract the lifetime constants of the different devices (Figure 6.7d). The sample with 15% Sb and 50 ALD cycles shows a shorter electron lifetime when compared to 100, 150 and 300 ALD cycles (Figure 6.7e). The 50-ALD-cycle TiO_2 coating

(ca. 2 nm) may be too thin to effectively block recombination from the electron-rich ATO material to the electrolyte. For samples with 50 ALD cycles the variation in Sb content did not see a significant change in the electron lifetime kinetics (Figure 6.7f). These findings suggest that as little as 100 ALD cycles (4 nm) are able to keep recombination at rates typical of TiO_2/electrolyte rather than TCO/electrolyte interfaces.

6.3 Conclusions

We have synthesized ATO aerogels with varying Sb content as electron collectors coated with ultrathin TiO_2 layers for applications in DSCs. We used a sol-gel method to deposit the wet gels on FTO glass and supercritical drying to produce aerogel thin films. The ATO aerogel films were successfully coated with TiO_2 by ALD. XRD for samples with deposited TiO_2 revealed only rutile and no trace of the anatase phase was observed. In I^-/I_3^- the performance parameters are not affected by Sb content but they are by the number of ALD layers. Power conversion efficiency is highest for samples with 150 cycles and above; whereas currents are lowest at 50 ALD cycles, which might be due to poor electron injection through amorphous TiO_2. For aerogels with 50 ALD cycles in Fc/Fc^+ electrolytes, 15% Sb samples have significantly higher current and voltage than undoped aerogels or a nanoparticulate TiO_2 film, suggesting improved charge collection efficiency. DSC electron kinetics shows that 15% ATO aerogel samples coated with 50 ALD cycles have faster transport than samples coated with thicker TiO_2 films or with different Sb content. Electron lifetime for samples with 50 ALD cycles is shorter than for samples with thicker TiO_2 layers, but it does not vary significantly with Sb content. This transparent conducting aerogel structure exhibits high surface area and promising results with high recombination electrolytes such as Fc/Fc^+.

7 Conclusions

The main objective of this thesis was to produce thin films of transparent conducting oxide aerogels as conductive scaffolds in DSCs. This was motivated by the desire to improve electron transport rates within the photoanode materials to replace the ubiquitous TiO_2. SnO_2 aerogels doped with different materials (i.e. fluorine and antimony), were prepared as bulk and thin film aerogels. The incorporation of fluorine was found to be key in the formation of monolithic thin films, which did not delaminate, a crucial result for the preparation of DSCs. Fluorine however did not show any change in the electronic properties of the aerogel materials. Given these results F was used to maintain the morphological advantages of aerogels as thin films while another dopant, namely antimony, was used to improve the electronic properties of the material. It was found that Sb(V) significantly reduced the resistivity of the SnO_2 aerogels, presumably by means of interstitial doping while keeping absorption low in the visible range of the spectrum. The ability to cast these TCO aerogels on FTO glass made it ideal for preparation of DSCs where thin TiO_2 overlayers served both as blocking layers for electron recombination with the electrolyte and as a suitable substrate for dye-sensitizing.

In order to fully understand the effect of F in the morphological changes of the aerogel structure, a thorough study of the fluorinated and unfluorinated materials was done. Addition of F (by NH_4F) significantly decreased the gelation time of the Sn solution. Apparent shrinkage after SCD decreased with the addition F with unfluorinated samples exhibiting 39% shrinkage while fluorinated samples (at 1:1 precursor F:Sn) only 7%. All samples showed large shrinkage after calcination, but fluorinated samples (1:1) showed the smallest shrinkage. TGA and TPD experiments indicated no PPO release for unfluorinated samples but instead CO_2 was detected, suggesting the reaction of PPO with the oxygen in SnO_2. In contrast, fluorinated samples (1:1) exhibited no CO_2 signal,

whereas PPO was readily detected. This suggests that F prevents the bonding with a PPO fragment, thus preventing additional shrinkage presumably caused by the removal of oxygen atoms in SnO_2. All aerogel materials exhibited a cassiterite (rutile) crystal structure with well-defined lattice fringes as observed by TEM and XRD. Crystallite size decreased with the addition of precursor fluorine. Uncalcined materials exhibited a decrease in surface area with increasing F concentration, but this trend disappeared after calcination at 450˚C with surface area for all materials remaining around 100-150 m^2g^{-1}

Sb(V) was used in order to improve the electronic properties of the SnO_2. The first ATO aerogel has been synthesized and characterized based on facile epoxide-assisted synthetic processing. In our sol–gel procedure, the addition of NH_4F to the precursor solution did not result in significant incorporation of F or reduction of resistivity, but it significantly reduced aerogel shrinkage during calcination. The use of $SbCl_5$ together with NH_4F resulted in Sb incorporation and a 3.5-order-of-magnitude reduction in resistivity to $1.1x10^3$ Ω-cm for samples calcined at 450˚C at the optimal Sb:Sn precursor ratio of 15%. The Sb-doped materials exhibited low visible light absorbance. Calcining at 800˚C yielded a further 2 orders of magnitude decrease in the monolithic aerogel resistivity to ~30 □-cm, partly due to increased crystallite size. However, a tradeoff exists as materials calcined at this temperature also yield low surface area and pore volume, which are important properties of aerogels. Sb doped materials calcined at 450˚C therefore yield both improved conductivity and morphological traits typical of aerogels. The high surface area and open-pore structure of these materials, along with their high conductivity and low absorbance, make them well suited to optoelectronic applications. Work is ongoing on the preparation and characterization of thin films of these aerogels and their applications in solar cell devices.

These materials were used as thin films and made into DSCs. We synthesized ATO aerogels with varying Sb content as electron collectors coated with ultrathin TiO_2 layers for applications in DSCs. We used a sol-gel method to deposit the wet gels on FTO glass and supercritical drying to produce aerogel thin films. The ATO aerogel films were successfully coated with TiO_2 by ALD. XRD for samples with deposited TiO_2 revealed only rutile and no trace of the anatase phase was observed. In I^-/I_3^- the performance parameters are not affected by Sb content but they are by the number of ALD layers. Power conversion efficiency is highest for samples with 150 cycles and above; whereas currents are lowest at 50 ALD cycles, which might be due to poor electron injection through amorphous TiO_2. For aerogels with 50 ALD cycles in Fc/Fc^+ electrolytes, 15% Sb samples have significantly higher current and voltage than undoped aerogels or a nanoparticulate TiO_2 film, suggesting improved charge collection efficiency. DSC electron kinetics shows that 15% ATO aerogel samples coated with 50 ALD cycles have faster transport than samples coated with thicker TiO_2 films or with different Sb content. Electron lifetime for samples with 50 ALD cycles is shorter than for samples with thicker TiO_2 layers, but it does not vary significantly with Sb content. This transparent conducting aerogel structure exhibits high surface area and promising results with high recombination electrolytes such as Fc/Fc^+.

8 References

(1) Bjorn, L. O. *Photobiology: The Science of Life and Light*; 2nd ed.; Springer: New York, 2008.

(2) (ASTM), A. S. f. T. a. M. *Terrestrial Reference Spectra for Photovoltaic Performance Evaluation*.

(3) *Renewables 2013: Global Status Report*, Renewable Energy Policy Network for the 21st Century, 2013.

(4) Bequerel, E. *C.R. Acad. Sci.* **1839**, *9*, 145.

(5) Chapin, D. M.; Fuller, C. S.; Pearson, G. L. *J. Appl. Phys.* **1954**; 25, 676.

(6) Green, M. A. *Third Generation Photovoltaics: Advanced Solar Energy Conversion*; 2nd ed.; Springer, 2005.

(7) O'regan, B.; Grätzel, M. *Nature* **1991**, *353*, 737.

(8) Chen, C.-Y.; Wang, M.; Li, J.-Y.; Pootrakulchote, N.; Alibabaei, L.; Ngoc-le, C.-h.; Decoppet, J.-D.; Tsai, J.-H.; Grätzel, C.; Wu, C.-G.; Zakeeruddin, S. M.; Grätzel, M. *ACS Nano* **2013**, *3*, 3103.

(9) Yella, A.; Lee, H.-W.; Tsao, H. N.; Yi, C.; Chandiran, A. K.; Nazeeruddin, M. K.; Diau, E. W.-G.; Yeh, C.-Y.; Zakeeruddin, S. M.; Grätzel, M. *Science* **2011**, *334*, 629.

(10) Peter, L. *Acc. Chem. Res.* **2009**, *42*, 1839.

(11) Koops, S. E.; O'Regan, B. C.; Barnes, P. R. F.; Durrant, J. R. *J. Am. Chem. Soc.* **2009**, *131*, 4808.

(12) Benkö, G.; Kallioinen, J.; Korppi-Tommola, J. E. I.; Yartsev, A. P.; Sundström, V. *J. Am. Chem. Soc.* **2002**, *124*, 489.

(13) Kuang, D.; Ito, S.; Wenger, B.; Klein, C.; Moser, J.-E.; Humphry-Baker, R.; Zakeeruddin, S. M.; Grätzel, M. *J. Am. Chem. Soc.* **2006**, *128*, 4146.

(14) Grätzel, M. *Inorg. Chem.* **2005**, *44*, 6841.

(15) Boschloo, G.; Hagfeldt, A. *Acc. Chem. Res.* **2013**, *42*, 1819.

(16) Gregg, B. A.; Pichot, F.; Ferrere, S.; Fields, C. L. *J. Phys. Chem. B* **2001**, *105*, 1422.

(17) Hamann, T. W.; Farha, O. K.; Hupp, J. T. *J. Phys. Chem. C* **2008**, *112*, 19756.

(18) Daeneke, T.; Kwon, T.-H.; Holmes, A. B.; Duffy, N. W.; Bach, U.; Spiccia, L. *Nat. Chem.* **2011**, 3, 213.

(19) Kashif, M. K.; Axelson, J. C.; Duffy, N. W.; Forsyth, C. M.; Chang, C. J.; Long, J. R.; Spiccia, L.; Bach, U. *J. Am. Chem. Soc.* **2013**, *134*, 16646.

(20) Feldt, S. M.; Gibson, E. A.; Gabrielsson, E.; Sun, L.; Boschloo, G.; Hagfeldt, A. *J. Am. Chem. Soc.* **2010**, *132*, 16714.

(21) Kashif, M. K.; Nippe, M.; Duffy, N. W.; Forsyth, C. M.; Chang, C. J.; Long, J. R.; Spiccia, L.; Bach, U. *Angew. Chem. Int. Ed.* **2013**, *52*, 5527.

(22) Powar, S.; Daeneke, T.; Ma, M. T.; Fu, D.; Duffy, N. W.; Götz, G.; Weidelener, M.; Mishra, A.; Bäuerle, P.; Spiccia, L.; Bach, U. *Angew. Chem. Int. Ed.* **2012**, *52*, 602.

(23) Yum, J.-H.; Baranoff, E.; Kessler, F.; Moehl, T.; Ahmad, S.; Bessho, T.; Marchioro, A.; Ghadiri, E.; Moser, J.-E.; Yi, C.; Nazeeruddin, M. K.; Grätzel, M. *Nature Comm.* **2012**, *3*, 631.

(24) Bach, U.; Lupo, D.; Comte, P.; Moser, J. E.; Weissörtel, F.; Salbeck, J.; Spreitzer, H.; Grätzel, M. *Nature* **1998**, *395*, 583.

(25) Cai, N.; Moon, S.-J.; Cevey-Ha, L.; Moehl, T.; Humphry-Baker, R.; Wang, P.; Zakeeruddin, S. M.; Grätzel, M. *Nano Lett.* **2011**, *11*, 1452.

(26) Ding, I. K.; Tétreault, N.; Brillet, J.; Hardin, B. E.; Smith, E. H.; Rosenthal, S. J.; Sauvage, F.; Grätzel, M.; McGehee, M. D. *Adv. Func. Mater.* **2009**, *19*, 2431.

(27) Fabregat-Santiago, F.; Bisquert, J.; Cevey, L.; Chen, P.; Wang, M.; Zakeeruddin, S. M.; Grätzel, M. *J. Am. Chem. Soc.* **2008**, *131*, 558.

(28) Burschka, J.; Pellet, N.; Moon, S.-J.; Humphry-Baker, R.; Gao, P.; Nazeeruddin, M. K.; Grätzel, M. *Nature* **2013**, *499*, 316.

(29) Liu, M.; Johnston, M. B.; Snaith, H. J. *Nature* **2013**, *501*, 395.

(30) Wang, J. T.-W.; Ball, J. M.; Barea, E. M.; Abate, A.; Alexander-Webber, J. A.; Huang, J.; Saliba, M.; Mora-Sero, I.; Bisquert, J.; Snaith, H. J.; Nicholas, R. J. *Nano Lett.* **2013**, *14*, 724.

(31) Chopra, K. L.; Major, S.; Pandya, D. K. *Thin Solid Films* **1983**, *102*, 1.

(32) Minami, T. *Semicond. Sci. Technol.* **2005**, *20*, S35.

(33) Badeker, K. *Ann Phys* **1907**, *22*, 749.

(34) Ginley, D. H., Hideo; Paine, David C. *Handbook of Transparent Conductors*; Springer, 2010.

(35) Beyer, W.; Hüpkes, J.; Stiebig, H. *Thin Solid Films* **2007**, *516*, 147.

(36) Kurz, A.; Brakecha, K.; Puetz, J.; Aegerter, M. A. *Thin Solid Films* **2006**, *502*, 212.

(37) Müller, V.; Rasp, M.; Štefanić, G.; Ba, J.; Günther, S.; Rathousky, J.; Niederberger, M.; Fattakhova-Rohlfing, D. *Chem. Mater.* **2009**, *21*, 5229.

(38) Terrier, C.; Chatelon, J. P.; Berjoan, R.; Roger, J. A. *Thin Solid Films* **1995**, *263*, 37.

(39) Schubert, E. F. *Physical Foundations of Solid-State Devices*; McGraw-Hill Inc., 2007.

(40) Granqvist, C. G. *Sol. Energy Mater. Sol. Cells* **2007**, *91*, 1529.

(41) Yang, Z.; Gao, S.; Li, T.; Liu, F.-Q.; Ren, Y.; Xu, T. *ACS Appl. Mater. Interfaces* **2012**, *4*, 4419.

(42) Icli, K. C.; Yavuz, H. I.; Ozenbas, M. *J. Solid State Chem.* **2013**, *210*, 22.

(43) Yin, Z.; Wang, Z.; Du, Y.; Qi, X.; Huang, Y.; Xue, C.; Zhang, H. *Adv. Mater.* **2012**, *24*, 5374.

(44) Liu, H.; Avrutin, v.; Izyumskaya, N.; Özgür, Ü.; Morkoç, H. *Superlattices Microstruct.* **2010**, *48*, 458.

(45) Chaisitsak, S. *Sensors 2011, Vol. 11, Pages 7127-7140* **2011**, *11*, 7127.

(46) Fukano, T.; Motohiro, T. *Sol. Energy Mater. Sol. Cells* **2004**, *82*, 567.

(47) Guglielmi, M.; Menegazzo, E.; Paolizzi, M.; Gasparro, G.; Ganz, D.; Pütz, J.; Aegerter, M. A.; Hubert-Pfalzgraf, L.; Pascual, C.; Durán, A.; Willems, H. X.; Van Bommel, M.; Büttgenbach, L.; Costa, L. *J. Sol-Gel Sci. Technol.* **1998**, *13*, 679.

(48) Nütz, T.; zum Felde, U.; Haase, M. *J. Chem. Phys.* **1999**, *110*, 12142.

(49) Nütz, T.; Haase, M. *J. Phys. Chem. B* **2000**, *104*, 8430.

(50) Geraldo, V.; Scalvi, L. V. A.; Lisboa-Filho, P. N.; Morilla-Santos, C. *J. Phys. Chem. Solids* **2006**, *67*, 1410.

(51) Correa Baena, J. P.; Agrios, A. G. *submitted for publication*.

(52) Hamd, W.; Wu, Y. C.; Boulle, A.; Thune, E.; Guinebretière, R. *Thin Solid Films* **2009**, *518*, 1.

(53) Sheel, D. W.; Yates, H. M.; Evans, P.; Dagkaldiran, U.; Gordijn, A.; Finger, F.; Remes, Z.; Vanecek, M. *Thin Solid Films* **2009**, *517*, 3061.

(54) Shanthi, E.; Dutta, V.; Banerjee, A.; Chopra, K. L. *J. Appl. Phys.* **1980**, *51*, 6243.

(55) Goebbert, C.; A Aegerter, M.; Burgard, D.; Nass, R.; Schmidt, H. *J. Mater. Chem.* **1999**, *9*, 253.

(56) Elangovan, E.; Ramamurthi, K. *Journal of Optoelectronics and Advanced Materials* **2003**, *5*, 45.

(57) Wu, S.; Yuan, S.; Shi, L.; Zhao, Y.; Fang, J. *J. Colloid Interface Sci.* **2010**, *346*, 12.

(58) Müller, V.; Rasp, M.; Štefanić, G.; Ba, J.; Günther, S.; Rathousky, J.; Niederberger, M.; Fattakhova-Rohlfing, D. *Chem. Mater.* **2009**, *21*, 5229.

(59) Boschloo, G.; Fitzmaurice, D. *J. Phys. Chem. B* **1999**, *103*, 3093.

(60) Lu, H. F.; Hong, R. Y.; Wang, L. S.; Xie, H. D.; Zhao, S. Q. *Mat. Lett.* **2012**, 68, 237.

(61) Volosin, A. M.; Sharma, S.; Traverse, C.; Newman, N.; Seo, D.-K. *J. Mater. Chem.* **2011**, *21*, 13232.

(62) Naghavi, N.; Marcel, C.; Dupont, L.; Leriche, J.-B.; Tarascon, J.-M. *Solid State Ionics* **2003**, *156*, 463.

(63) Rockenberger, J.; zum Felde, U.; Tischer, M.; Tröger, L.; Haase, M.; Weller, H. *J. Chem. Phys.* **2000**, *112*, 4296.

(64) Martinson, A. B. F.; Elam, J. W.; Liu, J.; Pellin, M. J.; Marks, T. J.; Hupp, J. T. *Nano Lett.* **2008**, *8*, 2862.

(65) Wang, Y.; Brezesinski, T.; Antonietti, M.; Smarsly, B. *ACS Nano* **2009**, *3*, 1373.

(66) Hou, K.; Puzzo, D.; Helander, M. G.; Lo, S. S.; Bonifacio, L. D.; Wang, W.; Lu, Z.-H.; Scholes, G. D.; Ozin, G. A. *Adv. Mater.* **2009**, *21*, 2492.

(67) Arsenault, E.; Soheilnia, N.; Ozin, G. A. *ACS Nano* **2011**, *5*, 2984.

(68) Sing, K. S. W.; Everett, D. H.; Haul, R. A. W.; Moscou, L.; Pierotti, R. A.; Rouquerol, J.; Siemieniewska, T. *Reporting physisorption data for gas/solid systems with special reference to the determination of surface area and porosity*, International Union of Pure and Applied Chemistry, **1985**.

(69) Hartmann, M. *Chem. Mater.* **2005**, *17*, 4577.

(70) Müller, V.; Rasp, M.; Rathousky, J.; Schütz, B.; Niederberger, M.; Fattakhova-Rohlfing, D. *Small* **2010**, *6*, 633.

(71) Bruce, P. G.; Scrosati, B.; Tarascon, J.-M. *Angew. Chem., Int. Ed.* **2008**, *47*, 2930.

(72) Brezesinski, T.; Wang, J.; Tolbert, S. H.; Dunn, B. *Nat Mater* **2010**, *9*, 146.

(73) Lang, X.; Hirata, A.; Fujita, T.; Chen, M. *Nat Nano* **2011**, *6*, 232.

(74) Pierre, A. C.; Pajonk, G. M. *Chem. Rev.* **2002**, *102*, 4243.

(75) Dorcheh, A. S.; Abbasi, M. H. *Journal of Materials Processing Technology* **2008**, *199*, 10.

(76) Rolison, D. R.; Dunn, B. *J. Mater. Chem.* **2001**, *11*, 963.

(77) Livage, J.; Henry, M.; Sanchez, C. *Prog. Solid State Chem.* **1988**, *18*, 259.

(78) Pajonk, G. M.; Elaloui, E.; Achard, P.; Chevalier, B.; Chevalier, J.-L.; Durant, M. *J. Non-Cryst. Solids* **1995**, *186*, 1.

(79) Mrowiec-Białoń, J.; Pająk, L.; Jarzębski, A. B.; Lachowski, A. I.; Malinowski, J. J. *Langmuir* **1997**, *13*, 6310.

(80) Gash, A. E.; Tillotson, T. M.; H, S. J.; Poco, J. F.; Hrubesh, L. W.; Simpson, R. L. *Chem. Mater.* **2001**, *13*, 999.

(81) Gao, Y. P.; Sisk, C. N.; Hope-Weeks, L. J. *Chem. Mater.* **2007**, *19*, 6007.

(82) Wang, S.; Wu, N. *J. Non-Cryst. Solids* **1998**, *224*, 259.

(83) Baumann, T. F.; Kucheyev, S. O.; Gash, A. E.; Satcher, J. H. *Adv. Mater.* **2005**, *17*, 1546.

(84) Davis, M.; Zhang, K.; Wang, S.; Hope-Weeks, L. J. *J. Mater. Chem.* **2012**, *22*, 20163.

(85) Kawashima, T.; Matsui, H.; Tanabe, N. *Thin Solid Films* **2003**, *445*, 241.

(86) Patterson, A. L. *Phys. Rev.* **1939**, *56*, 978.

(87) Cullity, B. D. **1978**.

(88) Schroder, D. K. *Semiconductor Material and Device Characterization*; 2nd ed. ed.; Wiley-Interscience, 2006.

(89) Horiuchi, T.; Miura, H.; Sumioka, K.; Uchida, S. *J. Am. Chem. Soc.* **2004**, *126*, 12218.

(90) Hamann, T. W.; Farha, O. K.; Hupp, J. T. *J. Phys. Chem. C* **2008**, *112*, 19756.

(91) Manthina, V.; Correa Baena, J. P.; Liu, G.; Agrios, A. G. *J. Phys. Chem. C* **2012**, *116*, 23864.

(92) Aricò, A. S.; Bruce, P.; Scrosati, B.; Tarascon, J.-M.; van Schalkwijk, W. *Nat. Mater.* **2005**, *4*, 366.

(93) Guo, Y.-G.; Hu, J.-S.; Wan, L.-J. *Adv. Mater.* **2008**, *20*, 2878.

(94) Suh, D. J.; Park, T.-J. *Chem. Mater.* **1996**, *8*, 509.

(95) Vacher, R.; Woignier, T.; Pelous, J.; Courtens, E. *Phys. Rev. B* **1988**, *37*, 6500.

(96) Williams, V. O.; Jeong, N. C.; Prasittichai, C.; Farha, O. K.; Pellin, M. J.; Hupp, J. T. **2012**, *6*, 6185.

(97) Hamann, T. W.; Martinson, A. B. F.; Elam, J. W.; Pellin, M. J.; Hupp, J. T. *Adv. Mater.* **2008**, *20*, 1560.

(98) Hamann, T. W.; Martinson, A. B. F.; Elam, J. W.; Pellin, M. J.; Hupp, J. T. *J. Phys. Chem. C* **2008**, *112*, 10303.

(99) Dunn, B.; Rolison, D. R. *J. Mater. Chem.* **2001**, *11*, 963.

(100) Ferrere, S.; Zaban, A.; Gregg, B. A. *J. Phys. Chem. B* **1997**, *101*, 4490.

(101) Kay, A.; Grätzel, M. *Chem. Mater.* **2002**, *14*, 2930.

(102) Snaith, H. J.; Ducati, C. *Nano Lett.* **2010**, *10*, 1259.

(103) Saito, R.; Miseki, Y.; Sayama, K. *Chem. Comm.* **2012**, *48*, 3833.

(104) Tatsuyama, C.; Ichimura, S. *Jpn. J. Appl. Phys.* **1976,** 15, 843.

(105) Miao, Z.; Wu, Y.; Zhang, X.; Liu, Z.; Han, B.; Ding, K.; An, G. *J. Mater. Chem.* **2007**, *17*, 1791.

(106) Ellmer, K. *Nature Photon* **2012**, *6*, 809.

(107) Calestani, D.; Lazzarini, L.; Salviati, G.; Zha, M. *Cryst. Res. Technol.* **2005**, *40*, 937.

(108) Shirato, N.; Strader, J.; Kumar, A.; Vincent, A.; Zhang, P.; Karakoti, A.; Nacchimuthu, P.; Cho, H. J.; Seal, S.; Kalyanaraman, R. *Nanoscale* **2011**, *3*, 1090.

(109) Aboulaich, A.; Boury, B.; Mutin, P. H. *Eur. J. Inorg. Chem.* **2011**, *2011*, 3644.

(110) Baumann, T.; Kucheyev, S.; Gash, A.; Satcher Jr, J. *Adv. Mater.* **2005**, *17*, 1546.

(111) Lee, M. M.; Teuscher, J.; Miyasaka, T.; Murakami, T. N.; Snaith, H. J. *Science* **2012**, *338*, 643.

(112) Ismail, A. A.; Ibrahim, I. A. *Applied Catalysis A: General* **2008**, *346*, 200.

(113) Reichenauer, G. *J. Non-Cryst. Solids* **2004**, *350*, 189.

(114) Nadargi, D. Y.; Kalesh, R. R.; Rao, A. V. *J. Alloys Compd.* **2009**, *480*, 689.

(115) Pope, E. J. A.; Mackenzie, J. D. *J. Non-Cryst. Solids* **1986**, *87*, 185.

(116) Ehrburger-Dolle, F.; Dallamano, J.; Elaloui, E.; Pajonk, G. M. *J. Non-Cryst. Solids* **1995**, *186*, 9.

(117) Suh, D. J.; Park, T.-J. *Chem. Mater* **1996**, *8*, 509.

(118) Mercera, P. D. L.; Van Ommen, J. G.; Doesburg, E. B. M.; Burggraaf, A. J.; Ross, J. R. H. *Applied Catalysis* **1990**, *57*, 127.

(119) Buonsanti, R.; Milliron, D. J. *Chem. Mater* **2013**, *25*, 1305.

(120) Müller, V.; Rasp, M.; Stefanic, G.; Günther, S.; Rathousky, J.; Niederberger, M.; Fattakhova-Rohlfing, D. *physica status solidi (c)* **2011**, *8*, 1759.

(121) Sanchez, C.; Boissière, C.; Grosso, D.; Laberty, C.; Nicole, L. *Chem. Mater* **2008**, *20*, 682.

(122) Fattakhova-Rohlfing, D.; Brezesinski, T.; Rathouský, J.; Feldhoff, A.; Oekermann, T.; Wark, M.; Smarsly, B. M. *Adv. Mater.* **2006**, *18*, 2980.

(123) Peng, Q.; Kalanyan, B.; Hoertz, P. G.; Miller, A.; Kim, D. H.; Hanson, K.; Alibabaei, L.; Liu, J.; Meyer, T. J.; Parsons, G. N.; Glass, J. T. *Nano Lett.* **2013**, *13*, 1481.

(124) Kim, D.-W.; Kim, D.-S.; Kim, Y.-G.; Kim, Y.-C.; Oh, S.-G. *Mater. Chem. Phys.* **2006**, *97*, 452.

(125) Gregg, S. J.; Sing, K. S. W. *Adsorption, Surface Area and Porosity*; 2nd ed. ed.; Academic Press, **1982**.

(126) Chandiran, A. K.; Sauvage, F. d. r.; Casas-Cabanas, M.; Comte, P.; Zakeeruddin, S. M.; Graetzel, M. *J. Phys. Chem. C* **2010**, *114*, 15849.

(127) Lee, K.-T.; Lu, S.-Y. *J. Mater. Chem.* **2012**, *22*, 16259.

(128) Trotochaud, L.; Boettcher, S. W. *Chem. Mater* **2011**, *23*, 4920.

(129) Liu, T. J.; Jin, Z. G.; Feng, L. R.; Wang, T. *Appl. Surf. Sci.* **2008**, *254*, 6547.

(130) Stranick, M. A.; Moskwa, A. *Surface Science Spectra* **1993**, *2*, 50.

(131) Terrier, C.; Chatelon, J. P.; Roger, J. A.; Berjoan, R.; Dubois, C. *J. Sol-Gel Sci. Technol.* **1997**, *10*, 75.

(132) Berry, F. J. *J. Catal.* **1982**, *73*, 349.

(133) Van Bommel, M. J.; Groen, W. A.; Van Hal, H. A. M.; Keur, W. C.; Bernards, T. N. M. *J. Mat. Sci.* **1999**, *34*, 4803.

(134) Izquierdo, R.; Sacher, E.; Yelon, A. *Appl. Surf. Sci.* **1989**, *40*, 175.

(135) Jianqi, W.; Daming, F.; Wenhui, W.; Minxiu, Z.; Yiz, L. *Polym. Degrad. Stab.* **1991**, *31*, 129.

(136) Benvenutti, E. V.; Gushikem, Y.; Vasquez, A.; de Castro, S. C.; Zaldivar, G. A. P. *J. Chem. Soc., Chem. Commun.* **1991**, 1325.

(137) Shiratsuchi, R.; Hongo, K.; Nogami, G.; Ishimaru, S. *J. Electrochem. Soc.* **1992**, *139*, 2544.

(138) Badrinarayanan, S.; Mandale, A. B.; Gunjikar, V. G.; Sinha, A. P. B. *J. Mater. Sci.* **1986**, *21*, 3333.

(139) Nefedov, V. I.; Gati, D.; Dzhurinskii, B. F.; Sergushin, N. P.; Salyn, Y. V. *Zh. Neorg. Khimii* **1975**, *20*, 2307.

(140) Wagner, C. D.; Zatko, D. A.; Raymond, R. H. *Anal. Chem.* **1980**, *52*, 1445.

(141) Pan, X. Q.; Fu, L. *J. Appl. Phys.* **2001**, *89*, 6048.

(142) Zhao, Q.; Xie, Y.; Dong, T.; Zhang, Z. *J. Phys. Chem. C* **2007**, *111*, 11598.

(143) Jeon, H.-J.; Jeon, M.-K.; Kang, M.; Lee, S.-G.; Lee, Y.-L.; Hong, Y.-K.; Choi, B.-H. *Mater. Lett.* **2005**, *59*, 1801.

(144) Emons, T. T.; Li, J.; Nazar, L. F. *J. Am. Chem. Soc.* **2002**, *124*, 8516.

(145) Kim, K.-S.; Yoon, S.-Y.; Lee, W.-J.; Ho Kim, K. *Surface and Coatings Technology* **2001**, *138*, 229.

(146) O'Regan, B.; Grätzel, M. *Nature* **1991**, *353*, 737.

(147) Peter, L. M. *J. Phys. Chem. C* **2007**, *111*, 6601.

(148) Boschloo, G.; Hagfeldt, A. *Acc. Chem. Res.* **2009**, *42*, 1819.

(149) Daeneke, T.; Kwon, T.-H.; Holmes, A. B.; Duffy, N. W.; Bach, U.; Spiccia, L. *Nature Chemistry* **2011**, *3*, 213.

(150) Gregg, B. A.; Pichot, F.; Ferrere, S.; Fields, C. L. *J. Phys. Chem. B* **2001**, *105*, 1422.

(151) Williams, V. O.; Jeong, N. C.; Prasittichai, C.; Farha, O. K.; Pellin, M. J.; Hupp, J. T. *ACS Nano* **2012**, *6*, 6185.

(152) Gao, X.-D.; Li, X.-M.; Gan, X.-Y.; Wu, Y.-Q.; Zheng, R.-K.; Wang, C.-L.; Gu, Z.-Y.; He, P. *J. Mater. Chem.* **2012**, *22*, 18930.

(153) Chappel, S.; Grinis, L.; Ofir, A.; Zaban, A. *J. Phys. Chem. B* **2005**, *109*, 1643.

(154) Grinis, L.; Ofir, A.; Dor, S.; Yahav, S.; Zaban, A. *Isr. J. Chem.* **2008**, *48*, 269.

(155) Icli, K. C.; Yavuz, H. I.; Ozenbas, M. *J. Solid State Chem.* **2014**, *210*, 22.

(156) Correa Baena, J. P.; Agrios, A. G., submitted for publication.

(157) Rahtu, A.; Ritala, M. *Chemical Vapor Deposition* **2002**, *8*, 21.

(158) Aarik, J.; Aidla, A.; Uustare, T.; Ritala, M.; Leskelä, M. *Appl. Surf. Sci.* **2000**, *161*, 385.

(159) Chandiran, A. K.; Yella, A.; Stefik, M.; Heiniger, L.-P.; Comte, P.; Nazeeruddin, M. K.; Grätzel, M. *ACS Appl. Mater. Interf.* **2013**, *5*, 3487.

(160) Law, M.; Greene, L. E.; Radenovic, A.; Kuykendall, T.; Liphardt, J.; Yang, P. *J. Phys. Chem. B* **2006**, *110*, 22652.

(161) Chappel, S.; Chen, S.-G.; Zaban, A. *Langmuir* **2002**, *18*, 3336.

(162) Nie, A.; Liu, J.; Li, Q.; Cheng, Y.; Dong, C.; Zhou, W.; Wang, P.; Wang, Q.; Yang, Y.; Zhu, Y.; Zeng, Y.; Wang, H. *J. Mater. Chem* **2012**, *22*, 10665.

(163) Snaith, H. J.; Ducati, C. *Nano Lett.* **2010**, *10*, 1259.

(164) Nie, A.; Liu, J.; Li, Q.; Cheng, Y.; Dong, C.; Zhou, W.; Wang, P.; Wang, Q.; Yang, Y.; Zhu, Y.; Zeng, Y.; Wang, H. *Journal of Materials Chemistry* **2012**, *22*, 10665.

(165) Snaith, H. J.; Ducati, C. *Nano Letters* **2010**, *10*, 1259.

(166) Ramasamy, E.; Lee, J. *J. Phys. Chem. C* **2010**, *114*, 22032.

(167) Benkö, G.; Skårman, B.; Wallenberg, R.; Hagfeldt, A.; Sundström, V.; Yartsev, A. P. *J. Phys. Chem. B* **2003**, *107*, 1370.

(168) Gubbala, S.; Chakrapani, V.; Kumar, V.; Sunkara, M. K. *Adv. Func. Mater.* **2008**, *18*, 2411.

(169) Chandiran, A. K.; Tetreault, N.; Humphry-Baker, R.; Kessler, F.; Baranoff, E.; Yi, C.; Nazeeruddin, M. K.; Grätzel, M. *Nano Lett.* **2012**, *12*, 3941.